

KM3NeT - WP5

Deliverable 5.1

**Report on evaluation of existing water, oceanographic,
biological and geological data from candidate sites**



INDEX

INTRODUCTION	3
1. WATER OPTICAL PROPERTIES	5
• Optics in deep sea	5
2. DEEP-SEA WATER OPTICAL PROPERTIES IN THE VARIOUS SELECTED MEDITERRANEAN SITES.	6
• Optical properties in ANTARES site	6
• Optical properties in NEMO site	7
• Optical properties in NESTOR site.	12
Measurements of deep-water transparency in South-West of Greece	12
A. Measurements with "good" geometry photometry	13
B. Measurements with "open" geometry photometry	20
3. MEASUREMENTS OF THE OPTICAL BACKGROUND	22
• Sources of optical background in seawater	22
Background from radioactive decay	22
Bioluminescence	22
Vertical Profiles of Bioluminescent Bursts	24
• Measurement of the optical background in the ANTARES site	25
Bioluminescent burst profiles at the ANTARES site	28
• Measurement of the optical background in the Capo Passero site	30
• Measurement of the optical background in the NESTOR site	31
Bioluminescent burst profiles at the NESTOR site	34
4. STUDY OF DEEP SEA CURRENTS IN SELECTED SITES	35
• Deep-sea currents in the ANTARES site	35
• Deep-sea currents in the NEMO site	37
• Deep-sea currents in the NESTOR site	39
5. STUDY OF DOWNWARD SEDIMENT FLUXES	47
• Sediment fluxes in ANTARES site	47
• Sediment fluxes in NEMO site	48

• Sediment fluxes in NESTOR site	50
6. GEOLOGICAL SURVEY OF THE SELECTED MEDITERRANEAN AREAS	55
• Geological survey of ANTARES site	55
• Geological survey of NEMO site	56
• Geological survey of NESTOR site	57
7. HYDROBIOLOGICAL SURVEY OF THE VARIOUS SELECTED AREAS	62
• Hydrobiological survey of NEMO site	62
• Water-mass structure and deep currents in the NESTOR area.	63
• Recent Hydrography in NESTOR area.	65
8. EFFECTS OF BIOFOULING ON OPTICAL SURFACES	72
• Biofouling measurements in ANTARES site	72
Biofilm collection system	74
• Biofouling measurements in NEMO site	74
• Biofouling measurements in NESTOR site	78
Analyzing the biofilm	81
• Corrosion and pressure action of the deep-sea on the NESTOR floor-detector	81
Components in deep-sea	82
Pressure action	83
Corrosion of the metal parts.	83
Summary about corrosion.	88
10. REFERENCES	90

Introduction

The Mediterranean Sea offers optimal conditions, on a worldwide scale, to locate an underwater neutrino telescope. Several sites exist, at depths beyond 2400m, that are potentially interesting to host an undersea neutrino telescope. The choice of the km³ scale neutrino telescope location is such an important task that careful studies of candidate sites must be carried out in order to identify the most suitable one. The ANTARES, NEMO and NESTOR Collaborations have performed dedicated research programs to characterize the possible deep-sea sites that could be appropriate for the installation of a deep-sea high-energy neutrino detector. Deep-sea water optical properties (absorption and diffusion) and the sites environmental properties (water temperature, salinity, biological activity, optical background, water currents and sedimentation) have been studied.

The site has to fulfil several requirements:

- *It has to be deep.* Thickness of the overlaying water has to be enough to filter out the down-going atmospheric muon background to allow the selection capability of up-going tracks (originated from up-going neutrino interactions in the Earth and/or the water near the detector). The needed background rejection is a function of the muon angle, of the muon energy and also depends on the capability of the muon reconstruction algorithm to correctly distinguish up-going tracks from down-going ones.
- *It has to be close to the coast.* The data transmission to the on-shore laboratory, as well as the transmission of power from the laboratory to the offshore detector, will be performed via an electro-optical multi-fibre cable. At distances closer than 100-120 km from the coast, commercial systems allow data and power transmission without special hardware requirements (e.g. amplifiers) that would increase the cost and reduce the reliability of the project. Moreover, the proximity to the coast and to shore infrastructures simplifies the access to the site for deployment and maintenance operations.
- *It has to be located far from shelf breaks and canyons.* Catastrophic submarine events, well known to oceanographers, such as *turbidity* and *density currents* may occur in the proximity of those structures.
- *The seabed has to be flat and stable.* The nature of the seabed should allow the mooring of the telescope structures.
- *It has to show good optical underwater properties.* The detector effective area is not only directly determined by the extension of the instrumented volume but is strongly affected by the light transmission in the water. Mainly two microscopic processes affect the propagation of light in the water: absorption and scattering. Light absorption directly reduces the effective area of the detector, the scattering worsen the detector track reconstruction performance, which is based on the measurement of the photon arrival time on the photon detectors.
- *The optical background has to be low.* The background directly affects the detector performances, in particular the quality of muon track reconstruction. In a high

background environment severe cuts to the photon detector data must be applied, hence reducing the detector effective area.

- *The sedimentation rate in the selected region must have very low values.* The presence of sediments in the water can affect seriously the performances of the detector. Sediments increase the light scattering and so worsen the track reconstruction angular resolution. Moreover a deposit on the sensitive part of photon detectors, i.e. large surface photomultipliers, reduces the global detector efficiency.
- *The site has to be “quiet”.* The underwater currents have to show low intensity and stable direction. This is important for several reasons:
 - it does not imply special requirements on the mechanical structure;
 - the detector deployment and positioning is easier if the water current is limited;
 - the optical noise due to bioluminescence, mainly excited by variation of the water currents, is reduced.

1. Water optical properties

• Optics in deep sea

The study of optical properties in the selected site is extremely important and should be completed with a long-term program of characterisation carried out in all different seasons. Seawater, indeed, absorbs and scatters photons as a function of water temperature, salinity and concentration, dimension and refraction index of dissolved and suspended, organic/inorganic particulate. These parameters are different in different marine sites and change as a function of time.

In order to describe the transparency of natural waters, as a function of photon wavelength, it is necessary to measure *in situ* the so called *Inherent Optical Properties* (IOP) of the water, such as the absorption $L_a(\lambda)$, scattering $L_b(\lambda)$ and attenuation $L_c(\lambda) = [L_a(\lambda) + L_b(\lambda)] / [L_a(\lambda) \times L_b(\lambda)]$ lengths [1]. Each of these lengths represents the path after which a photon beam of intensity I_0 and wavelength λ , travelling along the emission direction, is reduced of a factor $1/e$ by absorption or diffusion phenomena. These quantities can be directly derived by the simple relation:

$$I_{a,b,c}(x) = I_0 \exp(-x \cdot L_{a,b,c})$$

where x is the optical path traversed by the beam and I_0 the source intensity. In the literature the absorption $a = 1/L_a$ and the scattering $b = 1/L_b$ coefficients are extensively used to characterize the light transmission through matter. The sum of scattering and absorption coefficients is called attenuation coefficient $c(\lambda)$.

In pure water, light absorption and scattering are strongly wavelength dependent. In particular light transmission in pure water is extremely favoured in the range 350-550 nm, overlapping the region in which photomultiplier tubes usually reach the highest quantum efficiency. In the visible region of the electromagnetic spectrum light absorption steeply decreases as a function of wavelength and reaches its minimum at about 420 nm [2]. Scattering refers to processes in which the direction of the photon is changed without any other alteration. Scattering phenomena in which the photon wavelength changes (e.g. Raman effect) happen less frequently. Scattering can take place either on molecules (Rayleigh scattering) or on dissolved particulate (Mie scattering). Another parameter commonly used in the literature is the effective scattering length

$$L_b^{eff} = L_b(\lambda) / [1 - \langle \cos(\vartheta) \rangle],$$

where

$$\langle \cos(\vartheta) \rangle$$

is the average cosine of the scattering angle. The estimation of the last parameter is extremely difficult since it needs the knowledge of another IOP, the volume scattering function $b(\lambda, \vartheta)$, that must be measured with appropriate devices [3].

2. Deep-sea water optical properties in the various selected Mediterranean sites.

- **Optical properties in ANTARES site**

The ANTARES site has been studied during many years, especially with dedicated setups designed to characterize water optical properties. Most of measurements were made between 1997 and 2000 for two wavelengths, the blue (473 nm, with 10 nm of FWHM) and the UV (375 nm, with 10 nm of FWHM) light [4]. The results of absorption and scattering lengths are summarised in the following tables, as well as the effective attenuation length.

Time	Effective attenuation length	Absorption length	Scattering length
July 1998	$60.6 \pm 0.4 \pm 5$ m	$68.6 \pm 1.3 \pm 5$ m	$265 \pm 4 \pm 28$ m
March 1999	$51.9 \pm 0.7 \pm 1$ m	$61.2 \pm 0.7 \pm 1$ m	$228 \pm 11 \pm 24$ m
June 2000	$46.4 \pm 1.9 \pm 2$ m	$49.3 \pm 0.3 \pm 2$ m	$301 \pm 3 \pm 27$ m

Table 2.1: Summary of results for the blue data, where the first error is statistical and the second one is systematic.

Time	Effective attenuation length	Absorption length	Scattering length
July 1999	$21.9 \pm 0.8 \pm 2$ m	$23.5 \pm 0.1 \pm 2$ m	$119 \pm 2 \pm 10$ m
September 1999	$22.8 \pm 0.3 \pm 2$ m	$25.6 \pm 0.2 \pm 2$ m	$113 \pm 3 \pm 10$ m
June 2000	$26.0 \pm 0.5 \pm 1$ m	$28.9 \pm 0.1 \pm 1$ m	$133 \pm 3 \pm 12$ m

Table 2.2: Summary of results for the UV data, where the first error is statistical and the second one is systematic.

- **Optical properties in NEMO site**

Since July 1998 NEMO Collaboration started a series of campaigns of study in three sites close to the Italian coast. The sites were selected according to the geographical constraints of depth, proximity to the coast and nature of the seabed, listed in the previous section, to qualify the water optical properties.

These sites, shown in fig. 2.1, are:

- **Capo Passero**, located in the Ionian Sea South-East of Sicily at $36^{\circ} 16' N$, $16^{\circ} 06' E$, about 40 NM from the coast, with a depth of 3350 m;
- **Ustica**, located in the Tyrrhenian Sea North of Sicily at $38^{\circ} 55' N$, $13^{\circ} 18' E$, about 15 NM from the coast, with a depth of 3500 m;
- **Alicudi**, located in the Tyrrhenian Sea North of Sicily at $38^{\circ} 56' N$, $14^{\circ} 16' E$, about 25 NM from the coast, with a depth of 3500 m;

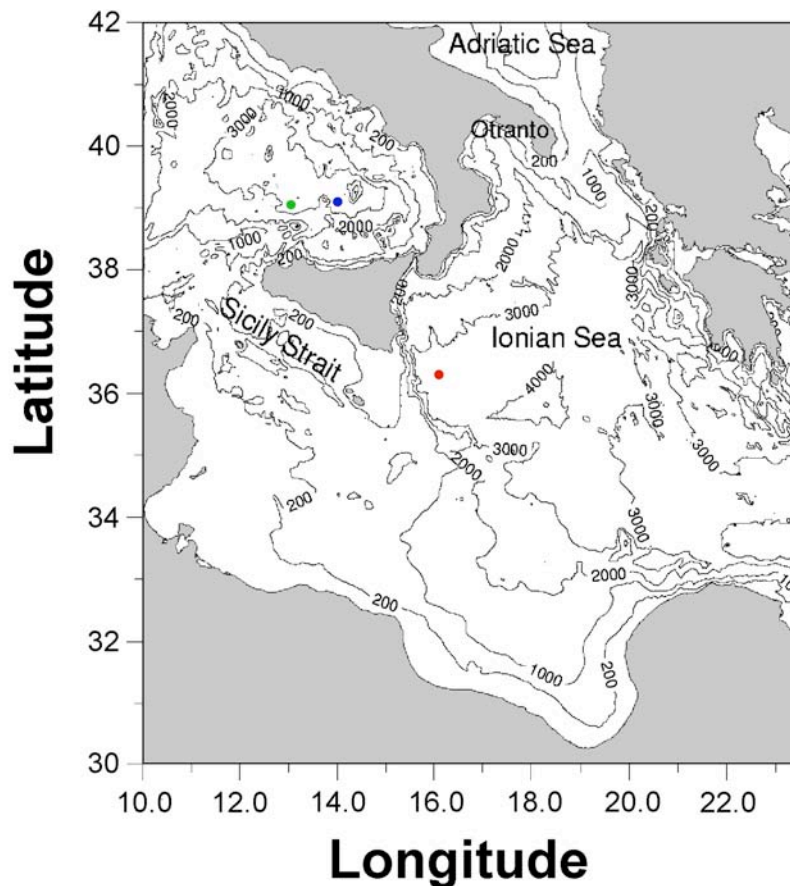


Figure 2.1 – Bathymetry of the central Mediterranean region. The sites explored by the NEMO collaborations are shown: Capo Passero (red dot), Ustica (green dot), Alicudi (blue dot).

In the Capo Passero region, which shows a wide plateau at more than 3000 m, two locations (fig. 2.2) have been investigated: one located at $36^{\circ} 16' N$, $16^{\circ} 06' E$ at about

40 NM from the coast, that has been denoted KM4, and a second one closer to the coast (20 NM), denoted KM3, located $36^{\circ} 30' N$, $15^{\circ} 50' E$.

The site presents the advantage of being close to well-equipped shore infrastructures:

- the ports of Siracusa, Augusta and Catania;
- the international airport of Catania;
- the I.N.F.N. Laboratori Nazionali del Sud in Catania.

Measurements of water optical properties have also been carried out in the Laboratori Nazionali del Sud Underwater Test Site, that is located 15 NM offshore Catania, at 2000m depths.

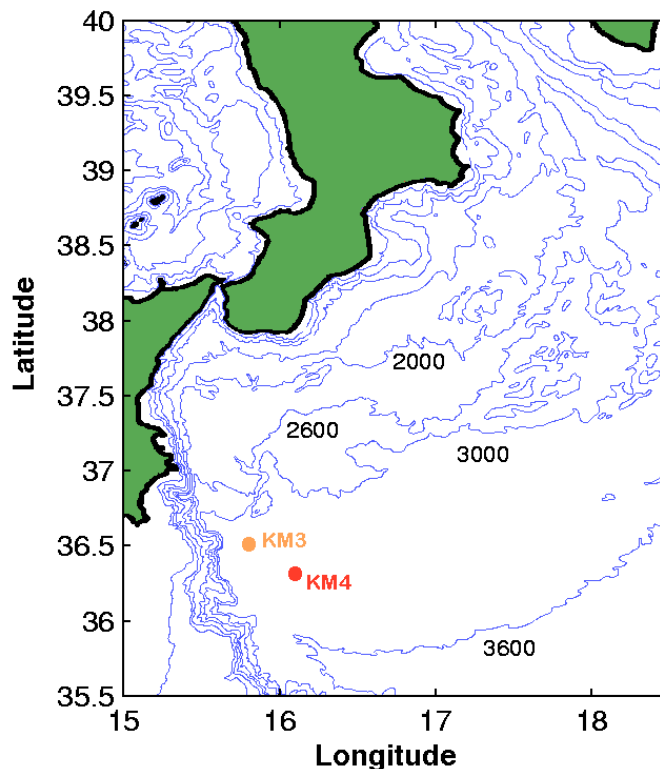


Figure 2.2 – The Capo Passero site. Both the explored sites, KM3 and KM4 are shown.

The optical properties of the four pre-selected sites (Ustica, Alicudi, Capo Passero KM3 and KM4) have been studied during several oceanographical campaigns since December 1999. Part of the data has already been published in [5], while a comprehensive report on all the results obtained in the preferred site, KM4, is presented in [6].

Two profiles of the water column have been carried out in each site. In figure 2.3 we report, as an example, the two profiles of sea temperature, salinity and the values of a and c coefficients for $\lambda = 440$ nm measured, as a function of depth, in KM4.

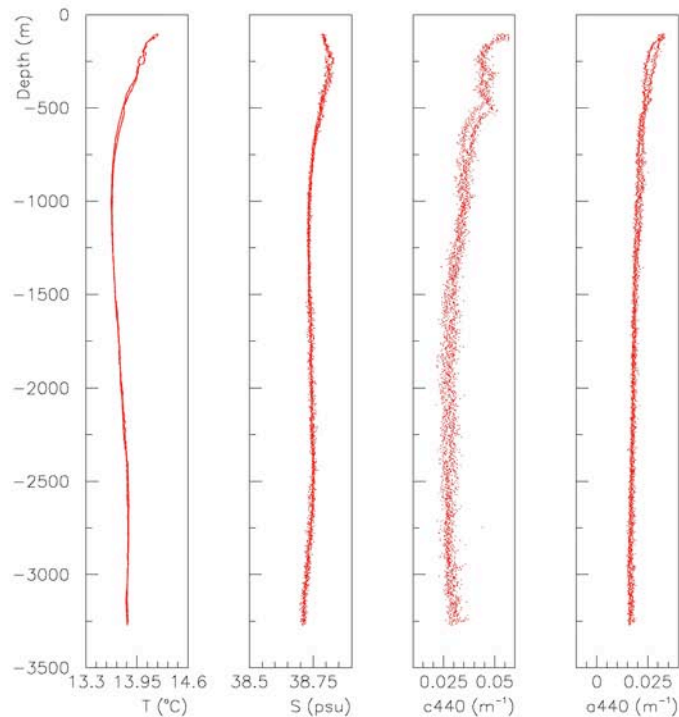


Figure 2.3 - Profiles of temperature (T), salinity (S), attenuation coefficient $c(440)$ and absorption coefficient $a(440)$ measured in KM4.

In order to compare the properties of the deepest waters in the different sites, the value of the absorption and attenuation coefficients a and c have been determined for each measurement by averaging the data over depths greater than 2850 m. Moreover, the data have also been averaged between the two measurements performed in each site. The statistical errors associated are negligible. Systematic errors have been estimated to be of the order of $\sigma_{a,c} \sim 2.0 \times 10^{-3} \text{ m}^{-1}$ for all the wavelengths. The results are summarized in figs. 2.4 and 2.5, where the average values of absorption and attenuation lengths measured in the four sites, are shown as a function of λ . In the figures we show the values of $L_a(\lambda) = 1/a(\lambda)$ and $L_c(\lambda) = 1/c(\lambda)$ in order to allow the reader to immediately evaluate the effect of water optical properties on the detector design.

We also show for comparison light transmission data for optically pure sea water (microfiltered water) taken from [1] [7]. It is clearly observable that at all wavelengths, deep waters in KM4 have an absorption length compatible with pure water. In comparison with the other sites, KM4 also shows the best values of L_c . The value of the light attenuation length is obviously worse than the one measured for microfiltered sea water, due to the dependence on the scattering coefficient, which is a function of the concentration of scattering centres dissolved in natural waters.

Having chosen KM4 as the best site among the four pre-selected, the NEMO Collaboration started a series of campaigns aiming at the study of the long-term

behaviour of optical properties in KM4. In particular three campaigns were performed during 2002 (March, May and August), in order to verify the occurrence of seasonal effects in optical properties. It is expected, in fact, that during the periods of major biological activity (like springtime) the concentration of dissolved and suspended particulate increases, worsening water transparency.

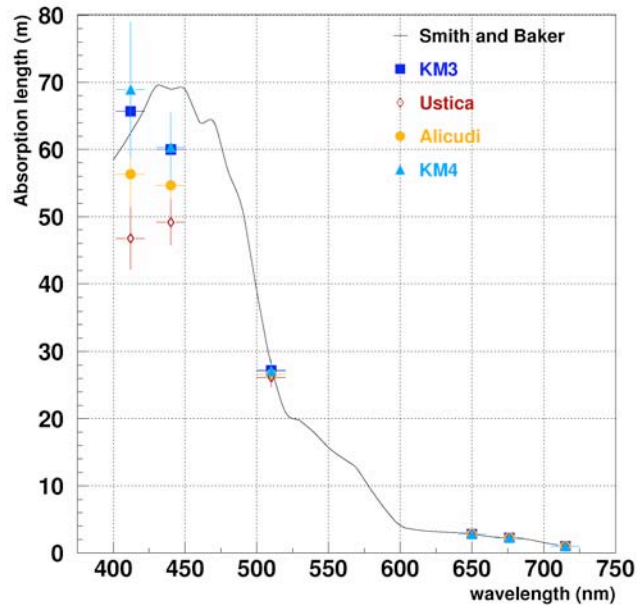


Figure 2.4 - Average absorption lengths, measured at depths greater than 2850 m, in KM3, KM4, Alicudi and Ustica. The curve relative to optically pure water [7] is plotted in black.

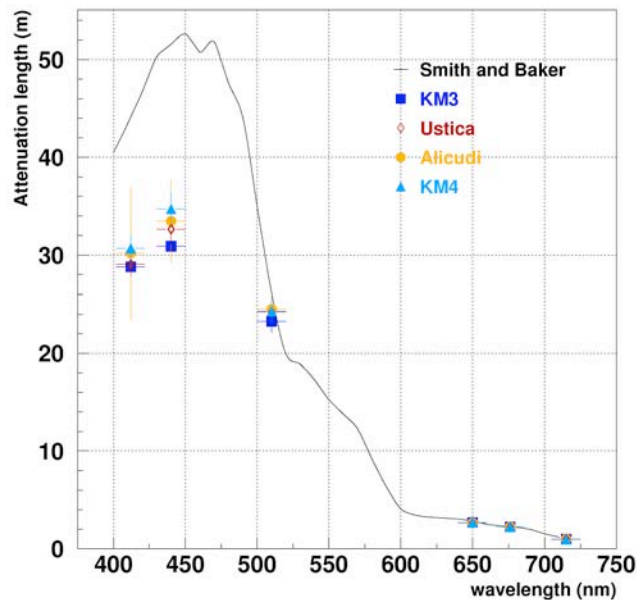


Figure 2.5 Average attenuation lengths, measured at depths greater than 2850 m, in KM3, KM4, Alicudi and Ustica. The curve relative to optically pure water [7] is plotted in black.

In figure 2.6 we show the profiles recorded with the AC9-CTD setup in the cruises of December 1999 (light blue), March 2002 (yellow), May 2002 (Blue) and August 2002 (red). The values of temperature, salinity and the coefficients $a(\lambda)$ and $c(\lambda)$ for the 440 nm wavelength are reported as a function of depth. Appreciable variations are observed in the temperature and salinity of shallow waters (first 500 m). These effects are also reflected in the optical properties. At the depths of interest for the telescope (>2500 m) seasonal variations are negligible and, for blue-green wavelengths, compatible with the instrument experimental error ($\sigma_T \sim 10^{-2}$ °C, $\sigma_S \sim 10^{-2}$ psu, $\sigma_{a,c} \sim 2 \cdot 10^{-3}$ m $^{-1}$). The absorption

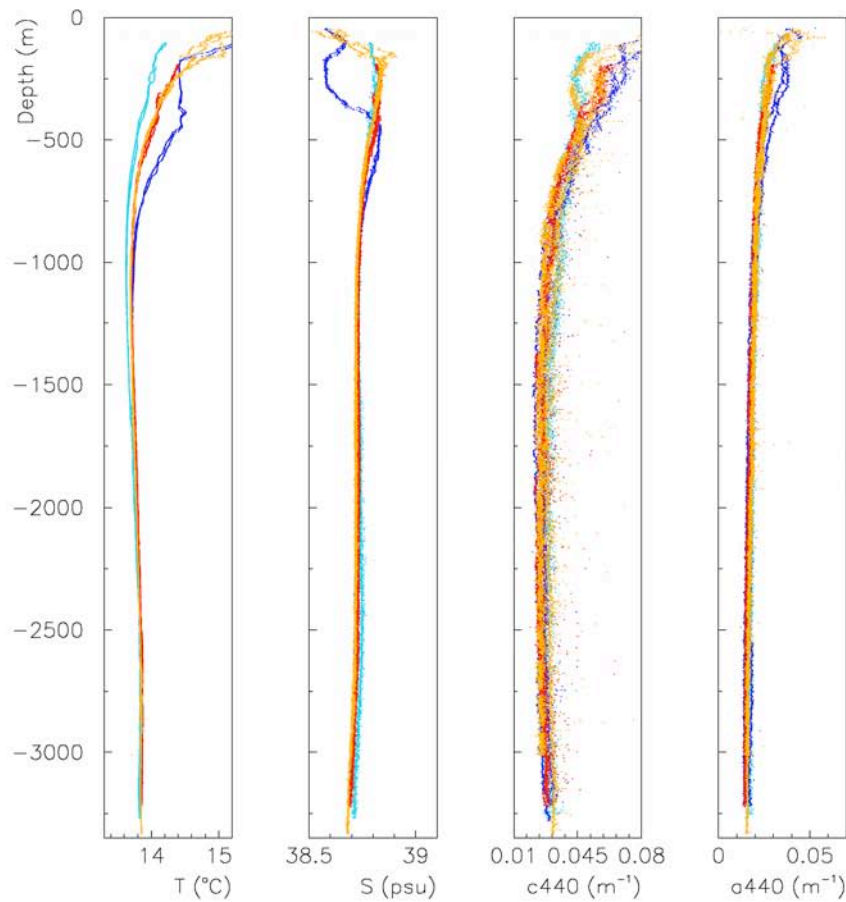


Figure 2.6 – Profiles of temperature (T), salinity (S), attenuation coefficient (c) and absorption coefficient (a) at 440 nm, measured in the Capo Passero KM4 site. The profiles refer to different campaigns: March (yellow), May (blue), August (red) and December (light blue)

and attenuation lengths, averaged for depths greater than 2850m, are shown, as a function of λ , in figures 2.7 and 2.8. There is no evidence of a seasonal dependence of the optical parameters. We can therefore conclude that optical properties in Capo Passero KM4 are constant over the whole year.

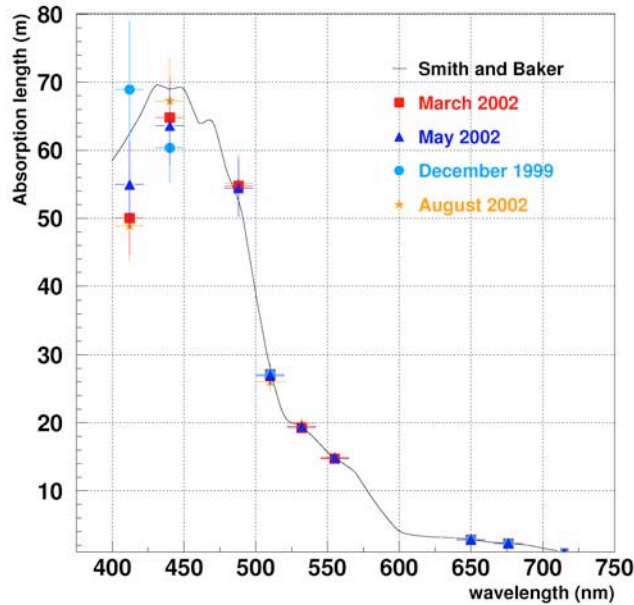


Figure 2.7 - Values of average absorption lengths as a function of wavelength, measured during four periods of the year in Capo Passero KM4.

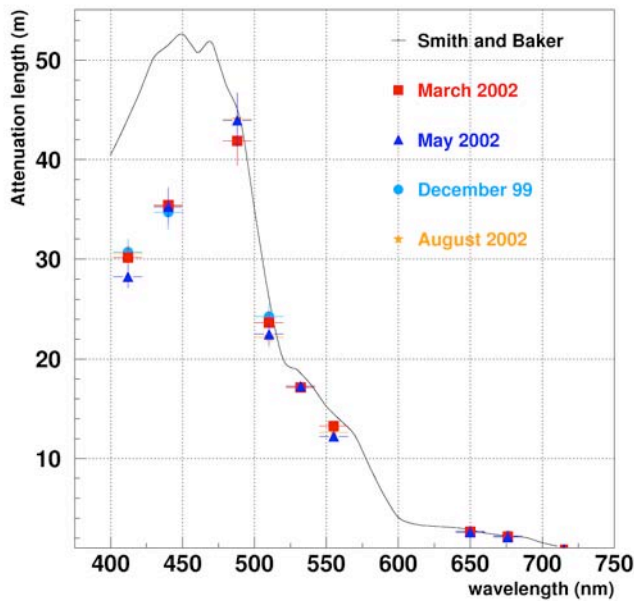


Figure 2.8 - Values of average attenuation lengths as a function of wavelength, measured during four periods of the year in Capo Passero KM4.

- **Optical properties in NESTOR site.**

Measurements of deep-water transparency in South-West of Greece

The purpose of this paragraph is to summarize experimental data of water transparency that have been obtained in the NESTOR site so far. The NESTOR site is situated on the bottom of the Ionian Trench near the foot of continental slope 20 miles SW of Pylos and 10 miles south of Sapienza Island (fig.2.9). Two methods were used:

- The measurement of the attenuation of a well collimated light beam ("good" geometry photometry).
- The measurement of the transmission distance with non-collimated light ("open" geometry photometry).

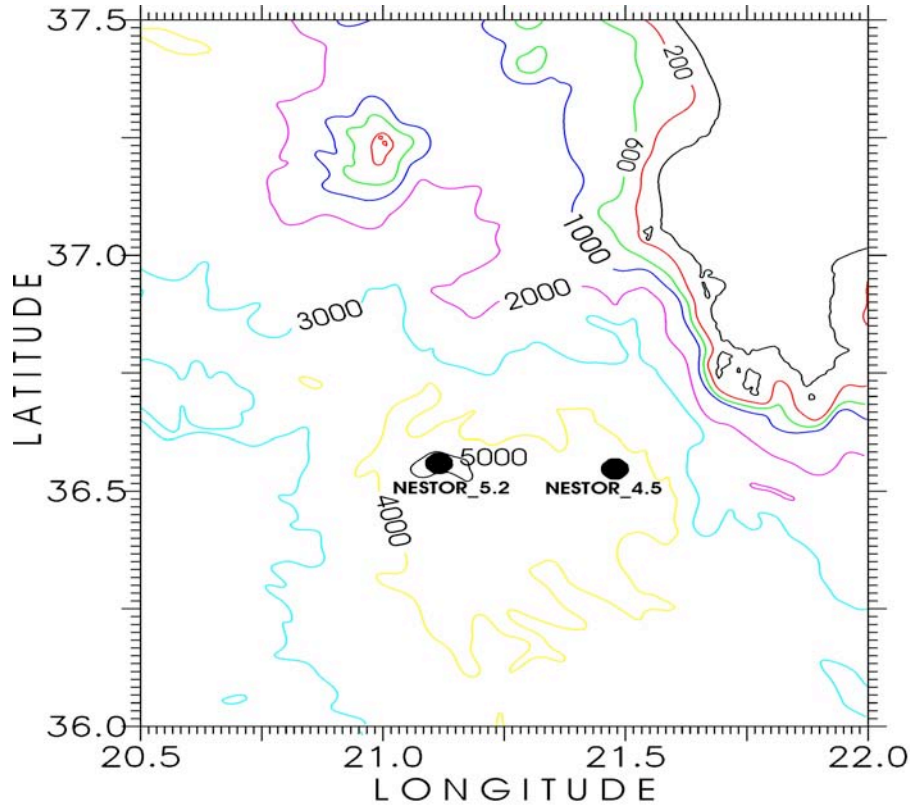


Figure 2.9: Study area with topographic contours in m. Numbers '5.2' and '4.5' indicate site depth in km.

A. Measurements with "good" geometry photometry

The water transparency in the Nestor Site was studied during the 29th cruise of "Akademic Keldish" (October-November 1992) with the measurement of the attenuation of a well-collimated light beam ("good" geometry photometry).

The spectrum of the attenuation coefficient was measured with a diffraction grating spectrophotometer, as shown in figure 2.10. Two cells were used, the "long" cell was 1.10m long and the "short" cell 0.10m long. The light source was an ultraviolet lamp and a photomultiplier was used as a photo detector [8].

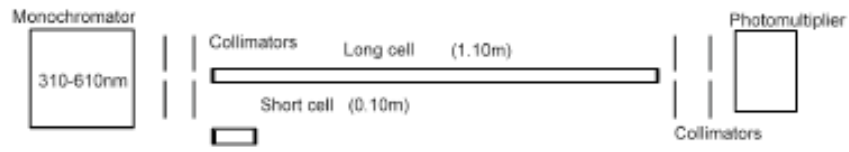


Figure 2.10 - Diagram of the spectrophotometer.

In the following tables (and in figures 2.11a, b, c and d), information about the transmissivity of samples obtained at 7 locations has been tabulated. In each location the figure of the attenuation versus wavelength with depth as a parameter is displayed and the estimated attenuation at 460nm is printed. The estimated attenuation has been extracted from the figures and the reading error is roughly 0.005. In figures 2.12 the light attenuation coefficient of 460nm wavelength versus the depth is plotted for all the locations.

Table 2.3 - Information about the attenuation coefficients from several locations.

Latitude	Longitude	Attenuation at 460nm		Figure 2.11a - Attenuation coefficient vs wavelength (with depth as a parameter)
		Depth (m)	Attenuation (m ⁻¹)	
36° 37.2'	21° 30.9'	0	0.06	
		70	0.14	
		500	0.065	
		1500	0.04	
		2500	0.06	
		3500	0.105	
		3870	0.029	
36° 37.2'	21° 33.4'	0	0.12	
		3000	0.045	
		3663	0.03	
		3713	0.03	
		3763	0.03	
		3813	0.03	
		3860	0.03	

Latitude	Longitude	Attenuation at 460nm		Figure 2.11b - Attenuation coefficient vs wavelength (with depth as a parameter)
		Depth (m)	Attenuation (m ⁻¹)	
36° 29.0'	21° 30.0'	0	0.1	
		3000	0.09	
		3500	0.04	
		3993	0.05	
36° 32.7'	21° 29.0'	0	0.04	
		2500	0.087	
		3000	0.06	
		3480	0.06	
		4000	0.045	

Latitude	Longitude	Attenuation at 460nm		Figure 2.11c - Attenuation coefficient vs wavelength (with depth as a parameter)
		Depth (m)	Attenuation (m ⁻¹)	
36° 36.9'	21° 32.1'	0	0.115	
		200	0.05-0.055	
		3608	0.035	
		3660	0.05-0.055	
		3734	0.05-0.055	
		3864	0.040	
36° 36.9'	21° 34.0'	0	0.115	
		2000	0.045-0.05	
		3000	0.045	
		3500	0.06	
		3814	0.05	

Latitude	Longitude	Attenuation at 460nm		Figure 2.11d - Attenuation coefficient vs wavelength (with depth as a parameter)
		Depth (m)	Attenuation (m^{-1})	
36° 37.1'	21° 30.1'	0	0.11	
		70	0.175	
		200	0.08	
		500	0.05-0.06	
		1000	0.05-0.06	
		2000	0.05-0.06	
		3000	0.048-0.050	
		3500	0.03-0.04	
		3800	0.049-0.051	

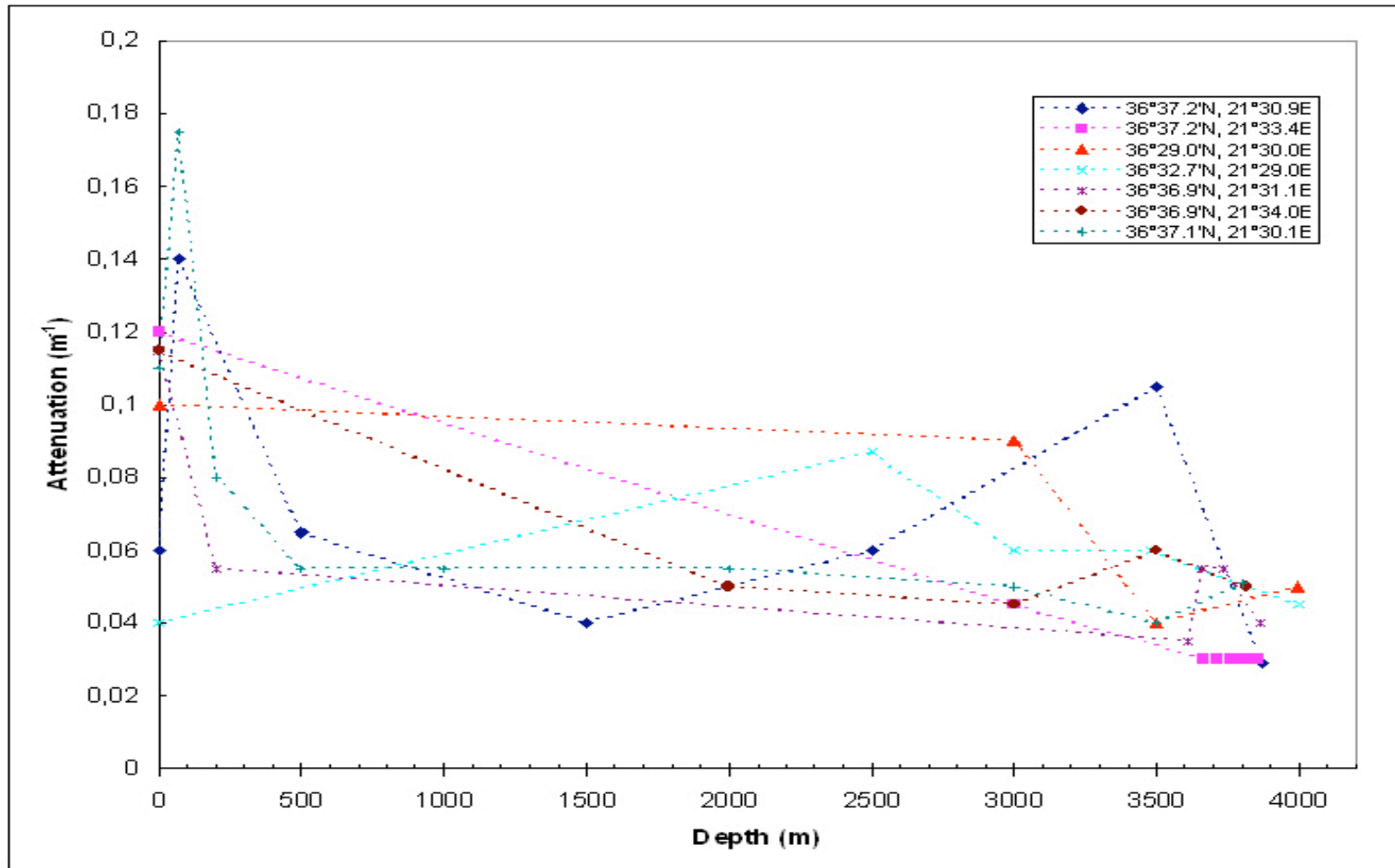


Figure 2.12 - Attenuation coefficient versus depth at 460nm wavelength.

B. Measurements with "open" geometry photometry

Measurements of the transmission distance have been made with the “open geometry photometry” method. In this method, a non-collimated light is used at three locations within the Nestor Site for the measurement of the transmission distance.

The detector used for the measurements is a two-part instrument, the light source, a blue-green (460 nm) filter and the photo detector. The two parts are joined together with a variable length wire rope 3mm thick, fig. 2.13:

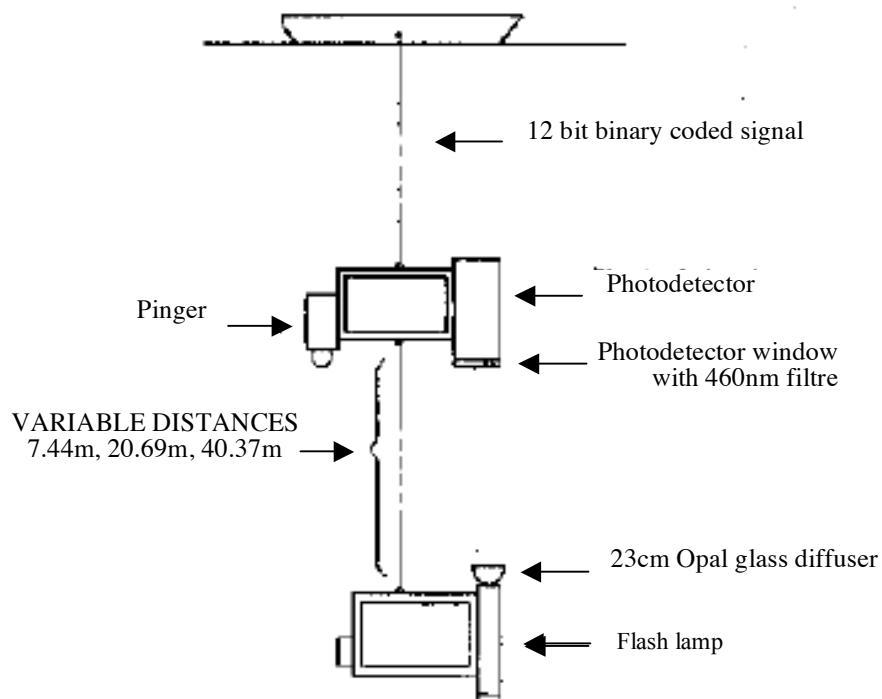


Figure 2.13 - Schematic diagram of the detector

Measurements were made at various depths down to about 4000m, using three distances between the light source and the photo detector; 7.44m, 20.69m and 40.37m. A transmission length of (55 ± 10) m describes the deep data satisfactory. Additional information is found in [9, 10]. The results measured from this experiment are shown in table 2.4.

Table 2.4 Information about the transmission distance from three locations. In the inset the location of the sample collection is shown

Latitude	Longitude	Sea bottom (m)	Depth (m)	Transmission distance (m)	Figure 2.14
36° 37'	21° 34'	3727	200	40 ± 8	
			1000	52 ± 11	
			2000	52 ± 11	
			3000	52 ± 11	
			3500	52 ± 10	
			3650	54 ± 10	
36° 29'	21° 30'	4160	1000	52 ± 10	
			3500	55 ± 17	
			3900	52 ± 11	
36° 34'	21° 16'	3600	100	36 ± 6	
			1000	58 ± 13	
			2000	45 ± 8	
			3000	46 ± 7	
			3500	52 ± 5	

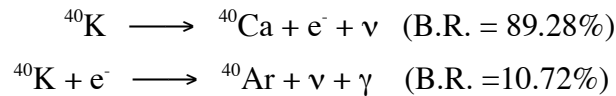
3. Measurements of the optical background

- **Sources of optical background in seawater**

The Optical Modules counting rate in an undersea neutrino detector is strongly affected by two kinds of natural causes: the decay of radioactive elements diluted in water and the luminescence produced by biological entities (we will refer to this contribution simply as “bioluminescence”).

Background from radioactive decay

Of all the radioactive isotopes present in natural seawater ^{40}K is by far the one that contributes the most to its total radioactivity. Both ^{40}K decay channels



contribute to the production of optical noise. A big fraction of electrons produced in the first reaction is above threshold for Čerenkov light production. The photon originated in the second reaction has $E_\gamma \approx 1.46$ MeV and can therefore originate electrons over threshold for the Čerenkov effect.

For obvious reasons the flux of Čerenkov photons originated by ^{40}K radioactive decays depends mainly on ^{40}K concentration in seawater. The very small variations of salinity in the Mediterranean Sea suggest that we have to expect very small variations of the luminescence produced by radioactive isotopes from site to site. In the Capo Passero site, as an example, the salinity at 3300 m amounts at $S \approx 38.7$ g/l. Knowing the contribution of potassium to the total salinity (ε_K), the relative abundance of ^{40}K isotope ($\eta_{^{40}\text{K}} = 1.17 \times 10^{-4}$) and its mean life time ($\tau_{^{40}\text{K}} = 1.277 \times 10^9$ y) we can evaluate the total number of radioactive decays per unit of sea water volume:

$$N = \frac{\ln(2)}{\tau_{^{40}\text{K}}} S \cdot \varepsilon_K \cdot \eta_{^{40}\text{K}} \cdot \frac{N_A}{40} = 13600 \text{ m}^{-3} \text{ s}^{-1}$$

The volume of water seen by an optical module has a radius $\approx L_a$. Therefore; we expect a huge number of photon hitting the PMT photocathode. Several measurements carried out by DUMAND, NESTOR, ANTARES, NEMO have shown that the contribution of ^{40}K to the “optical noise” on PMT with large photocathode (8”÷13” diameter) can rise up to 40÷80 kHz. The evaluation of the total flux of photons produced by ^{40}K in seawater can be carried, from direct measurements with Optical Modules, only taking into account photons propagation (in water, glass, optical gel, ...), detector properties (photocathode sensitivity and quantum efficiency), geometrical acceptance, etc...

Bioluminescence

Bioluminescence is mainly produced by bacteria emitting light at the level of single photon intensity. A high level of bacteria concentration can give rise to an optical noise several orders of magnitude more intense than the one due to ^{40}K .

Not too much is known about bioluminescence at high depth. Data reported in the literature show the typical spectra (see fig. 3.1) of the emitted radiation, centred in the region where the water transparency is maximal and, unfortunately, of interest for undersea Čerenkov neutrino telescopes.

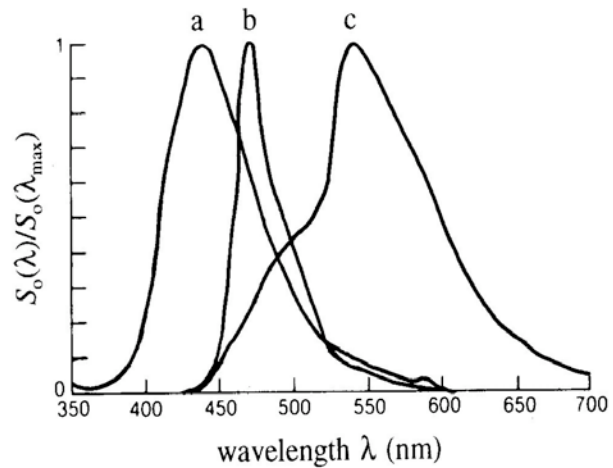


Figure 3.1 – Emission spectrum for three biological organisms: a) the arthropod *Scine*; b) the *Dinoflagellata Pyrocystis*; c) the bacterium *Vibrio fischeri*.

From a campaign of measurements in the region of Capo Passero, carried out in collaboration with the Istituto Sperimentale Talassografico di Messina (CNR), important information about the distribution of luminescent bacteria in a vertical column of water was determined. As it appears from fig. 3.2 the presence of these bacteria depends on the depth and their presence at more than 2500 m is negligible.

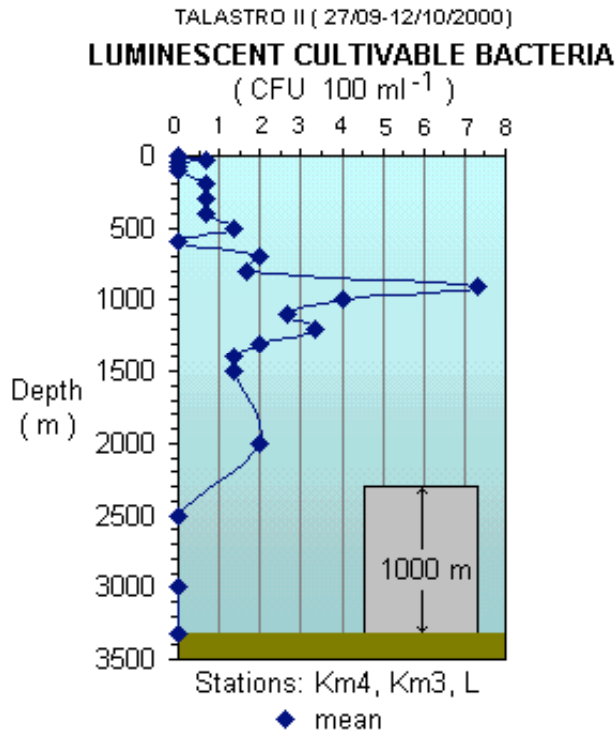


Figure 3.2 - Amount of luminescent cultivable bacteria in Capo Passero as function of depth.

Vertical Profiles of Bioluminescent Bursts

Ninety-seven percent of planktonic organisms in the water column have the ability to produce bioluminescence for a variety of ecological reasons. Drifting gelatinous organisms will to some degree produce spontaneous natural bursts of light that will be detected by the telescope. These bursts of light are increased in the presence of a stationary object in the water such as moored instruments. The animals drifting in the currents can impact the object and emit light on contact. These animals, often transparent and extremely fragile, have proven difficult to study with conventional sampling. Mechanically stimulating bioluminescence during a CTD cast produces a marker for each individual, therefore vertical profiles of bioluminescence can be used as a proxy for pelagic community structure and indicate spatial and temporal levels of potential impact-bursts on an underwater neutrino telescope

To induce these bioluminescent events, an ultra low-light camera (ISIT camera) is positioned on the CTD probe looking down on a black mesh screen. As the CTD is lowered through the water, organisms impacting or passing through the screen will produce bioluminescence by mechanical stimulation. The video profiles and data is pre-programmed, controlled, powered and stored autonomously inside a custom-built control unit on the CTD frame.

• **Measurement of the optical background in the ANTARES site**

The ANTARES Collaboration has performed a series of in situ measurements to study the background light. Such measurements were made at two sites in the Mediterranean Sea, the ANTARES site (42°50' N, 6°10' E) at a depth of 2430m and a site 20 nautical miles off Porto, Corsica, (42°22' N, 8°15' E) at a depth of 2680m. These dedicated tests were performed using 8-inch photomultiplier tubes (PMTs) on autonomous device systems [11].

Counting rates measured during 1997-1998 campaigns were acquired with a threshold of 0.3 or 2.0 photoelectrons. A typical time stream is shown in figure 3.3, on which two components can be identified: a continuum base rate of a few tens of kHz, varying slowly on time-scales of a few hours, and sharp peaks lasting a few seconds and rising to tens of MHz.

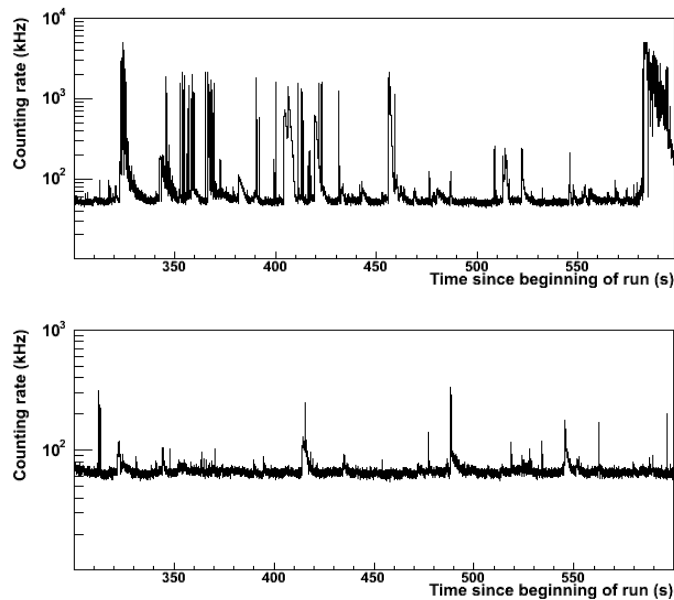


Figure 3.3 - PMT counting rates, as function of time, with a threshold of 0.3 pe.

The continuous component of the background light never exceeded 47 kHz during all these campaigns, as indicated in table 3.1. This background level varies simultaneously on all optical modules, even when located 40 m apart, and is not correlated with the sea current velocity. Knowing that the water salinity is constant in time, the ⁴⁰K contribution is expected to be constant too, unless the water transparency fluctuates by a large amount. So variations of the continuous component are probably caused by a variable bioluminescence component.

Test	Time of year	Location	Background (kHz)	
			Minimum	Maximum
1.6	Oct. 97	ANTARES	37	47
1.7	Oct. 97- Feb. 98	Corsica	24	27
1.8	Mar. 98-Apr. 98	ANTARES	20	34

Table 3.1 - Variation of the level of the continuous component of the background light (8'' PMT).

Light bursts observed in the counting rates are probably due to the passage of light emitting organisms near the detector. Periods of high burst activity are not correlated with variations of the continuous component, suggesting that different populations are involved in each process. Moreover, a strong correlation is observed between burst activity and the current velocity, as shown in figure 3.4. Finally, there is a clear indication for correlation between the periods of burst activity of two optical modules located near one another (0.55 m or 1.4 m), whereas this correlation is negligible for distant optical modules (40m).

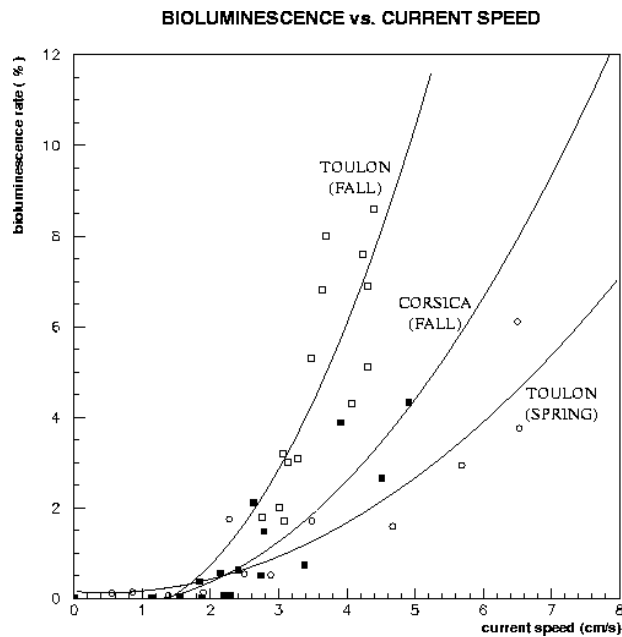


Figure 3.4 - Correlation between the burst rate and the current velocity, for all the three tests led during 1997-1998 campaigns. A fit with a second-degree polynomial is superimposed on top of the data from each individual test.

More recently, a prototype line and an instrumentation line were immersed at the ANTARES site. The prototype line, called PSL, was connected to the ANTARES Junction Box at a depth of 2475 m during three months in 2003. It was composed of five storeys of three optical modules each.

The continuous component of the recorded data is shown in figure 3.5 for the four working storeys of the PSL. These baseline rates showed a high bioluminescence activity with large variations, knowing that the ^{40}K contribution is constant and about 40 kHz for these PMTs (Hamamatsu 10 inches PMT). These variations, much higher than the ones observed in 1997-1998, are highly correlated between optical modules, even for those distant of 50m (between the first floor and the last one). Observation of large variations of the baseline was confirmed when the ANTARES instrumentation line, called MILOM [12], was immersed and connected in April 2005, cf. figure 3.6. This continuous component is neither correlated with sea current, nor with burst frequency.

Concerning burst frequency, a correlation with the sea current was confirmed, as illustrated in figure 3.7.

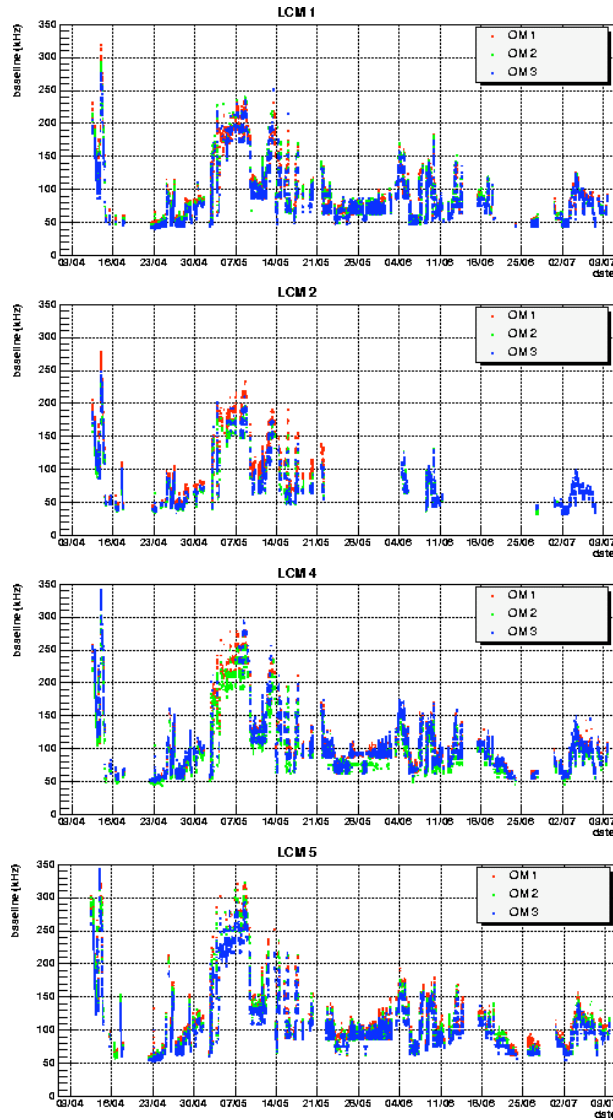


Figure 3.5 - Continuous component of the PMT counting rates of the PSL in 2003, as function of time.

A hypothesis is to say that this continuous background is due to luminescent bacteria, which emit light by long glows. Complementary sea campaigns called NOCTILUC [13] and led with the help of biologists from the CNRS/INSU/Centre d’Océanologie de Marseille, have shown that luminescent bacteria were present at the ANTARES site.

Anyway, the noticeable conclusion of all these optical background studies is that level of bioluminescence can extensively vary from one year to another one, and measurements on several years are necessary to give conclusions on biological luminescent activity.

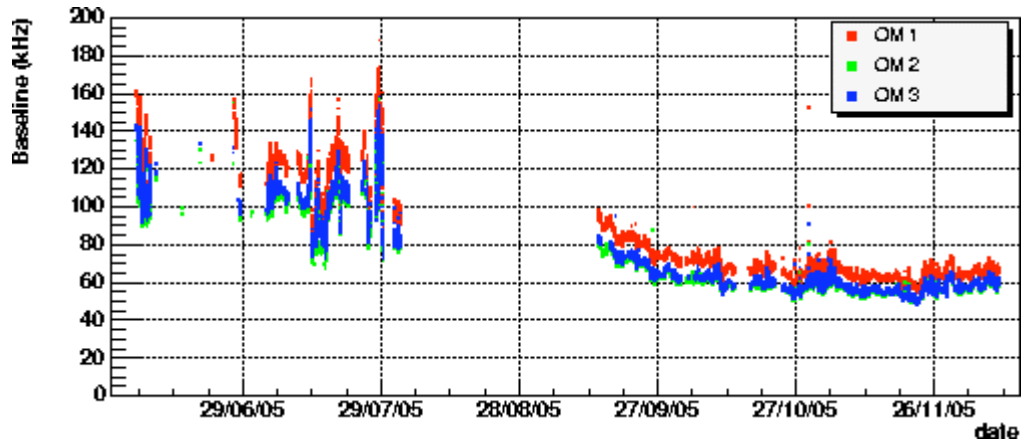


Figure 3.6 - Continuous component of the PMT counting rates of the MILOM in 2005, as function of time.

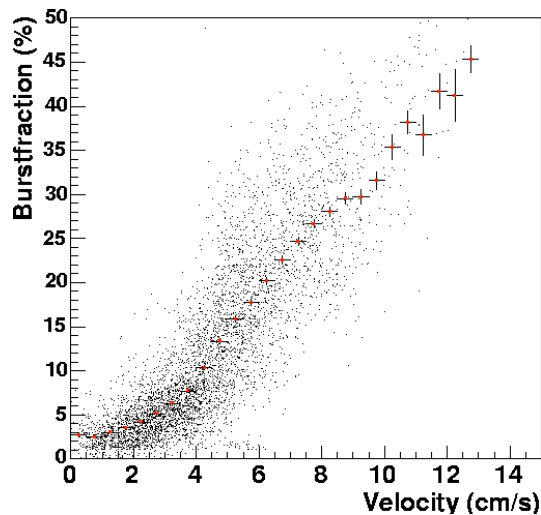


Figure 3.7 - Correlation between the burst fraction and the current velocity, for the data taken with the MILOM in 2005 .

Bioluminescent burst profiles at the ANTARES site

During two campaigns to the ANTARES site (42°48'N, 6°10.70'E) in 2004 a total of 4 vertical profiles were carried out. There were two stations; the ANTARES site and control site further offshore. The ANTARES site was sampled once in January and once in May. Bioluminescent activity was far greater in May than in January as an effect of the increase of primary production (or 'spring bloom') present in the surface layers during the Spring months. Both seasons show a typical decrease of bioluminescence with depth from the surface to the seafloor (~2400m). The mean number of bioluminescent events per metre cubed at the ANTARES site between 1000 and 2500m were 1.78 (in January) and 4.4 (in May).

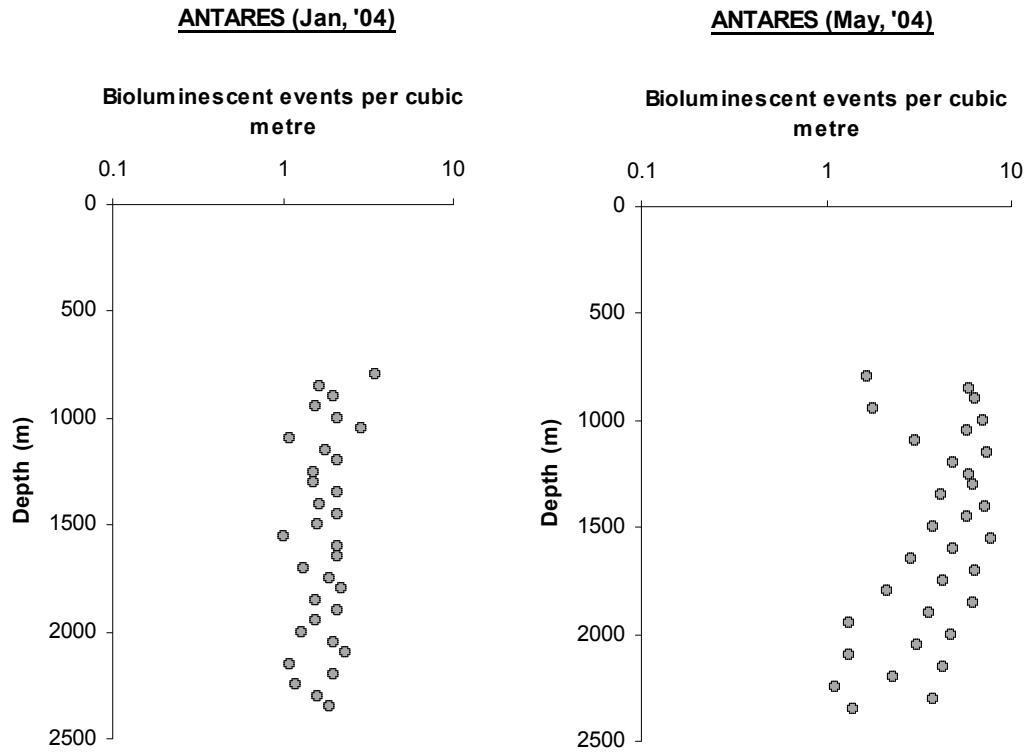


Figure 3.8 - Vertical profiles of pelagic bioluminescence at the ANTARES site in January and May .

- **Measurement of the optical background in the Capo Passero site**

Data in Capo Passero were collected by means of two different setup. One, built by NEMO Collaboration, consisted in two 8" photomultipliers and the associated electronics, the second, built by the ANTARES Collaboration, used an optical module containing a 10" photomultiplier. The two apparatus have been used to collect data separately but also together in order to compare the results and to avoid systematic errors. Pulses collected by the PMTs are induced mainly single photo-electron. The optical noise background is characterized by the PMT photocathode area and by the threshold fixed for pulse height collection. Figures 3.9 and 3.10 show results obtained

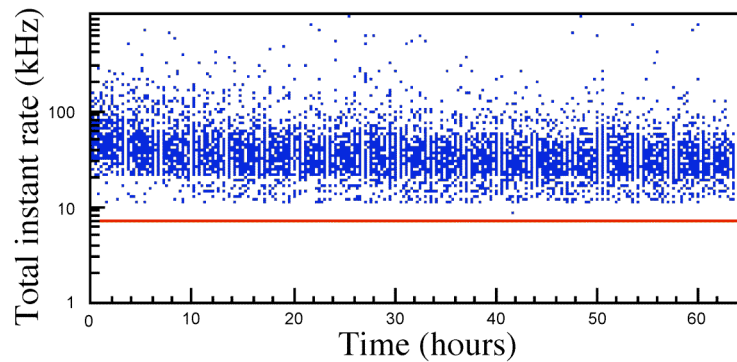


Figure 3.9 - PMT total instant rate, as function of time, for data collected in KM4. The red line indicates the level of "dark current noise", due to the PMT, to be subtracted.

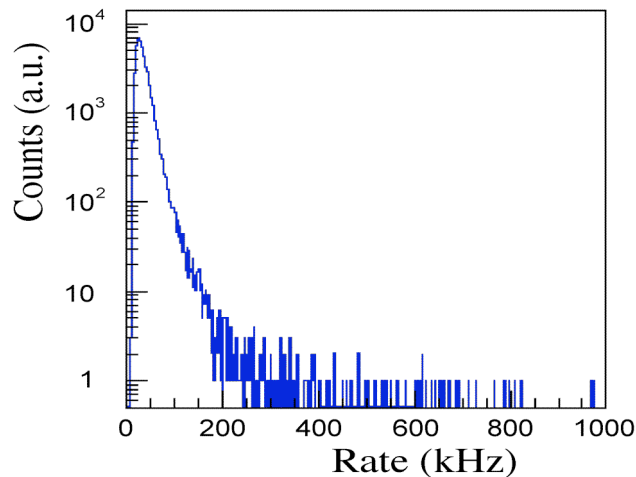


Figure 3.10 – PMT total instant rate distribution for data collected in KM4. The contribution to the total instant rate due to the PMT "dark current noise", that amounts to ~ 7 kHz, is not yet subtracted.

with the NEMO setup: 8" diameter PMT (355 cm^2 sensitive photocathode area) with a threshold equivalent at 0.33 p.e.. In fig. 3.9 is represented the PMT instant rate as a function of the time, fig. 3.10 shows the instant rate distribution. From these figures we

can easily see that the total measured instant rate value fluctuates from 20 kHz to 200 kHz and very rarely exceeds this higher value.

As results we obtain that the optical noise induced on a 8” PMT, subtracting from the total instant rate the 7 kHz due to the PMT “dark current”, amounts then to

$$f_{\text{optical noise}}^{KM4} \approx 28.5 \pm 2.5 \text{ kHz}$$

This noise is quite constant and shows only rare emissions of light in bursts, typical of “bioluminescence”.

Comparing this result with the expectations of a MonteCarlo simulation, that includes all knowledge about the PMT behaviour and the optical properties of deep sea water in KM4 site, NEMO Collaboration conclude that in average the flux of photons due to “optical noise” in Capo Passero, that can be detected by a bialkali PMT, amounts to

$$\Phi_{\text{optical noise photons}}^{KM4} = 360 \pm 40 \text{ photons} \cdot \text{cm}^{-2} \cdot \text{s}^{-1}.$$

• **Measurement of the optical background in the NESTOR site**

In this paragraph we summarize experimental data of optical background that have been obtained in the NESTOR site, on the bottom of the Ionian Trench near the foot of continental slope 20 miles SW of Pylos and 10 miles south of Sapienza Island. Data were collected using:

- A number of free-drop experiment deployed starting around 1996 at a depth of 4000m at the NESTOR site in order to measure Optical Module background in deep-sea; schematic is shown in fig.3.11. It composed of two Optical Modules with the required electronics inside a 1m-diameter titanium sphere. The system usually was deployed for a few days. In figure 3.12, data recorded for a few minutes, randomly chosen from the data set, shows clearly a few seconds increase of Optical Module rate above the mean rate;

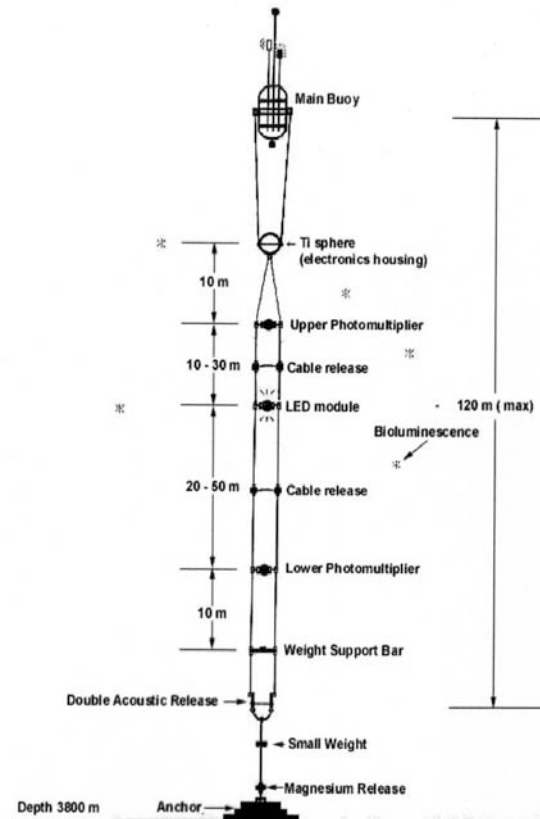


Figure 3.11 - Schematic of the free-drop

this increase is attributed to bioluminescence and it happens at 1% of the total data taking time.

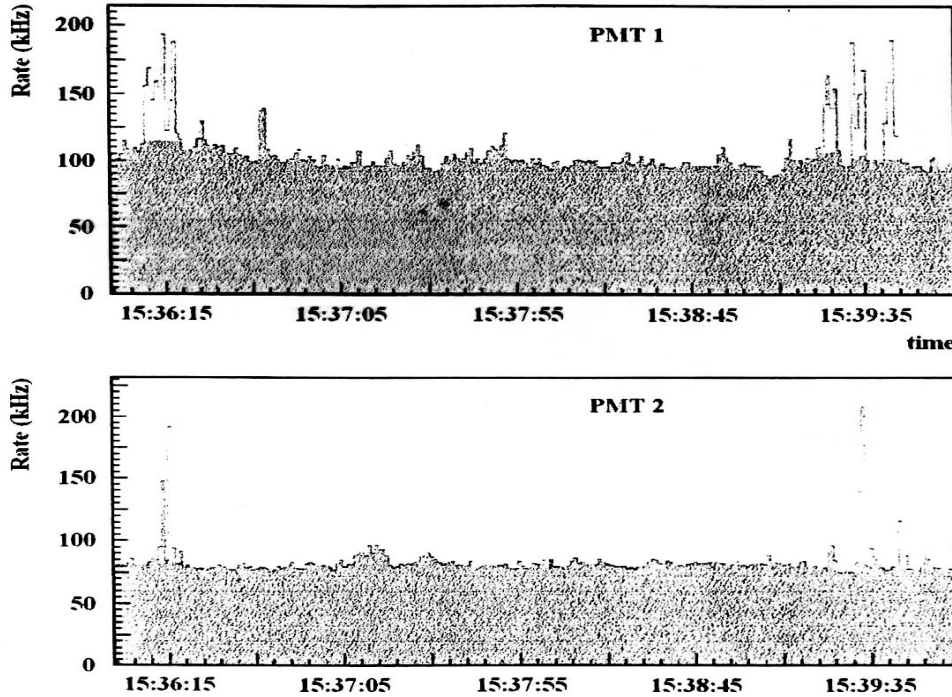


Figure 3.12. Data sample of the free-drop experiment; bioluminescence burst is clearly shown.

- B NESTOR floor, connected in real time via an electro-optical cable to shore, deployed in 2003. It was equipped with 12 Optical Modules in pairs at the end of six-arm titanium star; six with photocathode looking upwards (up-looking) and six downward (down-looking). The required electronics were installed in a 1m-diameter titanium sphere at the centre of the star and data were collected in real time through an electro-optical cable to shore; schematic is shown figure 3.13. A data sample of 100s, randomly chosen, is shown in figure 3.14. It is clearly shown that during this time period, a couple of a few seconds excesses of the Optical Module rate were recorded; those signals are attributed to bioluminescence. It is also obvious that those particular light sources were above the star since only the up looking Optical Modules detected clearly those signals. During this experimental period, bioluminescence occurs at $1.1\% \pm 0.1\%$ of the Active Experimental Time.

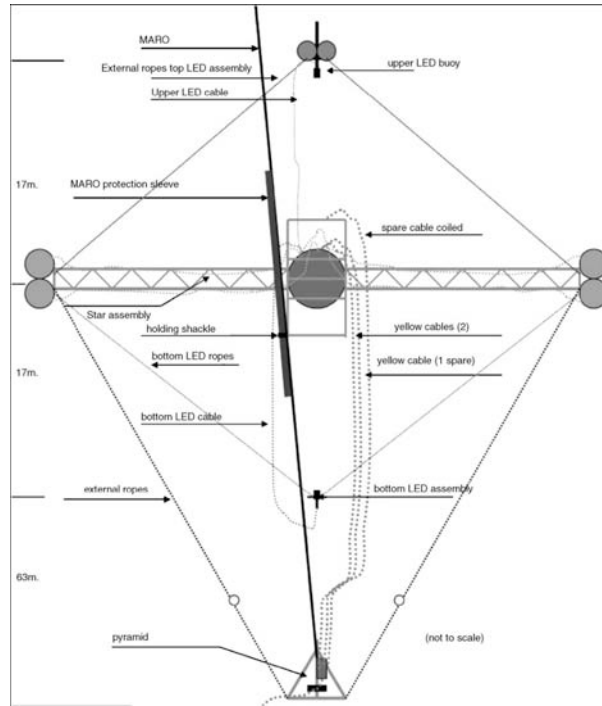


Figure 3.13 - Schematic of one NESTOR star connected to shore through an electro-optical cable

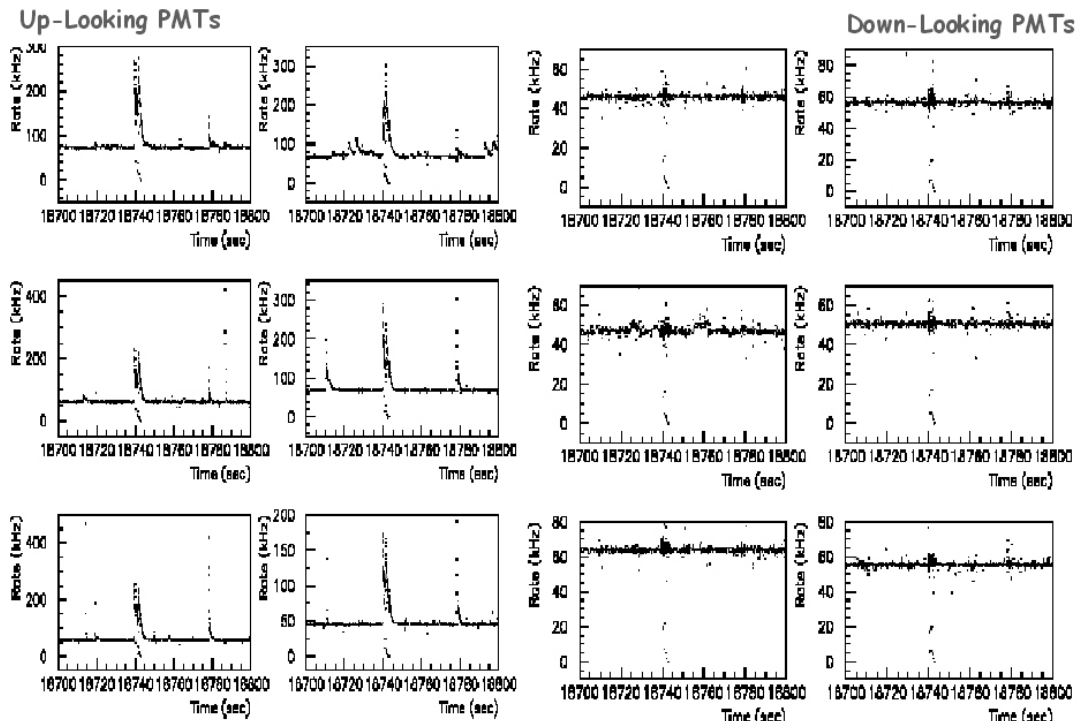


Figure 3.14 - Data sample of the NESTOR star; bioluminescence burst is clearly shown in the Optical Module with the photocathode looking upwards.

Bioluminescent burst profiles at the NESTOR site

Bioluminescent profiles were carried out close to the NESTOR site in 2006 (36°33.61N, 21°02.79E). A total of 31 profiles were carried around the Mediterranean and one was made 4nm West of the KMD site. The data showed the typical decrease of bioluminescence with depth from the surface to the seafloor (~5100m), however very little or no bioluminescent activity was observed below 3000m. In general, the bioluminescent activity at the KMD site was considerably lower in comparison with Western Mediterranean and Atlantic Ocean data. The mean number of events per metre cubed between 1000 and 2500m were 0.12.

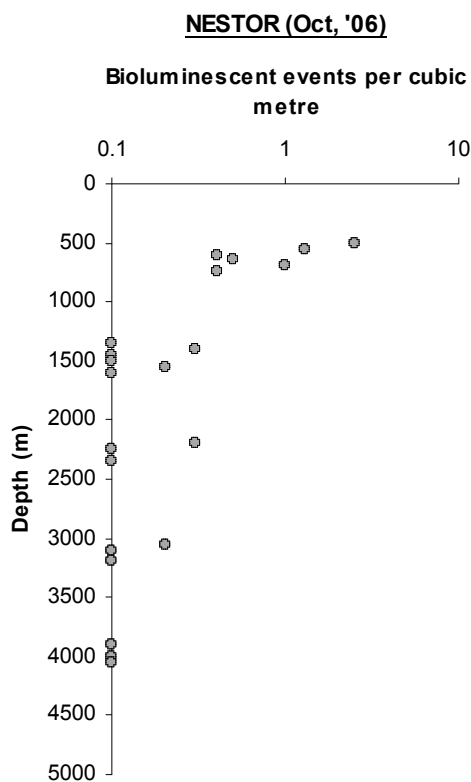


Figure 3.15 - Vertical profiles of pelagic bioluminescence at the NESTOR site in October 2006

4. Study of deep-sea currents in selected sites

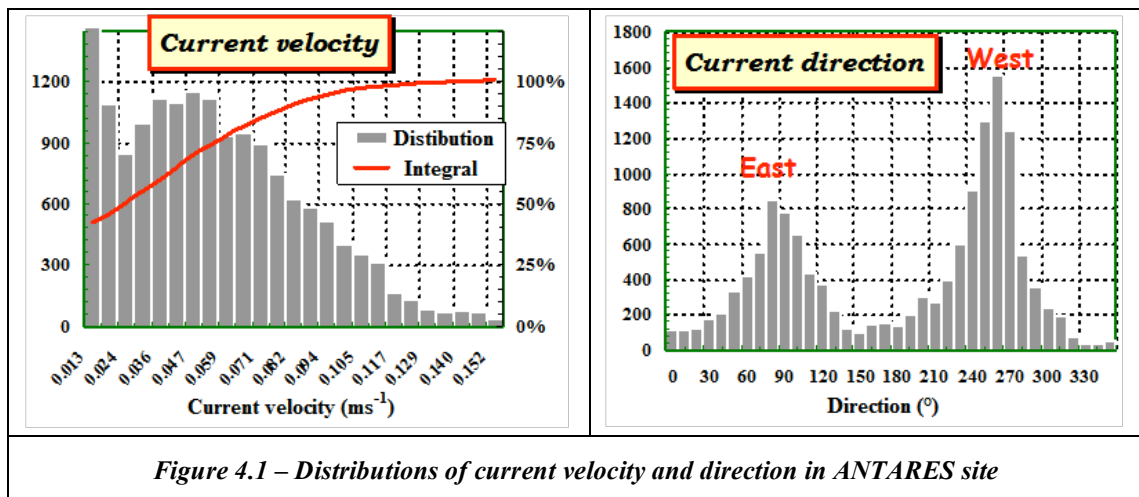
• Deep-sea currents in the ANTARES site

The measurements of deep-sea currents on the Antares site can be divided in 2 phases:

- During the exploratory phase, measurements were performed by current meters installed on autonomous mooring lines.
- Since the deployment and the connection to the shore of the instrumented line (2005/03), the measurements are continuously performed and in real time. Hence, one has a permanent monitoring of the sea current.

There is also differences in the techniques used: for the first phase, the devices used were mechanical current-meter which essentially performed a one point (in space) measurement and produced average values computed over a defined interval of time (typically few 10's of minutes). Instead, for the present measurements, we are using an ADCP (Acoustic Doppler Current Profiler) which permits to measure “instantaneous” (indeed, averaged over 1 mn) values of currents at different depths simultaneously, the vertical range being typically 100 m.

The deployment of the first autonomous line was performed in the beginning of 1997, and lasted 3 months. Since then, and up to 2005, several lines have been deployed for various durations, ensuring a partial coverage of these years, the longest immersion lasting 14 months. From this later exposure, which is representative of the others, the results are summarised in the next plots.



The left plot in fig 4.1 shows the distribution of the velocity. The saturation in the first bin corresponds to the sensitivity limit of the device ($> 1.1 \text{ cm.s}^{-1}$). The most probable value is approximately 5 cm.s^{-1} , and from the integral (red curve), one sees that, for instance, during 75 % of time, the velocity is below 6 cm.s^{-1} . On the right is drawn the distribution of the direction. There is a clear privileged axis East-West (this corresponds to the Liguria current), with a preferred direction towards West.

The data taken since 2005 have a basic periodicity of 10 minutes, and are available in real time. Furthermore, the new device gives access to the measurements along the water column, on a typical range of 100 m. It is also able to measure current down to ~ 0 . As an example, the plots in fig. 4.2 show the velocity and the direction distributions for the year 2006. They exhibit the same main behaviours than the previous ones. The plot in fig. 4.3 illustrates the time variation of velocity and direction. The short-term variations (shorter than one day) correspond to the inertial oscillations.

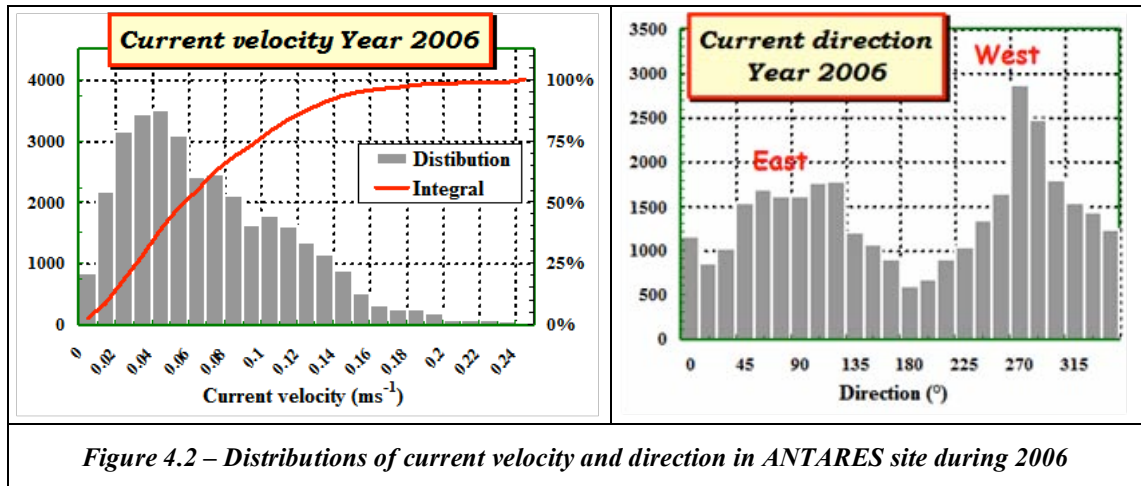


Figure 4.2 – Distributions of current velocity and direction in ANTARES site during 2006

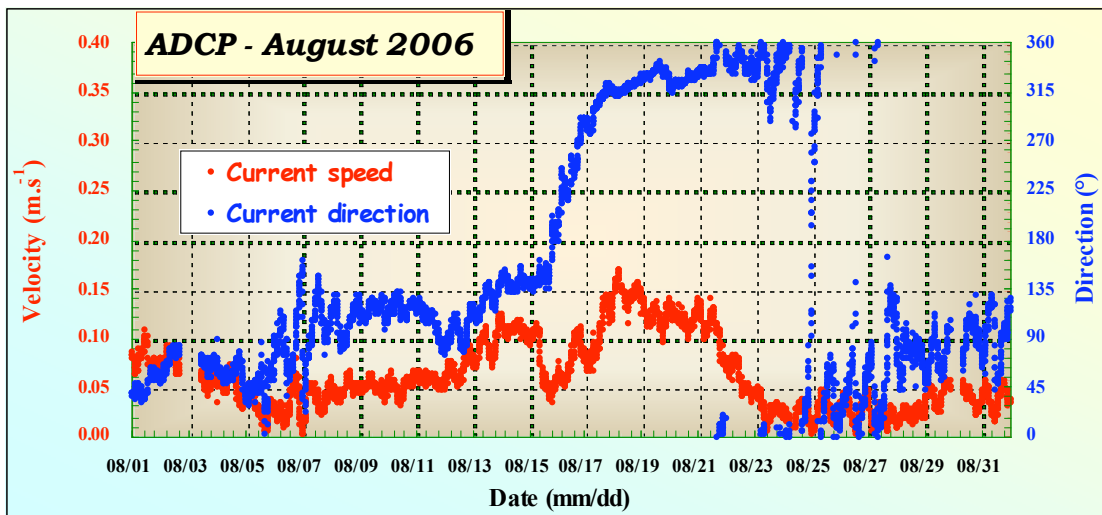


Figure 4.3 – ADCP measurement of current velocity and direction in ANTARES site

- **Deep-sea currents in the NEMO site**

Current-meter chains have been moored in the region of Capo Passero since July 1998 to measure the current intensity and direction in a range of ~ 500 meters above the seabed.

In the period July 1998 -December 1999 a mooring line has been positioned in the site denoted KM3 ($36^{\circ} 30' 00''$ N, $15^{\circ} 50' 00''$ E) in the region south of Capo Passero. The mooring was equipped with two current meters located at 10 m and 100 m above the sea bottom, respectively. The instruments measured currents stable both in direction and intensity: the average value was about 3 cm/s, and the maximum value was close to 12 cm/s. The current velocities measured by the instruments at the two depths were in good agreement each other: the water flowed from SE to NW and the average direction was 38° NW.

Since August 1999 a new mooring line has been positioned in the site denoted KM4 ($36^{\circ} 18' 52''$ N, $16^{\circ} 04' 42''$ E). This line was equipped with two current meters located at 100 m and 460 m above the sea bottom, respectively. The set of data from this second mooring line shows values comparable, and slightly smaller, than in the KM3 site.

A complete analysis of the current meter data for the period July 1998 – December 1999 is reported in [14]. This analysis confirms that the behaviour of the deep-sea currents in the region of Capo Passero is almost homogeneous on the part of the water column covered by the current-meters (≈ 500 m) with very low average values and peaks not exceeding 12 cm/s.

The time evolution of the current recorded in KM4 for the period August 1999 - August 2002 is shown in fig. 4.4. The current is almost stable in the northwest direction, with few more energetic events able to produce current reversal.

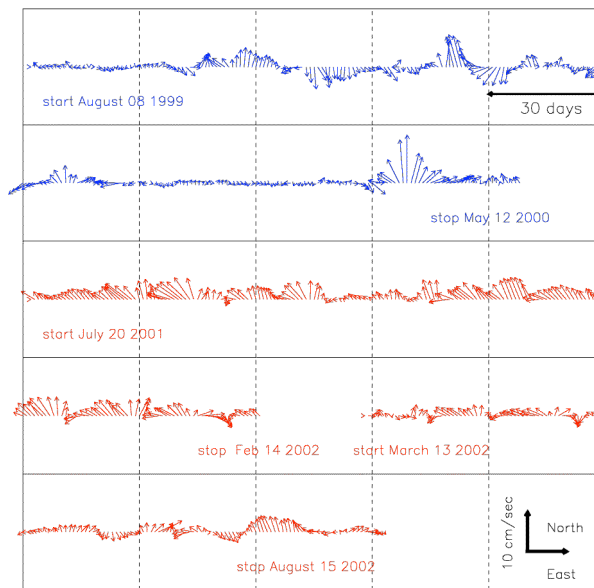


Fig. 4.4 - Stick plot of the current intensity and direction recorded in the Capo Passero KM4 site

The involved energy is generally very reduced, as evidenced by the histogram of raw data (sampling time 30 min) of the current speed (Fig. 4.5). The current speeds less than 5 cm/s accounts for the 85% of the total, while only 1% values are greater than 9 cm/s.

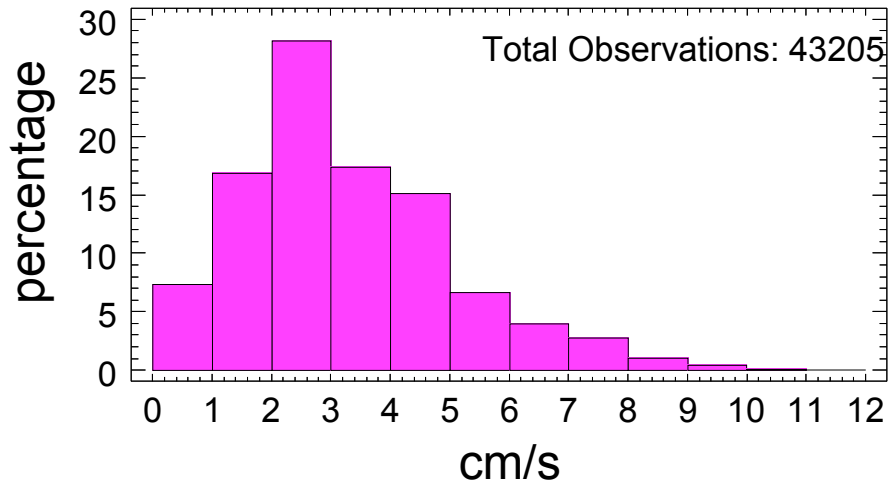


Fig. 4.5 = Histogram of the current speed for the period 1999-2004

Going to examine monthly mean values, we can envisage a weak annual cycle (Fig. 4.6). Colder months (with the only exception of March) appear more energetic than the warmer ones, with the higher speed of 4.2 cm/s during April and the weaker of 2.3 cm/s during October, suggesting a certain meteorological influence on the current. Data taking is still continuing on the KM4 site.

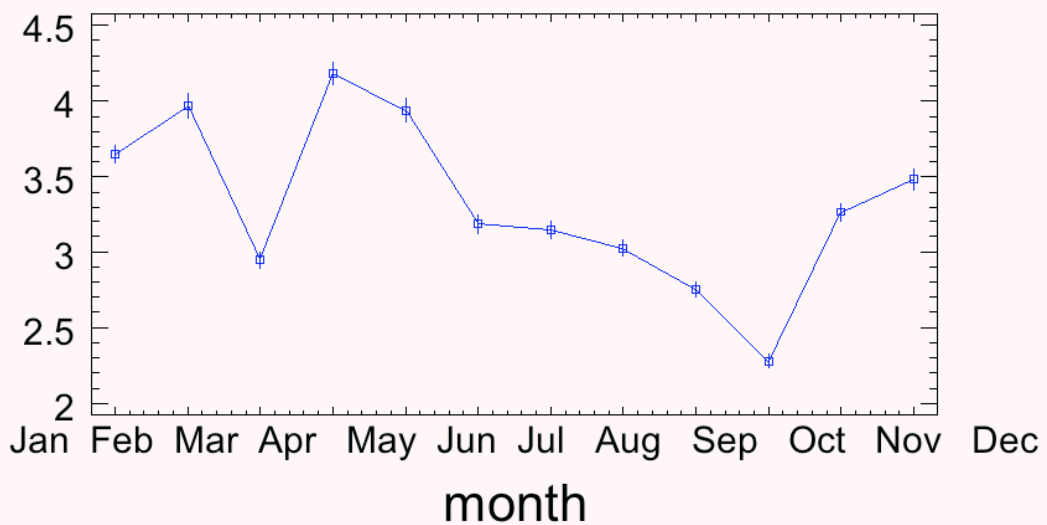


Fig. 4.6 - Monthly annual cycle of current speed.

- **Deep-sea currents in the NESTOR site**

Deep current measurements in the NESTOR area related to the tentative operation of a neutrino telescope started as early as 1989 by the University of Athens (UOA). The list below outlines the earlier current-measurement activities of UOA in the NESTOR area which took place:

- during on the 45th Cruise of R/V Dmitry Mendeleev (1989)
- during the 22th Cruise of R/V Vityaz (1991).
- during 29 cruise of the R/V Academician Mstislav Keldysh (October-November 1992).
- in 2002 with online data acquisition
- in 2003 with online data acquisition

In 1989 several subsurface deep moorings were deployed for a short period with ‘Potok’ current meters (an autonomous current meter with a propeller). In 1991, eight ‘Potok’ current meters were attached on each of two surface buoys. In 1992, there was a combination of both subsurface moorings and moorings with surface floats, all of which carried ‘Potok’ current meters [15].

In January 2002 data regarding the near-bottom current speeds at Nestor site were recorded online through a 30 km optical cable using a MARS current meter. In March 2003, a pyramid was deployed (fig. 4.7) in order to monitor and record several environmental parameters. It was equipped with a junction box, a Sensortek current meter, a sea return electrode and a transponder. The data were acquired on line through a 3 km cable [16].

Table 4.1, and figures 4.8 a, b, c and d, show all the gathered information about the currents measured at the specific locations until 2003. All raw current speeds were lower than ~4 cm/sec.

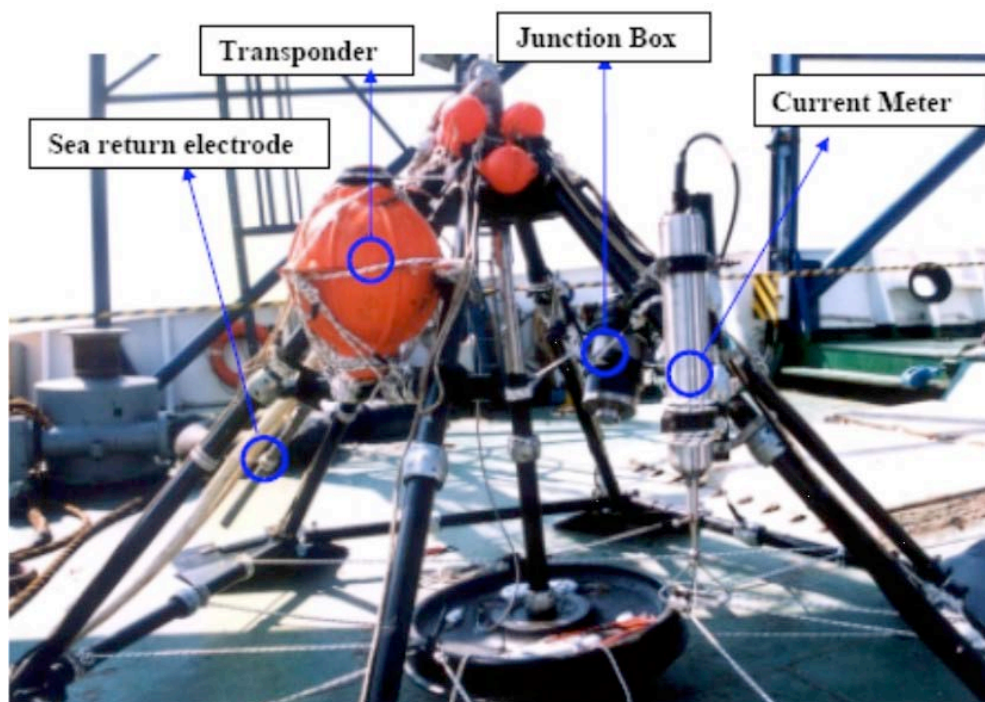
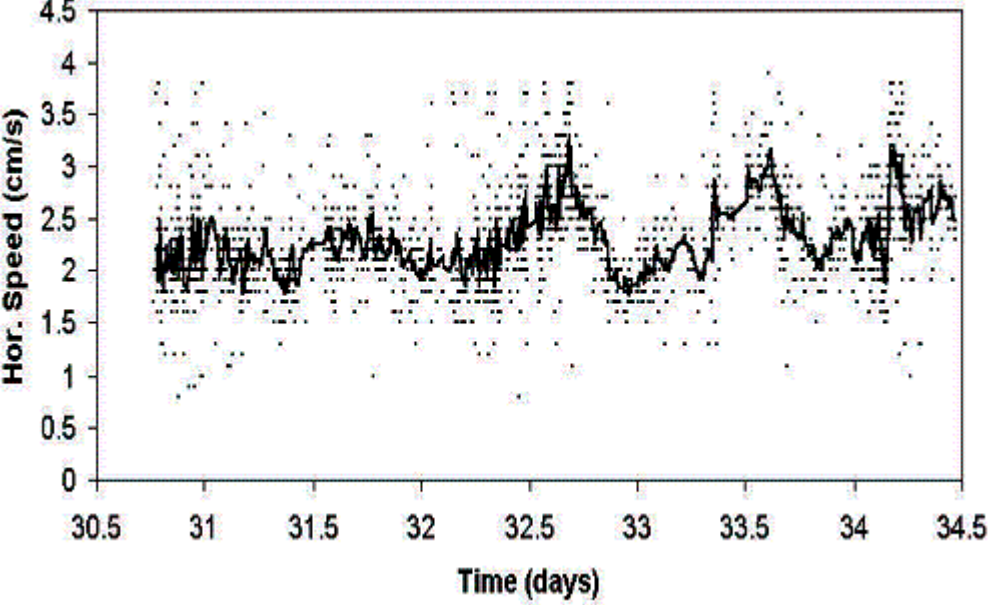


Figure 4.7. The Nestor pyramid

Table 4.1. Information on current measurements of the period 1989-2003

Date	Latitude	Longitude	Bottom Depth (m)	Distance from bottom (m)	v_{mean} (cm/sec)	Figure 4.8 a
1989	36° 32'	21° 26,50'	5110	3	1.5	
1989	36° 34,80'	21° 07'	4500	3	1.5	
1991	36° 33,00'	21° 28.75'	4250	200, 300, 500	2	-
1991	36° 37,20'	21° 34.35'	3750	200, 300, 500	2	-

Date	Latitude	Longitude	Bottom Depth (m)	Distance from bottom (m)	v_{mean} (cm/sec)	Figure 4.8 b
11/1992	36°37,00'	21°33,50'	3750	170	0.6	
11/1992	36°37,00'	21°33,50'	3750	440	1.8	
11/1992	36°37,00'	21°35'	3500	170	0.7	

Date	Latitude	Longitude	Bottom Depth (m)	Distance from bottom (m)	Figure 4.8 c
01/2002	36°38,85	21°35,99	3610	170	 <p>Figure 4.8 c is a scatter plot showing horizontal speed in cm/s over time in days. The y-axis is labeled 'Hor. Speed (cm/s)' and ranges from 0 to 4.5 with major ticks every 0.5 units. The x-axis is labeled 'Time (days)' and ranges from 30.5 to 34.5 with major ticks every 0.5 units. The plot contains numerous data points forming a dense, fluctuating band. The speed generally stays between 1.5 and 3.0 cm/s, with several distinct peaks reaching approximately 3.5 cm/s. The overall trend shows a slight increase in speed towards the end of the period.</p>

Date	Latitude	Longitude	Bottom Depth (m)	Distance from bottom (m)	Figure 4.8 d
03/2003	36°38,12	21°35,49	3720	170	<p style="text-align: center;">Figure 4.8 d</p> <p>The figure consists of two vertically stacked scatter plots, both titled 'CURRENTMETER DATA'. The top plot shows 'Horizontal speed(cm/s)' on the y-axis (ranging from 0 to 10) against 'time(h)' on the x-axis (ranging from 0 to 500). The data points show a clear diurnal cycle, with speeds peaking around 18-20 cm/s during the day and dropping to near 0 cm/s at night. The bottom plot shows 'Vertical speed(cm/s)' on the y-axis (ranging from 0 to 4) against 'time(h)' on the x-axis (ranging from 0 to 500). The data points are more scattered, generally staying between 0.5 and 2.5 cm/s, with some higher values around 3.5 cm/s.</p>

More recently, in 2006, current meter data were recovered by the HCMR (Hellenic Centre for Marine Research) from two sites in the NESTOR area of the tentative deep-neutrino-telescope to the southwest of Peloponnesus in the East Mediterranean.

Figure 6.3 shows the bottom topography of the study area and the two deployment sites, NESTOR_4.5 and NESTOR_5.2 (indicated as KMS and KMD in the figure), having bottom depths of 4.5 km and 5.2 km respectively.

Figures 4.9 and 4.10 show stick diagrams of half-hourly raw velocity time series during the deployment periods February/2006-to-May/2006 and June/2006-to-October/2006, respectively. In addition, fig. 4.9 shows U (east-west) and V (north-south) current components in which the data points with total speed lower than 2.0 cm/sec are plotted as blank. The U and V components give a preliminary idea of the time variability existing in the deep measurements with a distinct contribution from high-frequency tide-related motions.

Table 4.2 shows basic statistics of the raw half-hourly time series which for 2006 are comprised from a total of 7 records.

A fundamental feature related to the suitability of the environmental conditions of the particular area for the operation of the deep neutrino telescope is the very weak flow speeds of the deep records.

The deep flows, although not stagnant as shown by the persistence in the vectors' direction (fig. 4.9), are for most of the deployment period below instrumental threshold detection limit (Table 4.2) with speeds lower than ~1.5-2 cm/sec.

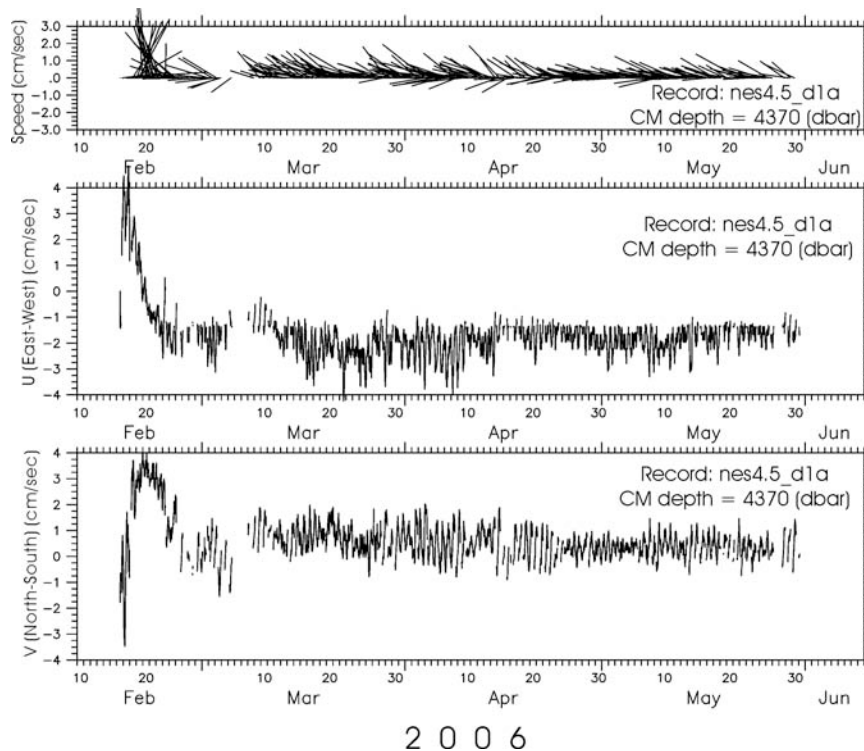


Figure 4.9 - Current-meter record of the period February/2006-May/2006 recovered from site NESTOR_4.5 (see Figure 6.3).

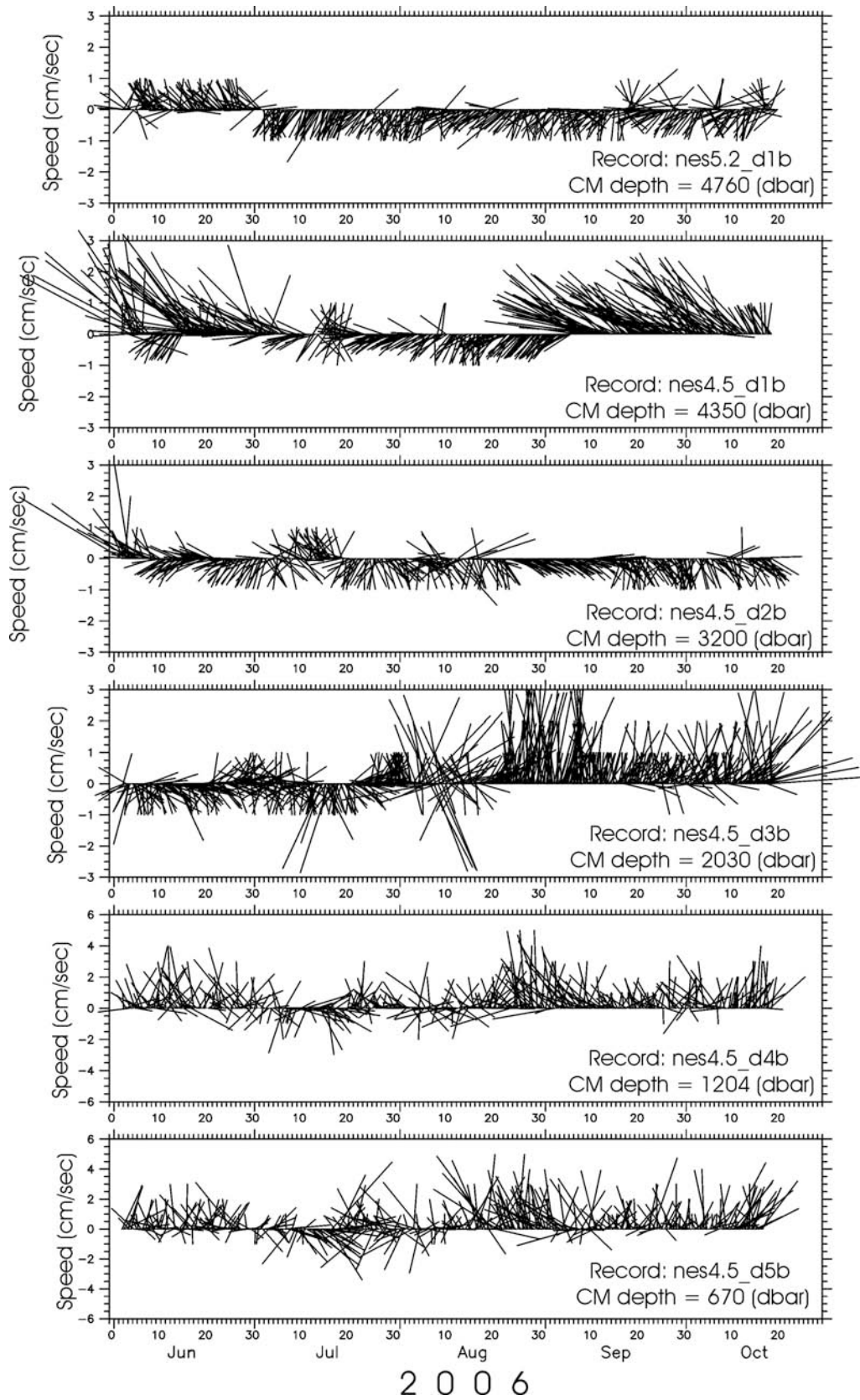


Figure 4.10 - Current-meter records of the period June/2006-to-October/2006 recovered from sites NESTOR_4.5 and NESTOR_5.2)

Table 4.2. Current meter records at the NESTOR area for the period February/2006-October/2006, and their basic statistics.

Site (4.5 and 5.2 are site- depths in km)	Record	Depth (dbar)	Deployment- Period and useful record length (days)	U min	U max	U rms	U mean	V min	V max	V rms	V mean	Speed min	Speed max	Speed rms	Speed mean	% speed values lower than 2 cm/sec
NESTOR_4.5	nes4.5_d1a	4370	16 Feb - 31 May 104	-4.2	4.8	1.0	-1.5	-3.5	4.0	0.8	0.5	1.1	5.2	0.7	1.9	22
NESTOR_4.5	nes4.5_d1b	4350	2 June - 19 Oct 138	-4.5	2.0	0.9	-1.2	-1.8	4.1	1.0	0.4	1.0	5.0	0.9	1.6	63
NESTOR_4.5	nes4.5_d2b	3200	2 June - 19 Oct 138	-2.9	2.0	0.8	0.1	-2.0	5.2	0.6	-0.4	1.0	3.0	0.2	1.0	97
NESTOR_4.5	nes4.5_d3b	2030	2 June -19 Oct 138	-3.0	2.9	0.7	0.3	-3.0	4.0	1.1	0.5	1.0	3.0	0.6	1.3	79
NESTOR_4.5	nes4.5_d4b	1204	2 June - 19 Oct 138	-5.0	4.0	1.2	-0.1	-5.8	5.8	1.3	0.9	1.0	6.0	1.0	1.7	48
NESTOR_4.5	nes4.5_d5b	670	2 June – 19 Oct 137	-5.1	4.9	1.4	0.1	-4.0	6	1.4	0.9	1.0	7.0	1.1	1.9	43
NESTOR_5.2	nes5.2_d1b	4760	2 June - 20 Oct 140	-2.0	2.0	0.5	-0.4	-2.0	1.6	0.7	-0.3	1.0	2.0	0.1	1.0	98

U is east-west current component (positive to the east); V is north-south current component (positive to the north); Speed is magnitude of total current velocity. All velocity units are in cm/sec.

5. Study of downward sediment fluxes

The analysis of the particulate material collected by a sediment trap can yield qualitative and quantitative information about the suspended matter in deep-sea waters. The aim of this study is to estimate the amount of downward sediment flux in deep waters, its composition and dimensional distribution and to have information on its time variability.

Samples were collected using sediment traps installed on the several sites explored by the ANTARES, NEMO and NESTOR Collaborations. Here we report about few experimental results.

- **Sediment fluxes in ANTARES site**

A mooring line, equipped with a sediment trap, was immersed at the ANTARES site in 1997 [17]. Mounted about 100 m above the seabed, the sediment trap (1 m² collection area) collects particles drifting towards the bottom. Sediments are collected into a series of 24 samples, based on a weekly programming. The total mass fluxes have been measured and results are shown in figure 5.1. In the summer and early autumn, low amounts of material were collected, characterized by remains of biological production (diatoms). In the second period, in autumn and winter, mass fluxes are higher, dominated by lithogenic or detrital material.

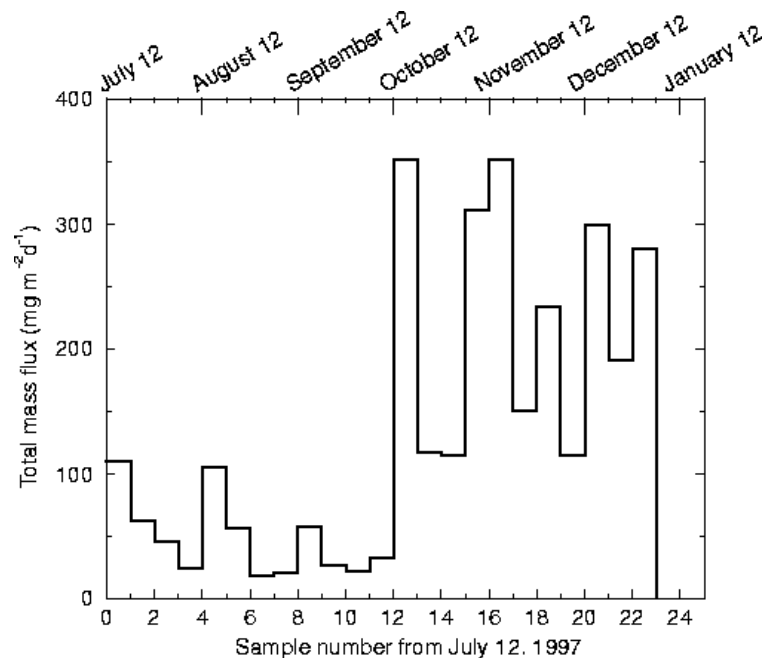


Figure 5.1 - Total mass fluxes at the ANTARES site over a six-month period, from July 12th to December 29th, 1997.

• Sediment fluxes in NEMO site

The sediment traps are usually part of “mooring lines” containing several other instruments for oceanographic studies. The trap was located at about 110 m above the seabed and programmed to collect sediment samples over periods of ≈ 15 days. Two periods of samples have been analysed: August-December 1999 and January-May 2000.

Samples collected in different periods were processed in laboratory according to [18]. The main steps of the procedure were:

- 1) manual removal of swimming organisms under a dissecting microscope and
- 2) subsampling using a precision wet splitter.

A small fraction (100-200 μl) was filtered on 0.4 μm Nuclepore filters for Scanning Electron Microscope (SEM) observation.

Subsamples for total mass flux (TMF) determinations were filtered through 0.45 μm Millipore filters, rinsed with distilled water and dried at 60 °C for 24 h, then weighed. For total and organic carbon (C_{tot} and C_{org}) and total nitrogen (N_{tot}) content, samples were filtered through precombusted 25 mm GF/F glass fibre filters, then they were analysed by a Perkin-Elmer 2400 CHN Elemental Analyser. For C_{org} analysis, the inorganic carbon was removed by HCl vapours [19]. The total amount of organic matter is assumed as $2 \times C_{\text{org}}$.

Carbonate content was calculated assuming that all inorganic carbon (obtained from $C_{\text{tot}} - C_{\text{org}}$) was represented by CaCO_3 , using the carbonates/carbonate carbon ratio of 8.33. Biogenic silica (Si_{bio}) was determined by a dissolution with 2 M Na_2CO_3 solution at 85 C for 5 h [20, 21]. The lithogenic fraction was computed as the difference between the total mass and the sum of the biogenic components: organic matter + CaCO_3 + Si_{bio} .

Grain size spectrum of particles, in the range 0.8-128 μm , was determined with a Coulter Counter MULTISIZER 3, utilising the two-tube methodology.

Till now, the complete set of analysis is available only for the first deployment period (August-December 1999), while TMF data are available for both periods.

The Total Mass Flux (TMF) measured is reported in fig. 5.2. The particle flux shows rather constant low values (average 20 $\text{mg m}^{-2} \text{d}^{-1}$) from August 1999 to February 2000, while an increase during the March-June period was observed (average 156 $\text{mg m}^{-2} \text{d}^{-1}$).

For comparison in fig. 5.2 similar data, collected by Istituto di Biologia del Mare of CNR (Venice), in the Ionian Sea (station I1, at ~ 2300 m depth and about 200 km North of Capo Passero) in 1997 and 1998, are also shown [22]. These data show the same seasonal behaviour as in KM4 station and they confirm the extremely low sedimentation values in the Ionian plateau. However, although the annual cycle observed in the I1 station seems to be reproduced in Capo Passero, the data of the I1 station show marked variations from year to year, suggesting that the monitoring of the sedimentation rate should be carried out for long periods. The mass flux averaged over

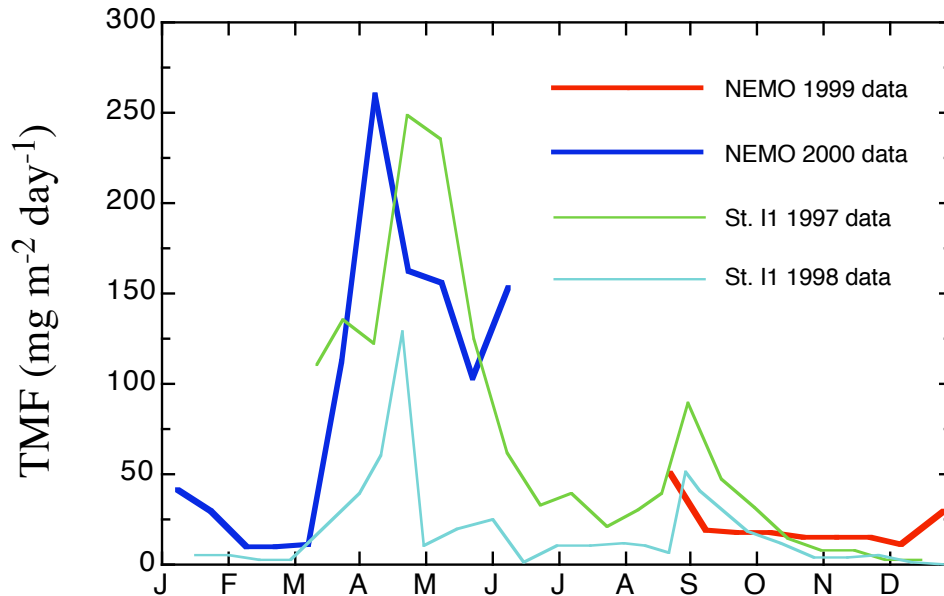


Figure 5.2 - Annual cycle of vertical fluxes in the Capo Passero site (thick blue and red lines). Data of the Northern Ionian II station are also shown.

the year of observation is $62 \text{ mg m}^{-2} \text{ d}^{-1}$. Data of the July 2001 – August 2002 period are under analysis, while the collection of samples is still going on.

From optical observation (optical microscopy and SEM), the trapped material during the first low-flux period is essentially constituted by diffused particles of small dimensions with rare small aggregates. The biogenic component is essentially represented by faecal pellets and remains of planktonic organisms (Radiolarian, Foraminifera, Pteropods). During the period of higher flux (spring 2000) the presence of flocks of various dimension and mucous aggregates with several faecal pellets, phytoplankton cells (mainly diatoms), and again remain of planktonic organisms was observed.

In the Ionian Sea, vertical fluxes of particles are considered highly correlated with the biological productivity, and show the same seasonality as confirmed by the direct relationship between carbon flux and primary production [22]. The autumn and spring peaks of fluxes are associated with phytoplankton blooms and match with the beginning and the end of the cooling period, in relation with the increase of inorganic nutrient concentration in the photic zone during the thermal mixing. Microplankton even in low abundance in the water column (in Ionian Sea diatoms are 3-10 % in number), might play an important role in assimilating exportable biomass in oligotrophic oceanic habitats with gelatinous aggregate formation. Particle settling velocity (about 150 m d^{-1}) permits a strict link between upper and deep-sea layers [22].

In summer the prevalence of organic nutrients in the photic layer [23], enhances regenerated production processes. In this layer the pico and nano-plankton fractions are predominant in the autotrophic communities, as reported also in [24], but the role of these organisms as source of sinking material is relatively unimportant [25].

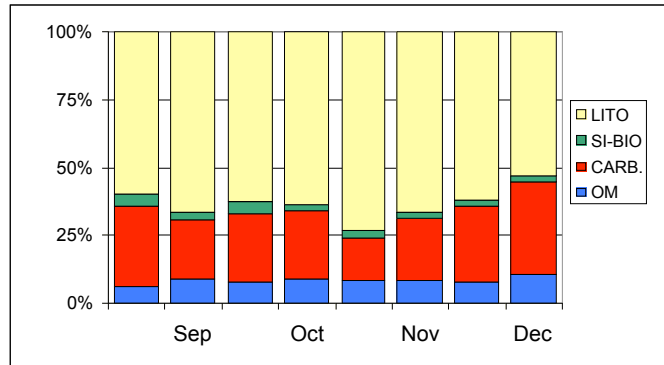


Figure 5.3 - Composition of the material collected during the first sampling period (August-December 1999).

The chemical analysis of the material collected by the trap has been carried out for the samples collected during the first deployment period (August-December 99). The composition of the sedimented material is shown in fig. 5.3, while the average values over the first collecting period are reported in Table. 5.1. The main component is represented by the lithogenic fraction and the high percentage of carbonates reflects the importance of coccolithophorids and foraminifera in plankton communities.

Table 5.1 – Chemical composition of sedimented material.

August– December 1999	Flux	
	<i>(mg m⁻² d⁻¹)</i>	<i>% of TMF</i>
Organic Matter	1.5 ± 0.6	8.2
Carbonates	5.2 ± 3.9	25.4
Biogenic silica	0.7 ± 0.7	3.1
Lithogenic	12.4 ± 7.3	63.3

The dimensional analysis of particles determined for the first sampling period (August 1999 - December 1999), in the range 0.8-128 μm, showed a general peak in the grain size distribution (expressed as volume percentage) around 3.5-6.5 μm, with a secondary mode in some samples around 30-68 μm (fig. 5.3).

- **Sediment fluxes in NESTOR site**

Two sediment trap lines were deployed in the area of NESTOR named KMS (fig. 5.4) and KMD (fig. 5.5) with one and five sets of trap/current meter respectively. In addition one Light Intensity Measuring System (LIMS) per line was also set. Dates, mooring positions, bottom depths of the mooring lines and the nominal depths of the instruments deployed in both sites are given in Table 5.2. The traps were synchronized to collect settling particles over 1 or 2-week periods. The experiment consisted of two individual

deployments covering the period from June 3rd to October 7th (the trap KMS-A collected samples from February 18th – October 7th).

The preparation of the sediment traps, the laboratory processing of the samples, including preliminary treatment, «swimmers» removal and sub-sampling was given in [viii]. Opal (biogenic silica) was determined with extraction of silica into 2M Na₂CO₃ solution at 85oC for 5h [xi]. Organic matter and carbonates data are not yet available. The shallower trap E of KMS line collected none samples, due to malfunction of the electronic device.

The temporal variability of total mass flux is shown in fig. 5.6.

The time-weighted means of total mass flux of KMS line for the period June 3rd to October 7th 2006, were:

- 13.22 mg m⁻² d⁻¹ for trap D
- 32.02 mg m⁻² d⁻¹ for trap C
- 33.09 mg m⁻² d⁻¹ for trap B
- 29.31 mg m⁻² d⁻¹ for trap A

showing relatively similar values from 2100m down to the 4273m depths, while at 1310m depths the mass flux was lower. The mean of mass flux for the period February 18th – October 7th 2006 of KMS-A trap was 35.51 mg m⁻² d⁻¹, due to high mass fluxes recorded from April to June. The time-weighted mean of total mass flux of KMD-A trap for the period June 3rd – October 7th 2006 was 22.89 mg m⁻² d⁻¹ lightly smaller than the KMS-A (29.31 mg m⁻² d⁻¹) (Table 5.3).

Table 5.2 - Dates, mooring positions, bottom depths of the mooring lines and the nominal depths of the instruments deployed in NESTOR area.

SITE	LONG	LAT	DEPTH (m)	LIMS	CURRENT METER	TRAPS	PERIOD
			815			E	3/6-7/10/2006
			818		X		3/6-7/10/2006
			1310			D	3/6-7/10/2006
			1313		X		3/6-7/10/2006
			2100			C	3/6-7/10/2006
			2103		X		3/6-7/10/2006
			3200			B	3/6-7/10/2006
			3203		X		3/6-7/10/2006
			4140	X			3/6-7/10/2006
			4270			A	18/2-7/10/2006
			4273		X		18/2-7/10/2006
KMS	21° 28.925	36° 32.955	4490				
			1430		X		3/6-7/10/2006
			2975		X		3/6-7/10/2006
			3990		X		3/6-7/10/2006
			4380	X			3/6-7/10/2006
			4690			A	3/6-7/10/2006
			4693		X		3/6-7/10/2006
KMD	21° 07.965	36° 33.180	5112				

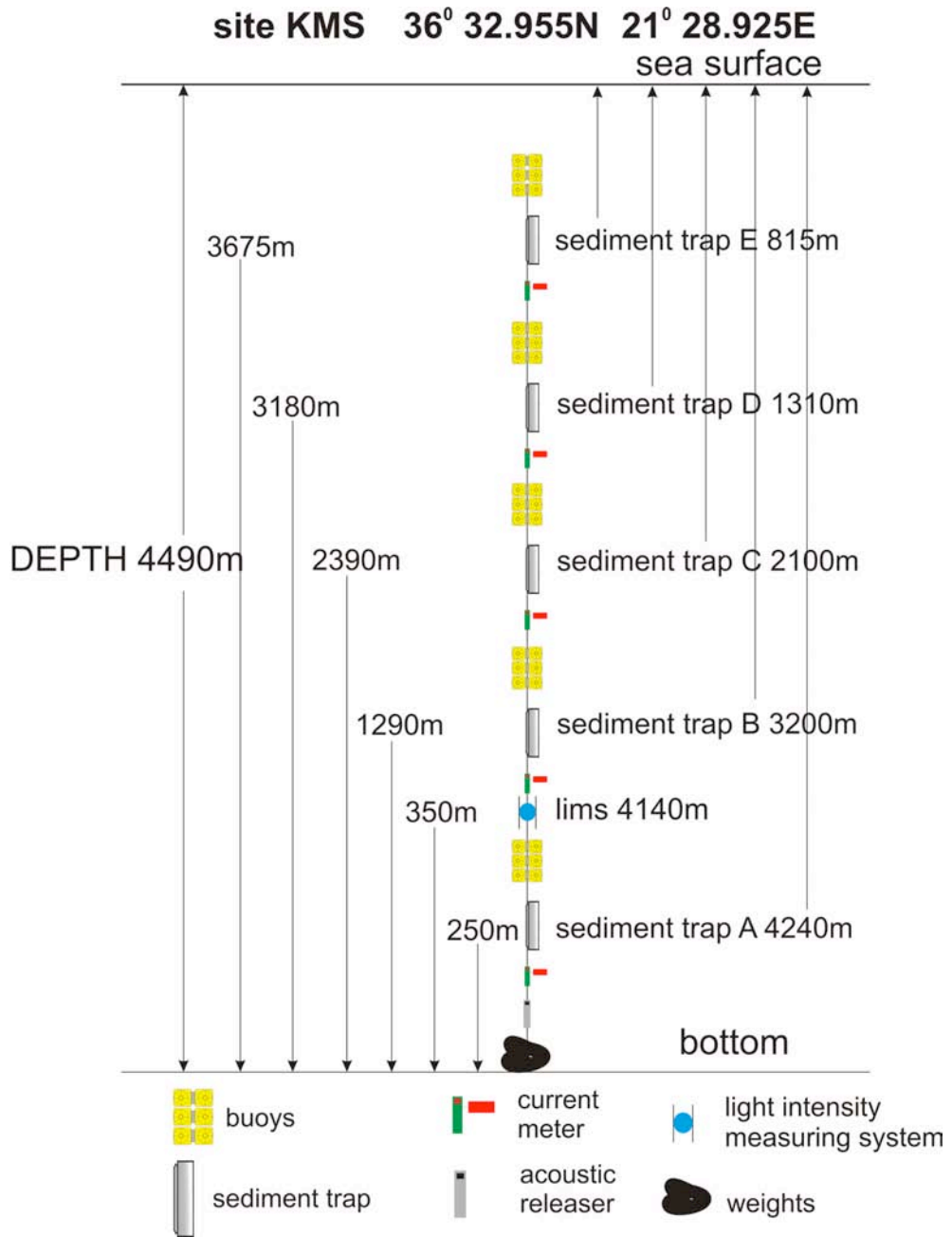


Figure 5.4 - Mooring line KMS design

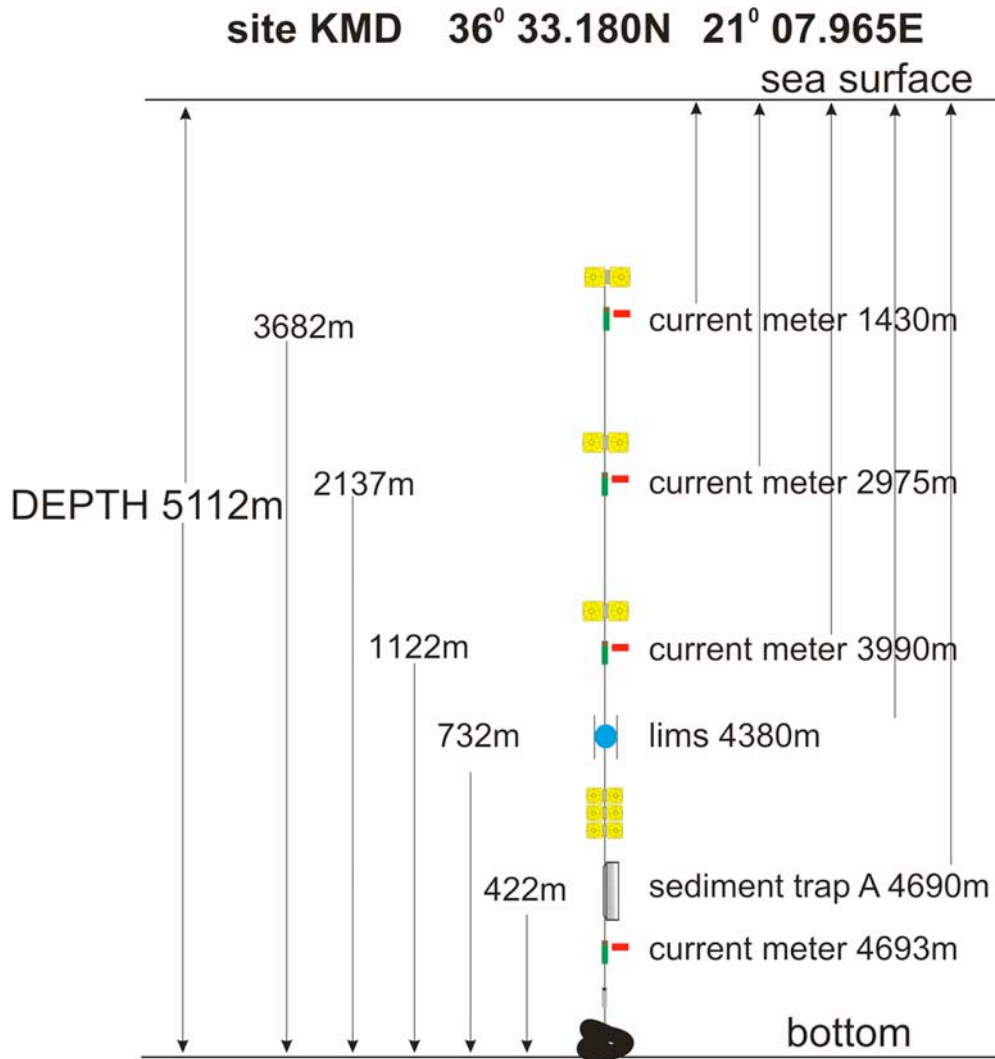


Figure 5.5 - Mooring line KMD design

Table 5.3 – Time-weighted means of total mass flux for the deployment periods at NESTOR trap sites

SITE	TRAP	DEPTH (m)	PERIOD	TMF (mg m ⁻² d ⁻¹)
KMS				
	D	1310	3/6 – 7/10/2006	13.22
	C	2100	3/6 – 7/10/2006	32.02
	B	3200	3/6 – 7/10/2006	33.09
	A	4270	3/6 – 7/10/2006	29.31
	A	4270	18/2 – 7/10/2006	35.51
KMD				
	A	4690	3/6 – 7/10/2006	22.89

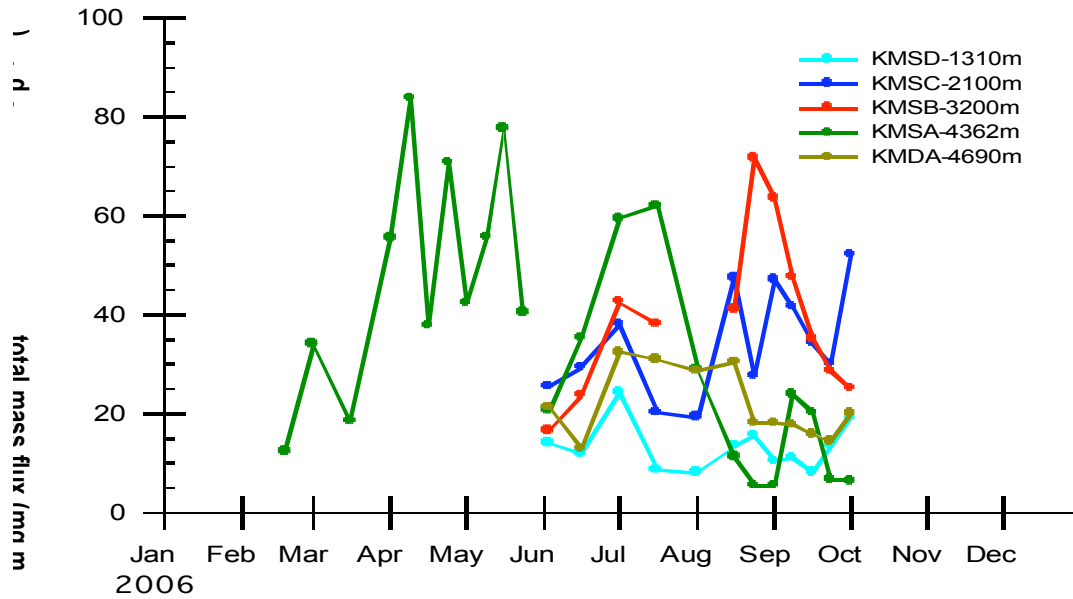


Figure 5.6 – Temporal evolution of total mass flux of settling particles at the two mooring lines.

The chemical analyses of settling particles are still in process and measurement of organic, inorganic carbon and lithogenic components will be completed in two months. Percentages and fluxes of biogenic silica are given in Table 5.4. Opal content of the line KMS was more or less constant with depth, as it ranged between 7.90 and 8.97%. At the KMDA trap the opal percentage was slightly higher with 9.64%.

Table 5.4 – Time-weighted means of opal contents and fluxes for the deployment periods at NESTOR trap sites

SITE	TRAP	DEPTH (m)	PERIOD	Si _{bio} %	Si _{bio} (mg m ⁻² d ⁻¹)
KMS	D	1310	3/6 – 7/10/2006	8.24	1.17
	C	2100	3/6 – 7/10/2006	8.97	2.99
	B	3200	3/6 – 7/10/2006	8.30	3.21
	A	4270	3/6 – 7/10/2006	7.90	2.36
	A	4270	18/2 – 7/10/2006	8.95	3.26
KMD	A	4690	3/6 – 7/10/2006	9.64	2.25

The two trap lines were deployed again for the period November 1st 2006 to April 31st 2007 and it is planned to continue the sampling until November of 2007.

6. Geological survey of the selected Mediterranean areas

- Geological survey of ANTARES site

The Nautilie submarine, in the period from December 21 to December 24 1998, collected six sediment core samples from the sea floor at the ANTARES site [13]. To collect each core, a 10-cm diameter 40-cm long PVC pipe was thrust into the sea floor using the manipulator of the Nautilie. Four sediment cores have been analyzed, giving similar results.

The sediment core shows four distinct sections, as illustrated in figure 6.1. The first and longest section (upper 0-16 cm) is mainly formed by clay sediment and biological material (pteropods). The second section (16-21 cm) is dominated by coarse sediments, with a smaller fraction of biogenic particles, slowly decreasing from the top to the bottom of the section. This second layer was formed over three centuries ago, according to sedimentation rates studied elsewhere. The last two sections of the core consist of a thin dark layer on top of a substrate formed of grey and brown mud with pteropods. These two layers are over three centuries old.

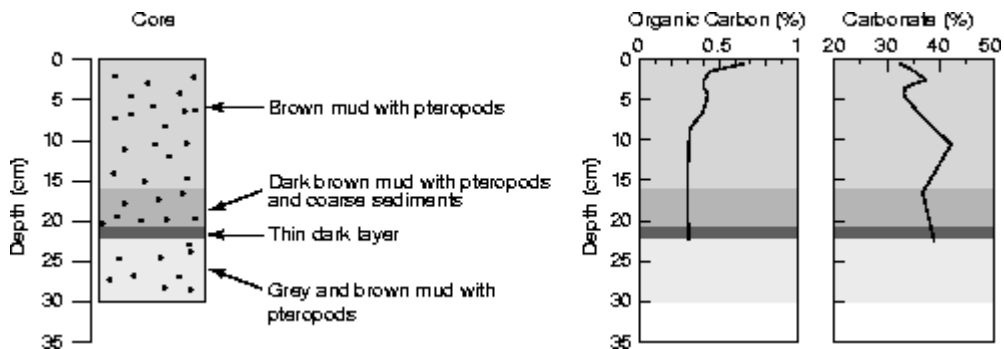


Figure 6.1 - Description of a core collected at the ANTARES site with the content profiles of organic carbon and carbonates. The various shades of grey illustrate the various compositions and textures.

The sedimentation rate is determined from the decay profile of ^{210}Pb activity of the core, using high-resolution alpha spectrometry. With 1998 data, we found an average sediment rate $R = 0.052 \text{ cm.yr}^{-1}$, which is 8 times higher than the average total mass flux determined by the sediment trap. An additional core, collected in July 2000 in similar conditions, gave an average sedimentation rate at the order of $R = 0.022 \text{ cm.yr}^{-1}$, so two times smaller. These differences can partly be explained by a variability of the local sedimentation, depending on the site morphology and on the continental slope. Anyway, these differences remain small on a scale of a century and results are consistent with previous works carried out in the NW Mediterranean basin.

These results highlight smallness of actual sediment amounts in deep sea, and show relative homogeneity of sediments.

- **Geological survey of NEMO site**

A preliminary geomorphologic characterization of the Capo Passero region has been performed with a study of an area of about $11 \times 5 \text{ km}^2$ around KM4. This study, performed by means of the Sub Bottom Profiler installed onboard the RV Urania, has evidenced that the sea bottom has a rather flat topography with slopes that, with few exceptions, do not exceed 0.5° . The bathymetry remains also flat for hundreds of km^2 around the region. The nature of the sea bottom is that of deposit of sediments of pelagic or emipelagic environment of sedimentation, characterized by absent or very weak bottom currents, that has permitted the formation of basin deposits (pelagic carbonates).

Eight sediment cores have been sampled in various locations close to KM4. The average length of the cores (fig. 6.2) was about 5 m.

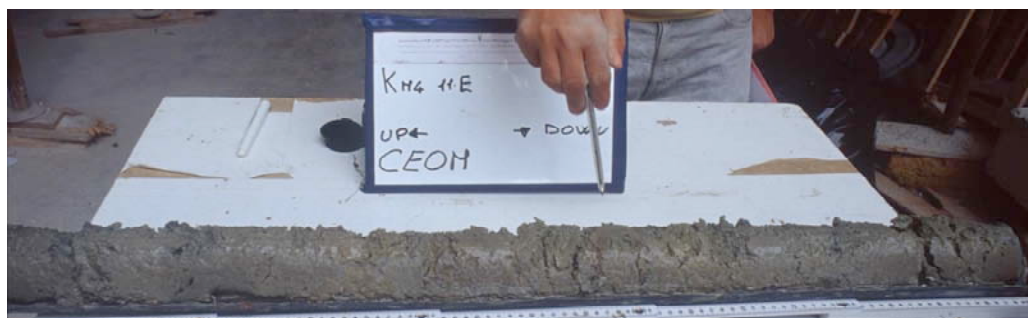


Figure 6.2 - One of the KM4 cores.

All of the cores have been analysed, showing the same stratigraphic features. Along their whole length the cores are essentially composed by clay sediments. Only two layers, one located at about 3 m below the sea-bottom and the second one at about 4.5 m, with different composition (silty sand) have been found. Layers of volcanic ash (tephra), that can be associated to ancient (more than 70 kyr) pyroclastic events, are also present.

Some feature observed in the cores, that can be associated to well known geological events, allow for a dating of the different layers of the cores. In particular, levels with a high concentration of organic material have been evidenced. These levels can be associated with anoxic events known as Sapropel, caused by the presence of a highly layered structure of the water column with a strong reduction of the oxygen exchange in the deepest waters. The presence of a strongly reducing environment favoured the preservation of organic substance on the sea-bottom. The most recent event, known as Sapropel S1, has been found in the cores at a depth of about 80 cm and can be dated between 9 and 6.5 kyr before present (BP).

A qualitative analysis of the Nannoflores, and in particular the relative abundance of *Emiliana Huxley* and *Gephyrocapsa Muellerae*, allows to associate the bottom part of the cores (below 3 m depth) to the Tyrrhenian (Mediterranean Isotopic Stage 5), dated between 125 and 75 kyr BP. At about 3 m depth the increase in the presence of *Emiliana Huxley* has been evidenced. This event is chronologically calibrated at about 60-70 kyr BP.

The association with planktonic foraminifera and nannoplankton allows evidencing the isotopic stages 2 and 1. The isotopic stage 2 is recognizable from the high ratio $^{18}\text{O}/^{16}\text{O}$ and corresponds to the Last Glacial Maximum, occurred between 24 and 14 kyr BP. The isotopic stage 1, which is characterized by a lower value of the $^{18}\text{O}/^{16}\text{O}$ ratio, corresponds with a warmer interglacial period dated between 13 and 14 kyr BP.

Based on these data an evaluation of the sediment accumulation rate has been performed, giving a value of 3-4 cm/kyr. This result is in agreement with the mass flux measured with the sediment trap. The only evidence of turbidity events, which occur when sediments of the continental shelf slide down the continental slope, has been found in the previous mentioned dark layer at a depth of 2.5 m. This leads to a date of about 65 kyr BP.

- **Geological survey of NESTOR site**

The greater area of the NESTOR site is located in the SE Ionian Sea (fig. 6.3). The submarine morphology is complicated with steep slopes close to the Messinia/Pylos

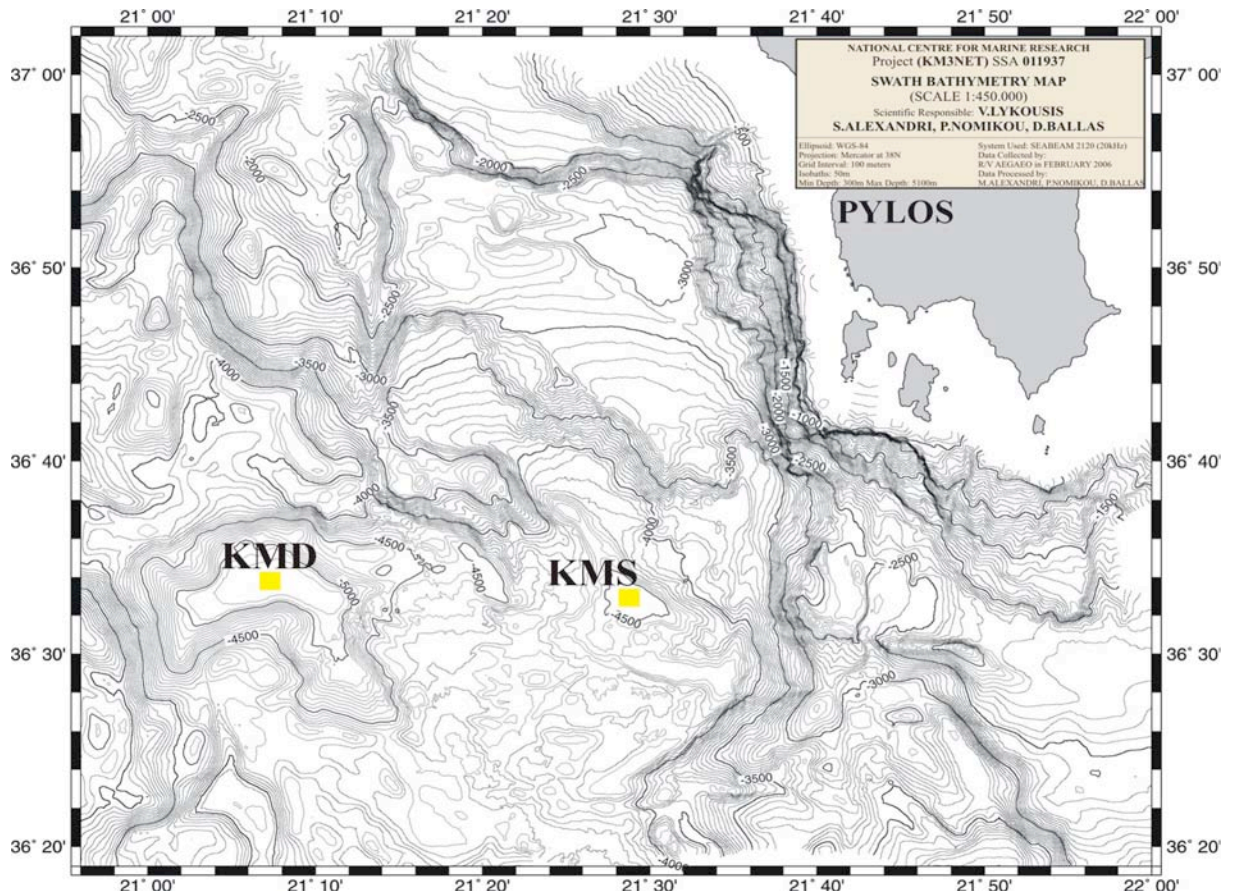


Figure 6.3 - Multibeam bathymetric map of the NESTOR greater area (SE Ionian)

(SW Peloponnese), valleys and deep basins. The abrupt slope extends in short distances from the shore from the 600-3000m depths. Deeper from 3000m and up to 4000m depth the area is covered with valleys and morphological plateaus. The most important feature of the region is that incorporates the deepest basins of the Mediterranean Sea (4600 and 5160m depths). These sites (basins) were selected for further research as potential KM3 locations (KMS-KMD).

Detailed continuous sub-bottom seismic profiling revealed the bottom sediment stratification that is very thin due to the insignificant sediment input from the nearby continent. The steep slopes are almost free of sediments (acoustic basement) and the valleys and plateaus covered by undisturbed sediments (lack of slumps or massive sediment failures). The sub-bottom strata of the deep basins consist from continuous weak and parallel reflectors indicating purely pelagic sedimentation with the absence of turbidity flows.

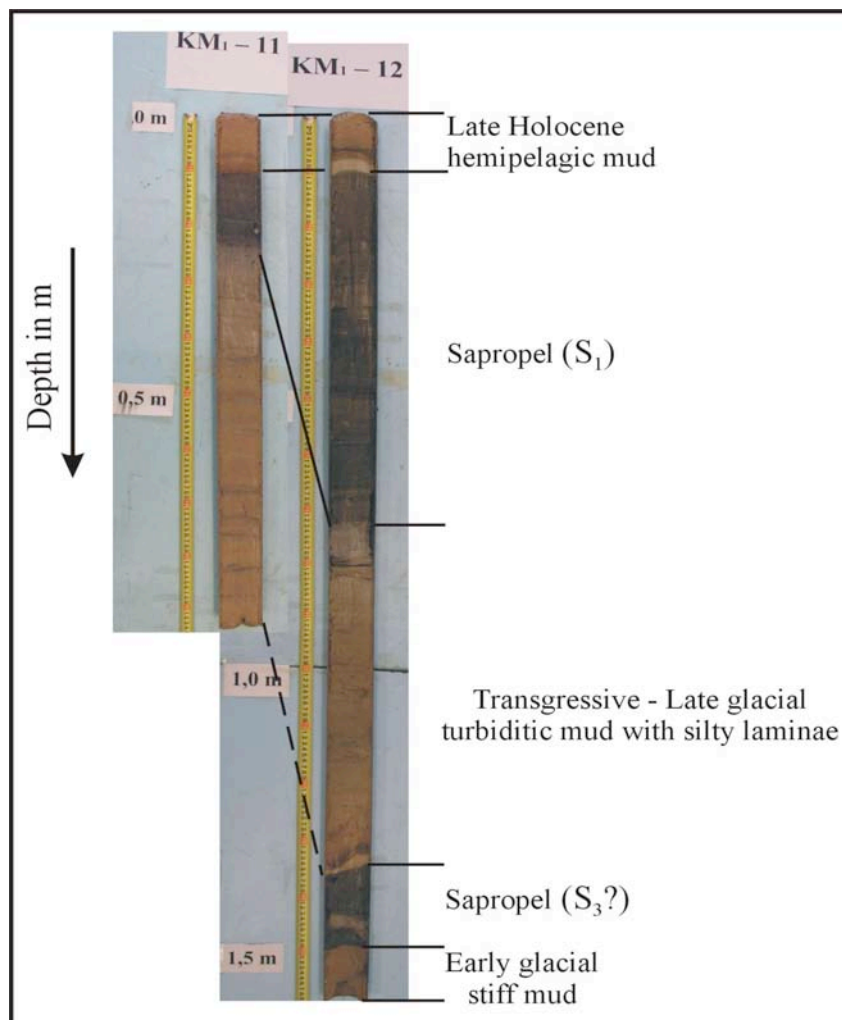


Figure 6.4 - Photograph and description of representative cores KM1-11 and KM1-12.

Eight sediment cores were collected offshore Pylos close to the location of KM3, Nestor site. The cores were taken with R/V Aegaeo during three cruises in the period 2006-2007. The cores were recovered from deep basin/slopes at water depths between 3300 and 4200m and core lengths between 0.94 and 4.0 m.

In the HCMR Laboratories the cores were split, X-rayed using a Faxitron X-Ray cabinet, photographed and macroscopically described. Sediment compressional wave (PW) velocity, dry gamma density, magnetic susceptibility, impedance and fractional porosity were measured using a Geotek multisensor core logger (MSCL) prior to opening gravity cores for further processing. The MSCL is a computer control, automated data acquisition system, consisting of a conveyor that moves intact whole core sections past a series of stationary sensors. Measurements of mentioned geoaoustic properties (MSCL) were made at 1-cm intervals along the length of each intact whole core section.

Five differential units of mud / clayey silt were identified in the representative cores KM1-11, KM1-12, on the basis of visual inspection and X-ray radiographs consists generally of mud (fig. 6.4). The top unit extends from the surface of the core down to 10-11 cm, and consists of water reach homogenous mud.

The lower unit consists mainly of dark coloured water reach mud with high concentration of organic material is a sapropel (S-1) sequence. Sapropel and sapropelic mud (it depends of organic carbon content) are characteristic of Holocene and interglacial Pleistocene sediments of eastern Mediterranean basins. The deposition of sapropel S-1 initiated about 9.2 kyrs BP (before present) during the Holocene and was completed at 6.4 kyrs BP.

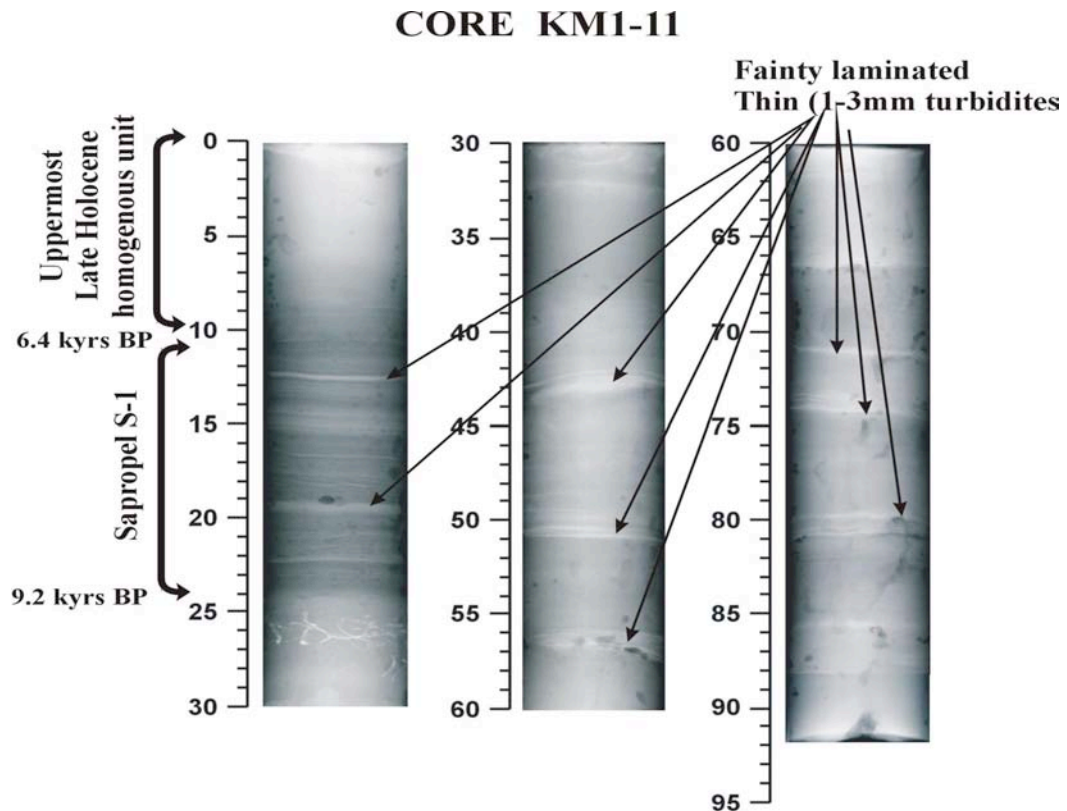


Figure 6.5 X-ray radiographs of three representative units of the core KM1-11.

The thickness of the sediment column of uppermost unit and the actual location of sapropel S-1 in the cores were used to calculate mean sediment accumulation rates within the uppermost unit. The mean sedimentation rate in the uppermost unit that

accumulated after the end of deposition of sapropel S-1 is 1.6-1.7 cm/kyrs. These very low values of sedimentation rates are agreement with the low lithogenic flux of particulate matter measured using sediment traps. These mean sedimentation rates are from lowest that have been determined in the Eastern Mediterranean.

The third unit that was identified below the sapropel S-1 generally consists of turbidity mud with silty laminae less water. This unit was deposited possibly during the last glacial/post-glacial period. Below this unit was identified a second sapropel sequence possible S-3 (30 kyrs BP) only in the core KM1-12. In the same core was identified a last sort unit below the sapropel S-3 consists of stiff mud and deposited during early glacial period.

Core KM1-12

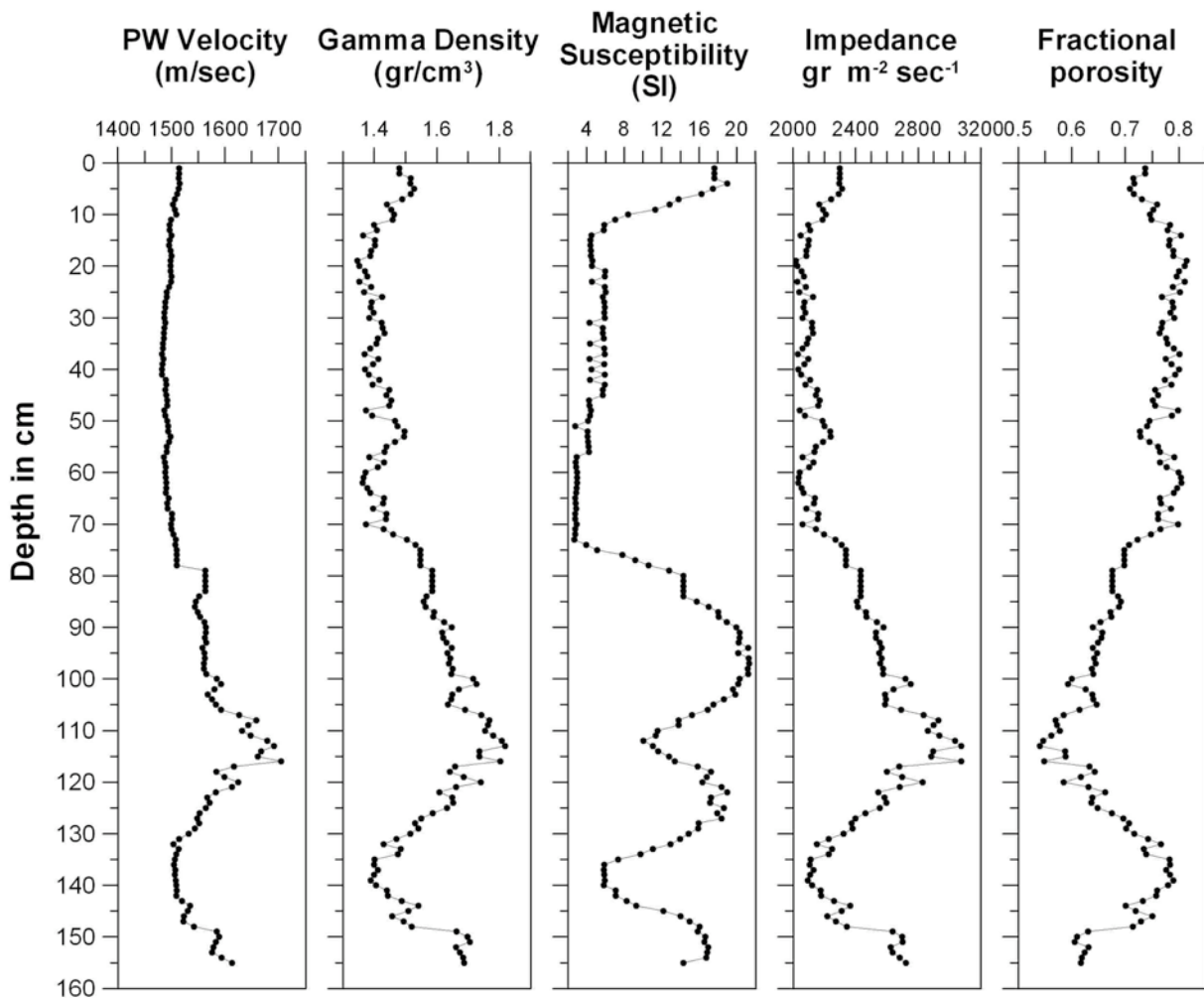


Figure 6.6 Vertical variation of geoaoustic properties along core KM1-12

X-ray images of the spit cores provided significant information regarding sediment processes at the coring sites (fig. 6.5). Detailed X-ray photographs and textural analysis of the uppermost sediment unit appears to be homogenous hemipelagic and indicate that the prevailing sediment processes during the most recent period of last Holocene (0-6,5 kyrs) in the area of KM-3 is the hemipelagic sedimentation. X-ray images of the

sapropel S-1 unit and the below units revealed a series of faint laminations 1-3 mm in thickness (fig 6.5). This displaying deposition from benthic nepheloid layers or from down slope small-scale turbidity flows. Such type sediments gravity flows are expected to be possible on the basin slopes during the last glacial stage and the following transgression at the lower sea level stand conditions.

MSCL results for geoacoustic properties of sediments (fig. 6.6) show that the PW Velocity ranged between 1482 to 1691m/sec with maximum values are occurred in the silt laminae of third unit (turbidity mud, core KM1-12). Gamma density varied from 1.35 to 1.80 gr/cm³ with lower values is located in the topmost unit and the sapropel sequences where the water content is very high. Magnetic susceptibility and impedance averaged between 2.61 and 23.33 SI and between 2017 and 3076 gr m⁻² sec⁻¹ respectively. Generally magnetic susceptibility and impedance decreased gradually in the sapropel sequences. Strong relationships is realised between fractional porosity, water content and grain size of sediments. The higher values of fractional porosity are located in the sapropel sequences and in the uppermost sediment unit (0.80) while the lower values (0.53) are presented in the silty laminae of turbidity mud (third unit).

7. Hydrobiological survey of the various selected areas

- **Hydrobiological survey of NEMO site**

To evaluate the possible interference on the detector efficiency, the area characterization has also been performed through an interdisciplinary analysis of the main physical, chemical, trophic and microbiological features of the water masses. Particular attention was put on the bacterial compartment that plays a dominant role in the organic matter transformation in the marine ecosystems. The seasonal evolution of trophic rate in the water masses was investigated in four oceanographic cruises (December 1999, September 2000, July 2001, April 2002).

The investigated area shows typical oligotrophic conditions and a marked water stratification, which influences the distribution of planktonic communities.

Four main water masses were identified: Atlantic Water (0-200m), Levantine Intermediate Waters, Eastern Mediterranean Deep Water and Cretan Deep Water. Seasonal variability of selected parameters was observed in each water mass and in the whole water column.

Different vertical patterns were found for each parameter, but the prevailing trend was characterized by a decrease in activity and abundance values with increasing depth. In the shallow water photic zones microbial processes are particularly intense and subject to strong seasonal variations, also in relation with photosynthetic activity. With increasing depth only low levels of biological activity and a marked decreasing vertical gradient were observed.

The trophic load was very moderate during all investigation cycle, and appreciable differences between photic and deep zone were observed, with the highest levels in the first one.

The highest levels of biomass were noticed at the superficial layer and generally decreased from the surface to the bottom. Also the higher microbial activity levels were registered in these layers suggesting the presence of an efficient microbial food chain in this oligotrophic environment and confirming the key role of enzymatic activity to mediate the organic matter flux in the whole water column.

Particularly relevant for what concerns the effects on the water Čerenkov detector is the absence in the deepest waters of luminescent bacteria, already presented in fig. 3.2.

The presence of Particulate Organic Carbon (POC) and Particulate Organic Nitrogen (PON) is very low in agreement with the known oligotrophic condition of the area. The lowest values have been observed during the summer campaign.

The measurements of biological parameters confirm the sedimentation and biofouling data, showing that deep Ionian Seawaters are comparable with oceanic waters. The extremely low values of the bacterial concentration could represent a double advantage

both for the expected growth of biofilm and for the optical noise level induced by bioluminescent organisms.

Considering the variability observed in the eastern Mediterranean during the last decade, new observation activity was planned starting from 2006. A west-east hydrographic transect, from the Malta plateau to the deep sea, has been repeated in two different periods (April and October). In both periods, corresponding to different seasons, we can observe a similar deep structure with an almost well defined vertical stratification. At the NEMO site, during the October 2006 cruise and below 2000m of depth (fig. 7.1), the potential temperature decreased with depth from 13.50 to 13.42 at 3000m, while salinity changed from 38.745 at 2000m to 38.73 at 3000m. The horizontal variability of temperature and salinity was few thousandths of °C and psu, respectively, over a distance of 50km.

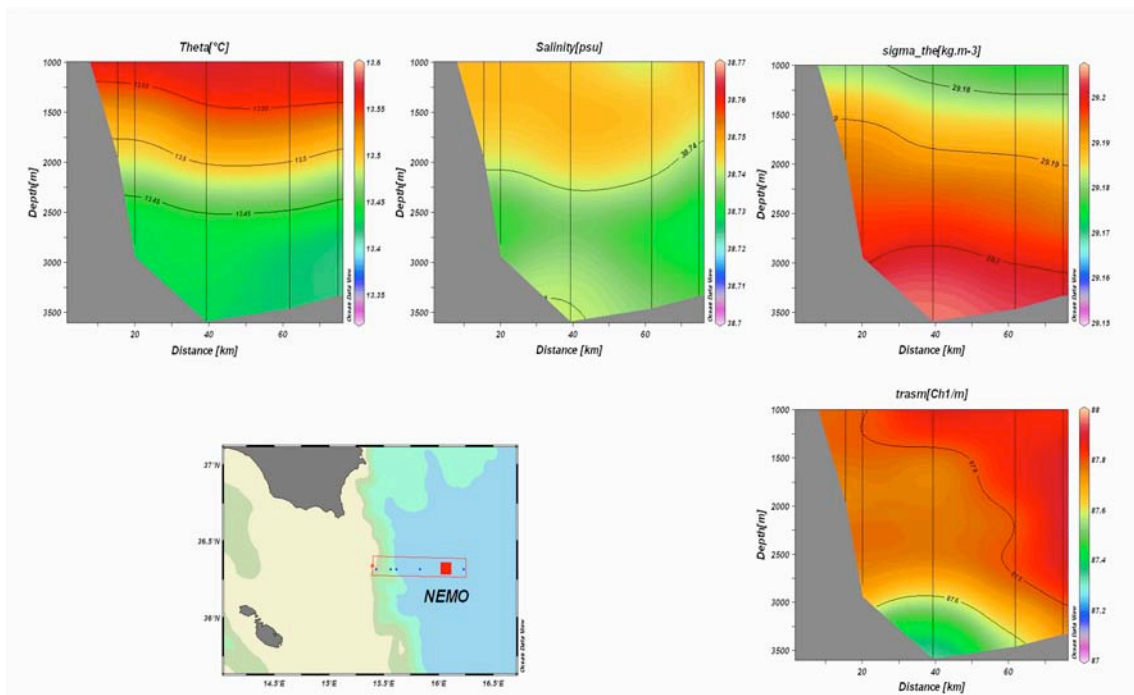


Figure 7.1 -Vertical sections of Temperature, Salinity, Density and Light Transmission, from 1000m to the bottom during October 2006. The 2nd profile from the right corresponds to the NEMO site.

Tramissometer¹ measurements below 1000m of depth give along the section almost homogeneous light transmission, with very stable values along the NEMO profile.

- **Water-mass structure and deep currents in the NESTOR area.**

The hydrologic characteristics and the current regime in the NESTOR area are determined by the dynamic structures that drive the upper and deep circulation in the eastern margin of the Ionian Sea. Fig.7.2 is a sketch of the dynamic structures that determine the upper circulation in the Eastern Mediterranean.

¹ Chelsea, ALPHA tracka MkII, wavelength 660nm, optical path length 25cm.

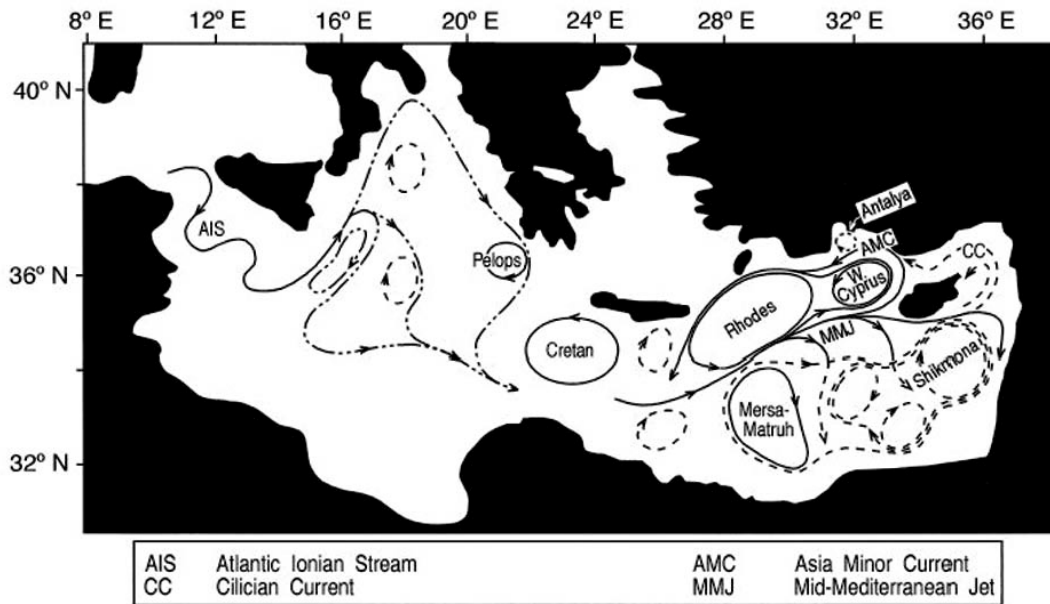


Figure 7.2. Sketch of surface circulation dynamic structures in the Eastern Mediterranean, taken from [26]

The upper circulation in the NESTOR area is influenced by the Pelops anticyclone, a dynamic structure with lateral scales on the order of 2° LAT x 2° LON that transports water along its periphery in a clockwise manner. The NESTOR area is most frequently located in the northeast edge of the Pelops anticyclone. The upper-layer(s) circulation in the NEMO area is influenced by the meandering of the Atlantic Ionian Stream., i.e., the jet that carries the low salinity signal of the Atlantic Water and propagates eastward in the Eastern Mediterranean.

Fig. 7.3 depicts the distribution of the near-bottom dissolved oxygen values in the Eastern Mediterranean and is indicative of the deep basin-wide thermohaline circulation. Deep oxygen maxima are observed in the southern Adriatic and along the eastern Italian slope, offshore from southern Italy and Sicily. The phenomenology behind this observation is as follows: During winter, surface water masses of high oxygen content sink to the bottom in the southern Adriatic Sea because of density increase resulting from intense cooling. Afterwards, they spread southwards and to greater depths along the Italian continental slope forming a bottom boundary current or bottom gravity/density plume. Apart from high oxygen content, bottom gravity plumes on their pathway are advecting characteristic properties, such as salinity, temperature and transparency, of the surface waters of the area where they are originating from. Furthermore, along their spreading route they grow in size due to entrainment of surrounding water and their path is temporally and spatially varying because of internal instabilities, friction with the sea bottom and varying characteristics they can have from year to year [27]. Figure 7.3 shows that the deep Adriatic plume is providing higher bottom oxygen values along the western margin of the east Mediterranean basin. After passing the southern tip of Sicily and reaching the deep plain of the Eastern Mediterranean with depths 3000-4000 m, the deep Adriatic waters spread to the east to

fill the rest of the East Mediterranean basin. The southern Adriatic has been termed as ‘the engine’ that drives the East Mediterranean deep thermohaline circulation.

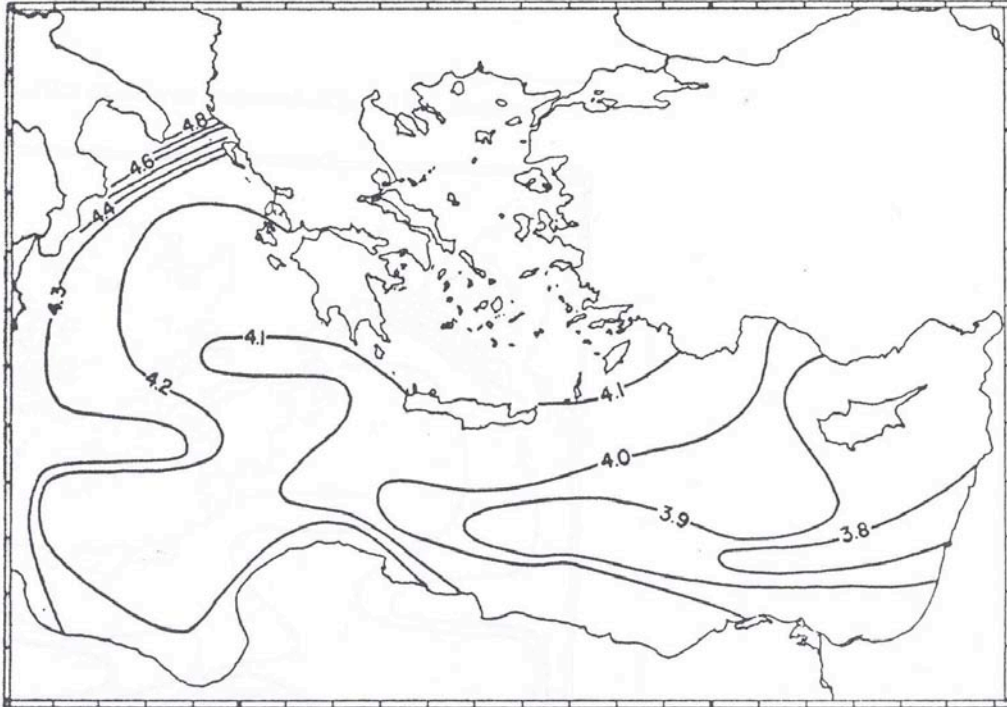


Figure 7.3 - Deep maxima of dissolved oxygen. (From [28])

This process was interrupted during the period of the late 80's-to-mid 90's, when the Aegean became the area filling the bottom layers of the East Mediterranean with dense waters, due to their high salinity content, which were outflowing from the sills to the east and west of Crete. By the late 90's the Cretan Water deep outflow into the Eastern Mediterranean was not dense enough to sink to the bottom and there has been a return to the previous state of the thermohaline circulation when the bottom water was of Adriatic origin [29].

- **Recent Hydrography in NESTOR area.**

In 2006, three cruises (February, June and October) were undertaken by the HCMR (Hellenic Centre for Marine Research) in the NESTOR area within the framework of KM3NET. Fig. 7.4 shows the (CTD: Conductivity Temperature Depth) stations for each cruise, in which typical hydrographic continuous profiles of temperature salinity and light transmission measurements were collected.

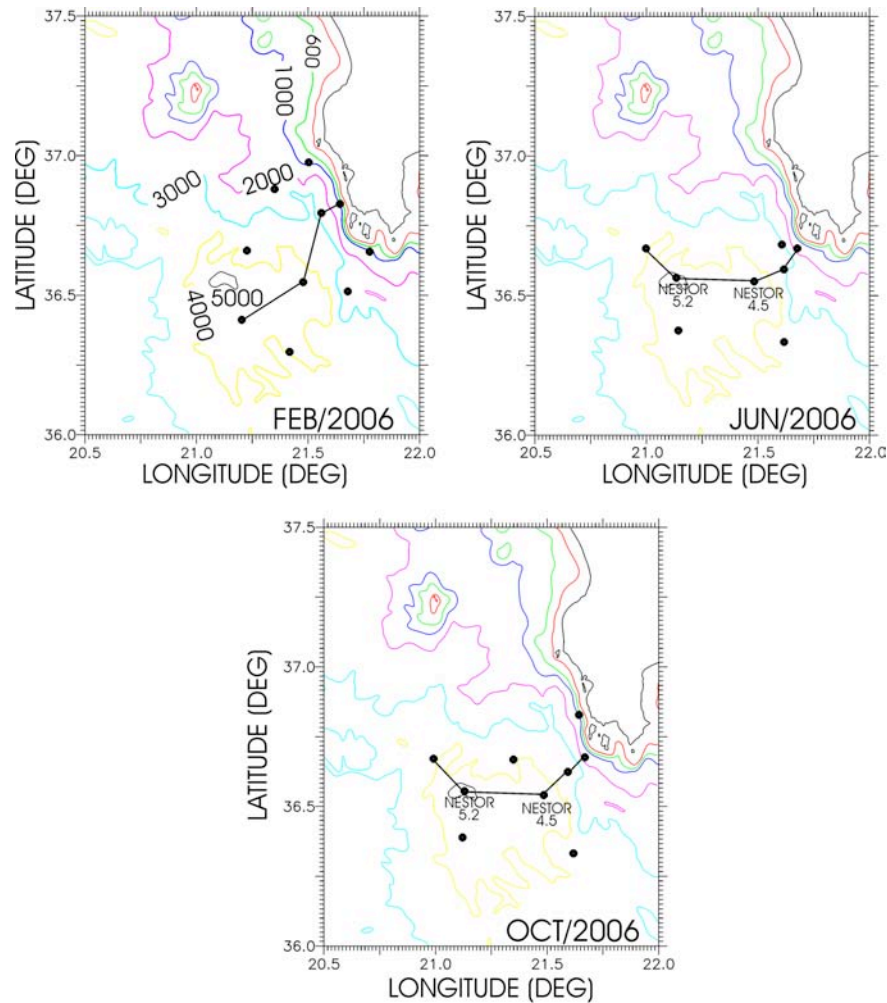


Figure 7.4 - Black dots are positions of CTD stations for the cruises of February/2006 (upper left panel), June/2006 (upper right panel) and October/2006 (lower panel) in the NESTOR area. Depths in meters of the depth contours are shown in the upper left panel. Black lines joining CTD stations represent hydrographic sections shown below. NESTOR_5.2 and NESTOR_4.5 are sites with bottom depths 5.2 and 4.5 km, respectively, where current meter/sediment trap moorings were deployed in 2006.

The light transmission measurements in this section refer to percent beam intensity detected at a distance of 25 cm from a point source of a red well-collimated beam relative to the beam intensity output of the point source. They are utilized only to map relative changes of water transparency throughout the NESTOR area so as to investigate structures in spatial distribution of water transparency and possibly identify water masses that can be associated with less or more transparent water.

Temperature, salinity and density profiles at sites NESTOR_5.2 and NESTOR_4.5 are shown in fig. 7.5, whereas fig. 7.6 shows an expanded view of the salinity profiles in NESTOR_5.2 and NESTOR_4.5 and is used for the description of the various water masses existing in the NESTOR area.

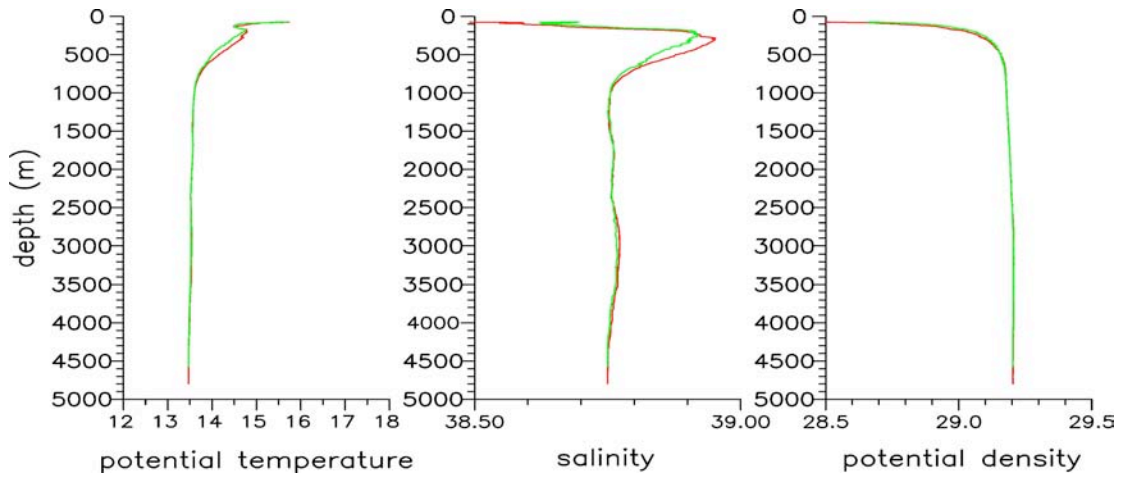


Figure 7.5 - Profiles of potential temperature, salinity and potential density obtained in 2006 at sites NESTOR_5.2 (36.556° N 21.131° E) (red lines) and NESTOR_4.5 (36.545° N 21.482° E) (green lines). (At site NESTOR_5.2 the CTD was not lowered to the sea bottom for safety reasons because of malfunctioning altimetric probe on the CTD and uncertainty to the ‘distance from the bottom’)

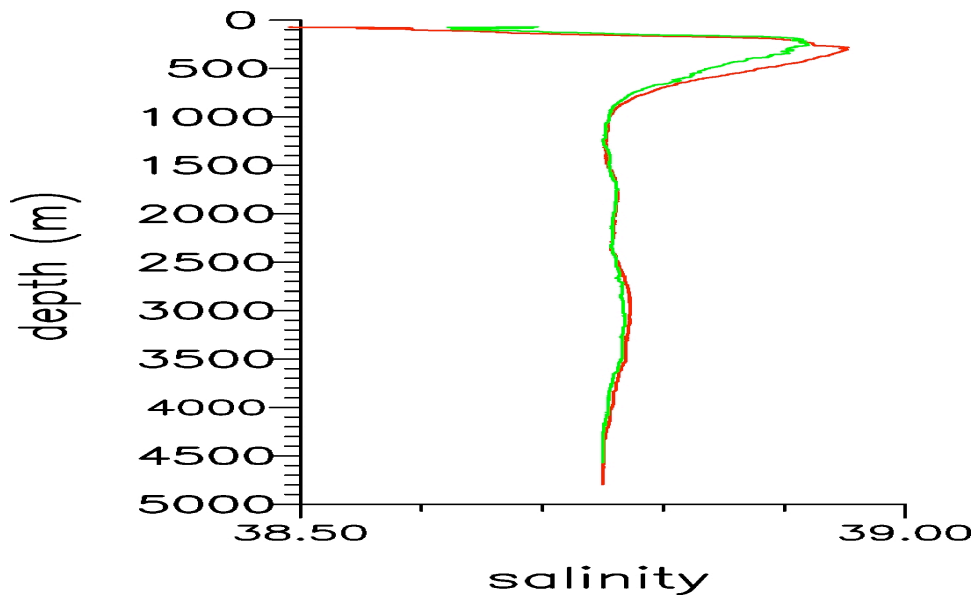


Figure 7.6 - Salinity profiles of Figure 7.5.

In fig. 7.7 we observe:

- 1) The Levantine Intermediate Water (LIW) indicated by the high salinity core at ~ 200 m.
- 2) The weak salinity maxima at ~1600 m and at ~3000, which are indicative of Intermediate Water masses of Cretan origin.
- 3) The distinct salinity change toward lower values for the water masses deeper than ~4000 m which is indicative of their Adriatic origin. This is the most recent (after the late 90’s) East Mediterranean Deep and Bottom Water (EMDW) of Adriatic origin.

Figures 7.7, 7.8 and 7.9 show the 2-D (horizontal-vertical) distributions of temperature, salinity and water transparency, expressed as % light transmission (see above), for the

three hydrographic cruises in 2006 on the sections shown in Figure 7.4. In the first cruise (February/2006, fig. 7.7) the CTD profiles could not exceed the depth of 3.5 km. In the second cruise (June/2006, fig. 7.8) a longer CTD wire was used but the light transmission-meter was malfunctioning and provided wrong measurements. In the third cruise (October/2006, fig. 7.9) another light transmission-meter was used, detecting the percent light transmission of red light at 10 cm from the point source. Therefore in the third cruise we had a complete data set for temperature salinity and transparency with values reaching very near the bottom (fig. 7.9).

With respect to the conditions in the deep part of the section which are of interest for the construction and operation of the deep neutrino telescope, we observe in the temperature and salinity sections of fig. 7.9 a core of a water mass at depths around 3-3.5 km with local maxima in temperature and salinity and weak maxima in light-transmission. These characteristics depict a vain (intermediate plume) of Cretan Intermediate Water that originates from the area of the sills of the west Cretan Straits and is deflected northward, i.e., to the right of its outflowing direction. In greater depths, below the Cretan Intermediate Water, the dominant water mass is the East Mediterranean Deep (and Bottom) Water (EMDW) of Adriatic origin that is characterized by lower temperature and salinity, as discussed with respect to fig. 7.7 and also addressed in the section ‘Historical Background’. The transparency section of fig. 7.9 shows that this water mass (EMDW of Adriatic origin), for the wavelength of the instrument, at the NESTOR area has slightly less transparency than the Cretan Intermediate Water.

Therefore, if we exclude local factors such as sedimentation, the water transparency of the recent East Mediterranean Deep Water of Adriatic origin that dominates in the near bottom layers of the Ionian Sea is expected to further decrease as we approach the Adriatic area of origin backwards along the spreading route that was discussed in the section ‘Historical Background’.

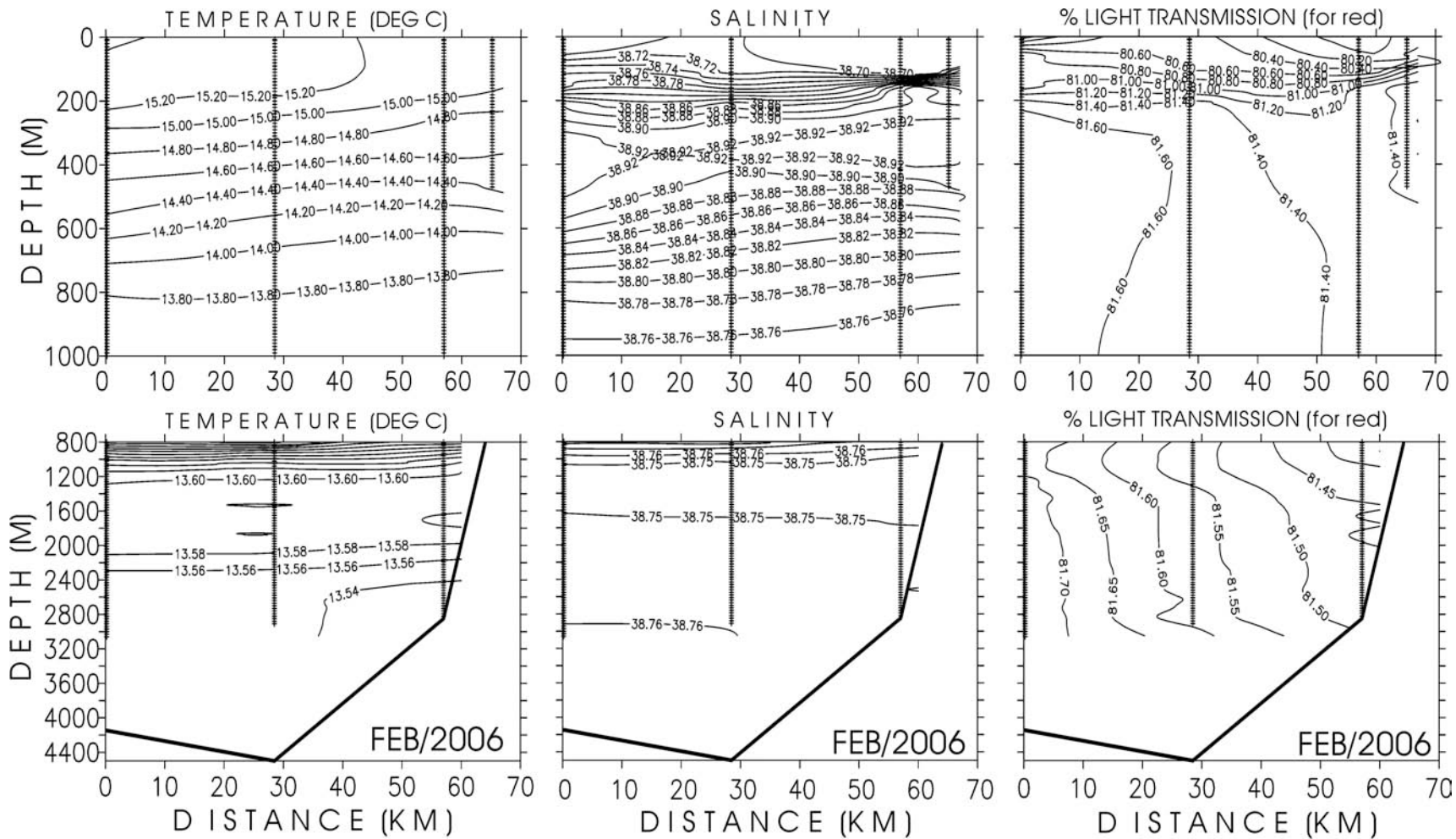


Figure 7.7 - Section of temperature, salinity and transparency in the NESTOR area in February/2006. Thick black line indicates sea bottom. Station location along the section and depth of measurements are indicated by crosses. The geographic position of the section is shown in Figure 3.

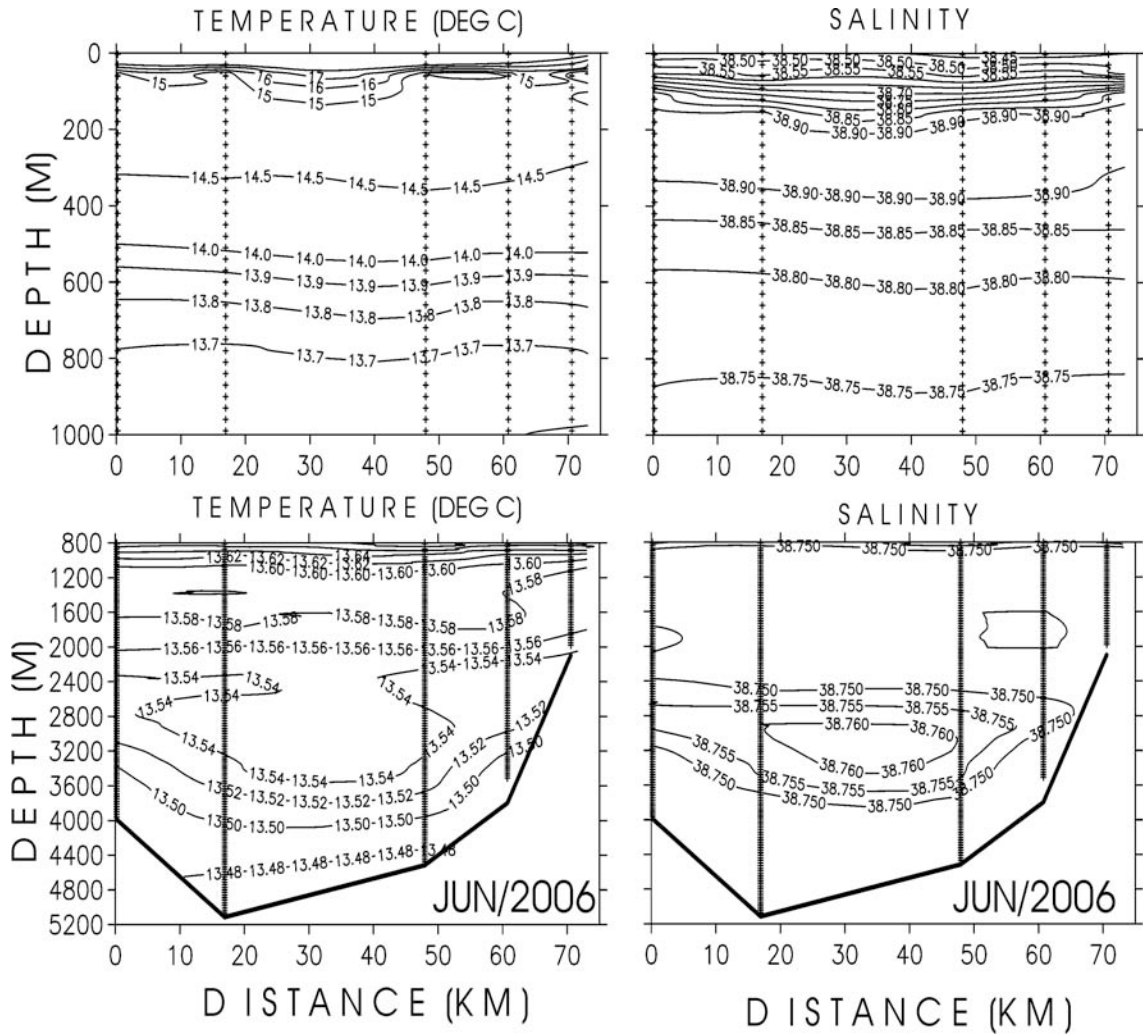


Figure 7.8: As in Figure 7.7, but for June/2006. Due to malfunctioning of the light transmission-meter, the transparency measurements are not available.

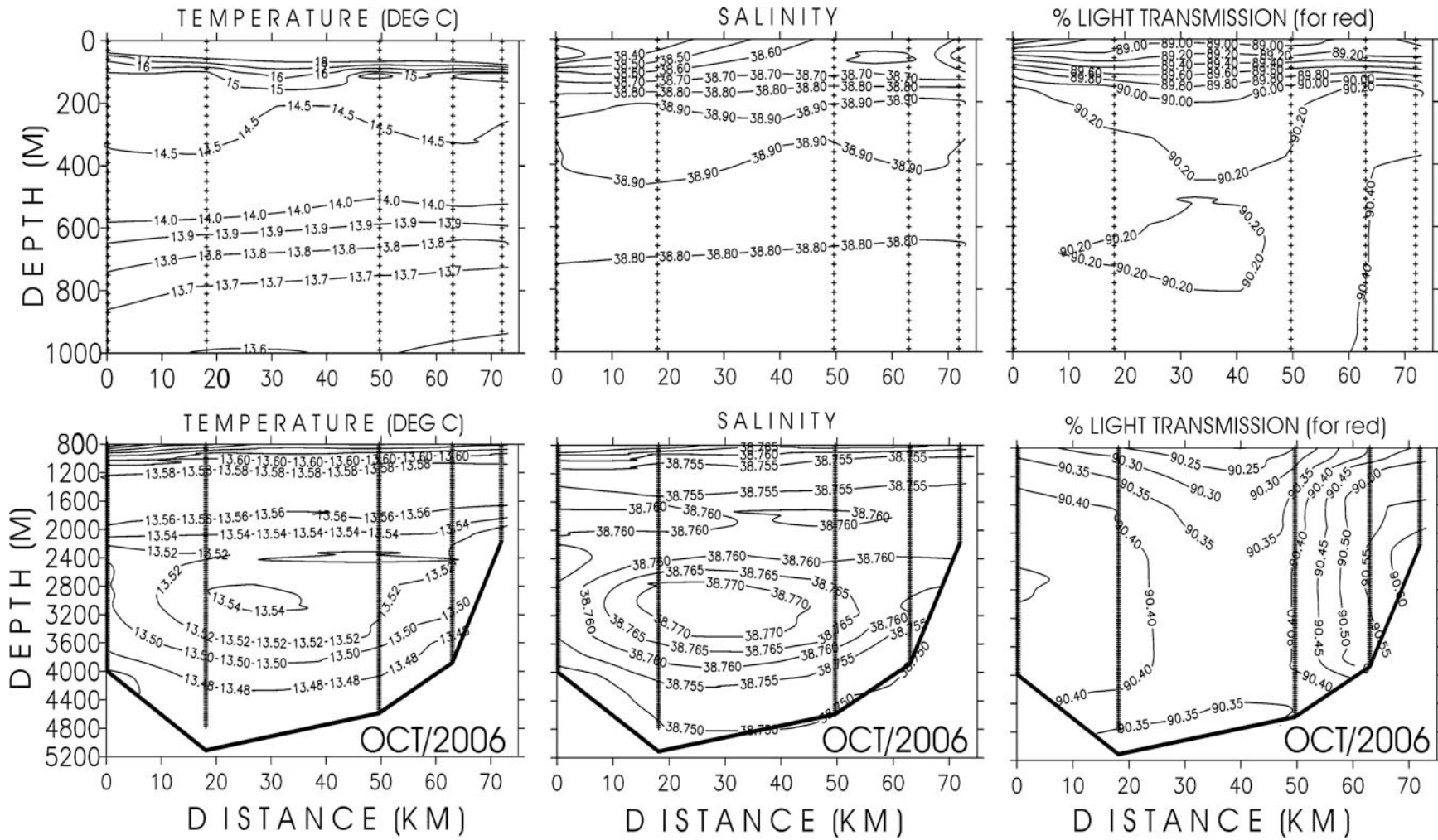


Figure 7.9 - As in Figure 7.7, but for October 2006.

8. Effects of biofouling on optical surfaces

Materials that are kept in a marine environment for long time are subject to the growth on their surfaces of a bacterial film or to the settling of marine organisms: this is called “bio-fouling”. The degradation of the light transmission properties of the glass spheres that are used to host the optical modules due to bio-fouling has to be studied since it determines the operational lifetime of the optical modules.

Deep-sea stations to study this phenomenon were deployed, or are planned to be deployed, in the various Mediterranean sites by the ANTARES, NEMO and NESTOR Collaborations. The measuring system is basically composed by an array of photodiodes placed inside a benthos glass sphere and illuminated by pulsed blue LEDs.

The measurement technique consists in studying the time evolution of the ratio between the pulse amplitude of each photodiode inside the sphere over the pulse amplitude of a reference photodiode placed inside the vessel containing the LED. If fouling is formed on the sphere surface, a reduction of the ratio is expected as a function of time.

- **Biofouling measurements in ANTARES site**

Optical fouling was studied in the vicinity of the ANTARES site with the immersion of a dedicated mooring line during three months in 1997 and eight months covering part of 1997 and of 1998 [13]. The setup for measuring light transmission is composed of two glass spheres, mounted on a support frame with their centres separated by 2.5 m. The first one holds a light source composed of two blue light emitting diodes (LED). The two-LED system is designed to ensure the stability of the light source. The second glass sphere contains five photodetectors glued to the inner surface of the sphere at various positions. The aim is to monitor the effect of fouling on the two glass surfaces by measuring the light flux transmitted to each photodiode.

The resulting relative transmissions are shown in Figures 8.1 and 8.2 as a function of time. These figures show a general trend of decreasing fouling with increasing zenith angle on the glass sphere. According to the figure 8.1, the transmission at the top of the sphere ($\theta=0^\circ$) decreases rapidly within a few days, but shows less variations at larger zenith angles. Moreover, the transmission is seen to recover from time to time in partial correlation with an increase in the measured water current velocity. These observations are consistent with the surfaces being fouled by sediments rather than microbial adhesion, sediments being more likely to stay on horizontal surfaces than on inclined ones, and can be washed off by flowing water. The differences between the three photodiodes at zenith angle 20° indicate patchiness in the fouling. Most important for neutrinos telescope is that there is less fouling at larger zenith angles, as confirmed by the figure 8.2. The measured loss in transmission at the equator of the sphere after eight months is 2.7%. Extrapolation for one year indicates a global loss of 4%, which, given that concerns the transmission of the combination of fouling on two surfaces at 90° , matches with a net loss at the equator of about 2% per year.

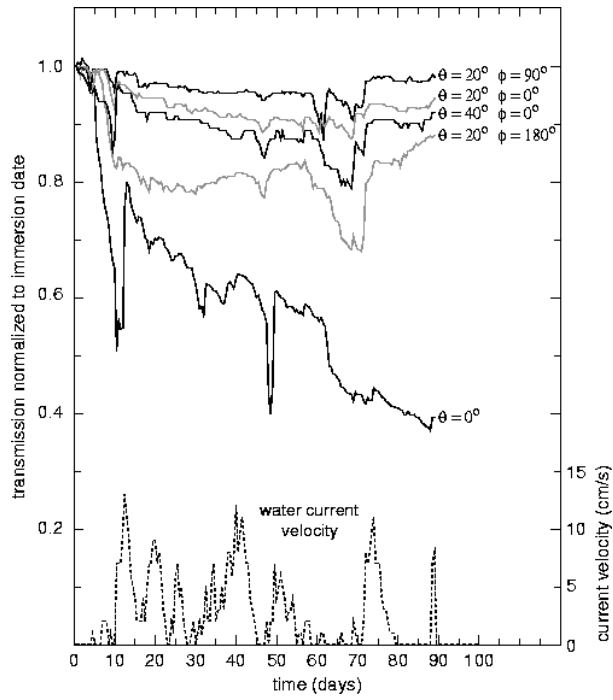


Figure 8.1 - Light transmission as function of time from the first immersion with two spheres mounted vertically. The zenith angle is θ and the azimuth angle is ϕ . The current velocity is indicated at the bottom of the figure.

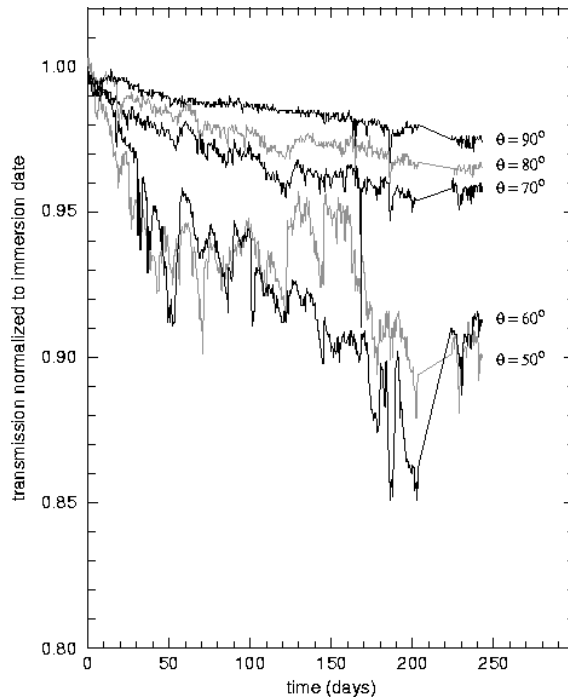


Figure 8.2 - Light transmission as function of time from the second immersion with two spheres mounted horizontally. The measurements for each of the five photodiodes are normalised to unity at immersion on July 12, 1997. Curves are labelled according to the photodiode zenith angle θ .

Biofilm collection system

The biofilm collection system consists of a 1.2 m long horizontal rod supporting 12 cylindrical sample holders. Six 2.6 x 3.8 cm² glass plates are mounted on each sample holder as shown in figure 8.3.

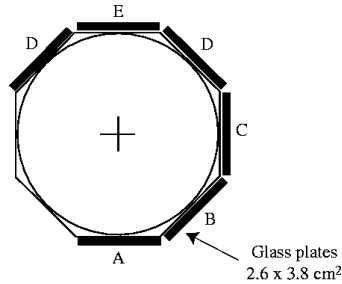


Figure 8.3 - Light Side view of a biofilm sample holder

After the immersion, at the recovery of the mooring line, all glass slides are immersed in either a glutaraldehyde or a formaldehyde solution, which fixes the biofilm. Using the epifluorescence microscopy, the density of bacteria after three-month or eight-month exposures at the ANTARES site ranges from 10⁴ to 10⁶ bact.cm⁻². Such low levels are similar to those observed on glass samples exposed for 1-2 weeks in shallow waters at temperature below 15°C.

- **Biofouling measurements in NEMO site**

The Capo Passero site, about 3300 meters deep, has very good optical properties so that it can be considered a good candidate as a site for the future "deep underwater high-energy neutrino telescope".

An under-water Čerenkov Neutrino Telescope is based on Čerenkov radiation's detection and is strongly dependent on light transmission properties in water (absorption and diffusion phenomena).

An evaluation of the biofouling effect at Capo Passero site (see fig. 2.1) has been carried out analysing the data taken, in the period March 2003 - October 2004, with the same apparatus used by the ANTARES collaboration to measure the biofouling effect in Toulon site and mentioned in a previous paragraph. This dedicated experimental set up, is capable to quantify the variation of the transparency of a glass surface placed for long time under-water, at different angles to respect to the vertical axis. It consists of a system made by light sources (blue LEDs) and detectors (photodiodes) placed at different polar angles inside a glass sphere.

This set-up can help to quantify the eventual loss of light detection efficiency in photo-detectors placed inside glass spheres, due to the growing-up of bacteria colonies and to sedimentation on the glass surface: this process, usually called "biofouling", can produce a transparency loss of the glass spheres which will host PMTs, once they are placed underwater for several years.

The fouling process starts as soon as the apparatus is put underwater: the surfaces start to be affected by bacteria colonies fouling, creating a very thin biofilm. The fouling process can also be induced by sedimentation phenomena, which sometimes occur and which can be related to underwater currents.

A detailed study of the biofouling effect, as a function of time, is mandatory since the variation of the glass spheres transparency can reduce the detection efficiency of the whole telescope and/or affect its angular resolution.

The photons, produced by Čerenkov effect when a high-energy muon passes through seawater, can become unlikely to reach the PMTs as a consequence of the transparency loss.

A slow glass spheres transparency loss is expected to occur as a function of time: this effect has been already observed and reported as characterized by a regular trend superimposed to several random fluctuations, which mainly occur mainly for upward – looking surfaces.

The position on the optical modules has been, in this report, indicated according to the picture shown in figure 8.4: according to the picture, we characterize the position with the sphere “latitude” θ , and $\theta=0$ represents the "Equator" of the glass sphere.

Figures 8.5 show, as a function of time, the light transmission through the glass surface for the full deployment period and for photodiodes located at different latitude angles inside the glass sphere.

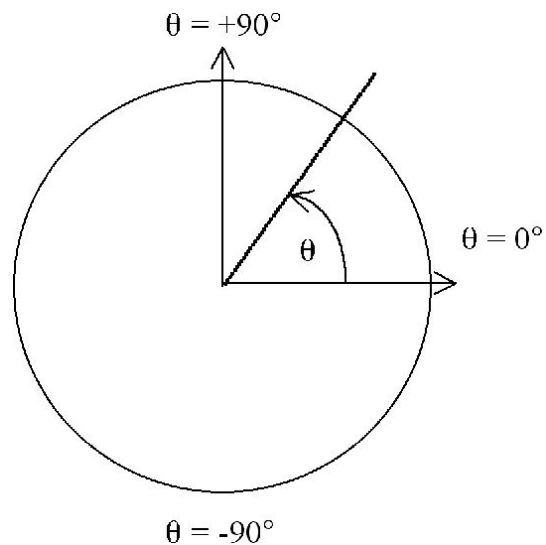


Figure 8.4 Latitude on the Optical Modules.

It can be easily be noticed that the variation of transparency can follow a slow regular trend or can be described by strong, positive and or negative, variations. Fast variations are common in periods characterized by intense water currents, as already reported by ANTARES collaboration discussing the analysis of data collected in Toulon site.

Slow transparencies variations are consistent with the surfaces being fouled by microbial adhesion, larger and stochastic transparencies variations are consistent with the deposit of sediments on glass surfaces: they can also be washed off by flowing water.

In general, as reported before discussing the ANTARES results, these figures show a general trend of decreasing fouling with increasing zenith angle on the glass sphere.

We quantify the “biofouling” effect analyzing the photodiodes signals as function of time and latitude. Each photodiode signal is normalized to the value collected immediately after the detector deployment under-water allowing in this way to evaluate the variation of the glass transparency with time. All transparencies variations are expressed as percent variation in one-year time.

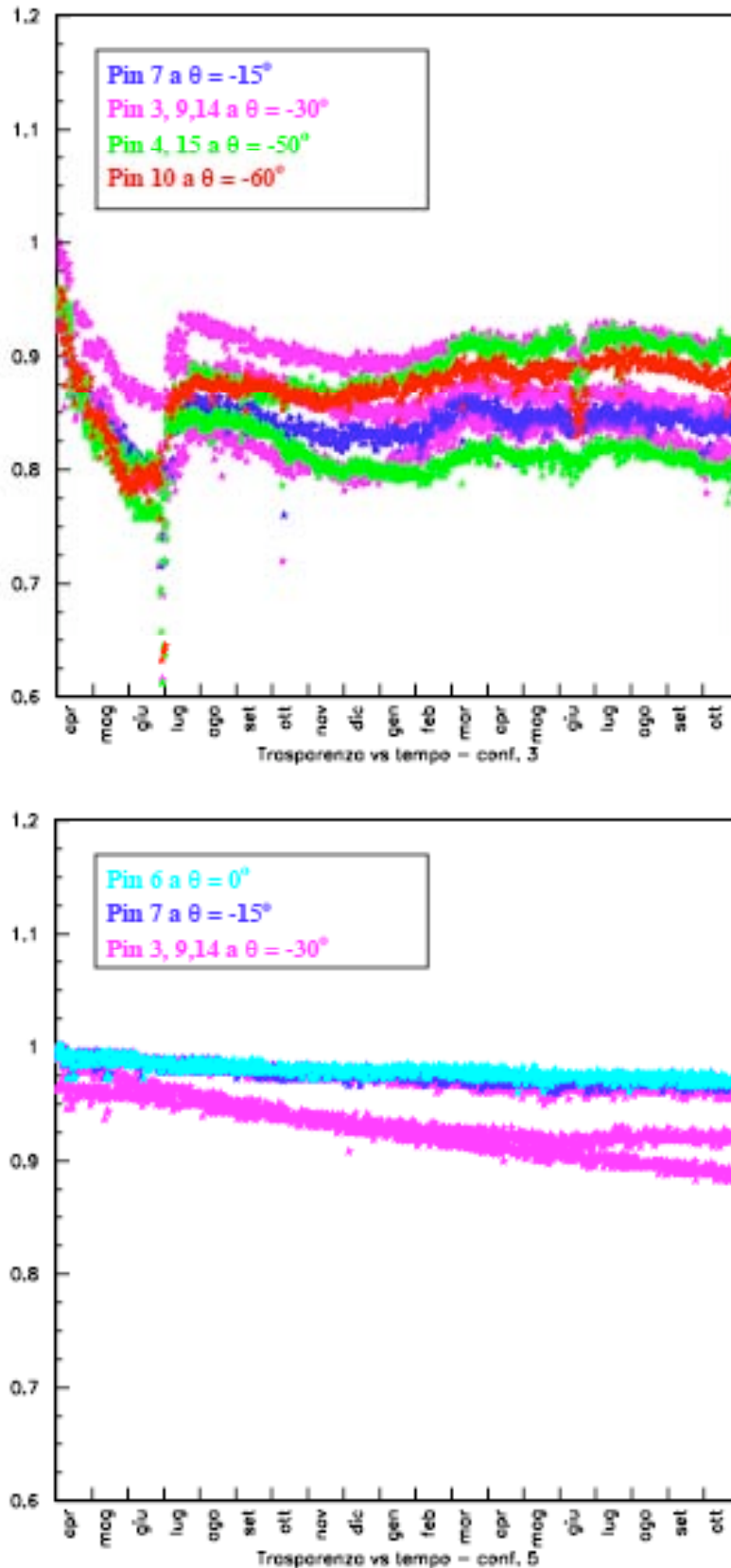


Figure 8.5 - Behaviour with time of the signals collected by photodiodes placed, at different latitudes, inside the glass sphere, all signals are normalized to the value collected immediately after the detector deployment under water.

Figure 8.6 shows the transparency variation, expressed in percentage per year, as a function of the optical modules latitude. We observed a reduction of glass transparency

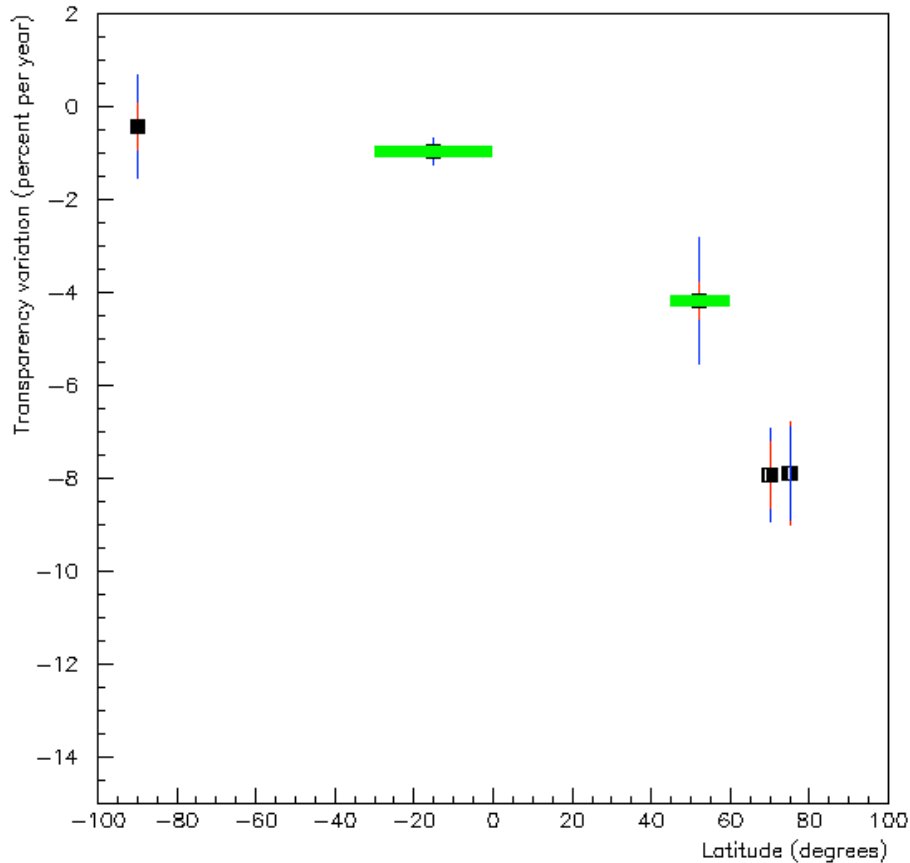


Figure 8.6 – Transparency variation, expressed in percentage per year, as a function of latitude on the Optical Modules. Red bars represent statistical errors, while blue bars represent the systematical ones. The green stripe over an angular region indicates that the corresponding value of transparency variation has been obtained by averaging the values of that interval.

mainly for upward looking surfaces ($\theta > 0$), while for downward-looking surfaces the mean fouling effect has been estimated to be less than 2% per year.

The sedimentation process appears to be relevant for upward-looking surfaces: it can lead, even in short periods, to both positive and negative variations of transparency. Downward-looking surfaces are less affected by sedimentation process, however they are affected by bacteria colonies fouling, creating the thin bio film.

We observed that the decrease of transparency diminishes as a function of time becoming constant about a year after deployment: this result is shown in fig. 8.7 for different sphere latitudes.

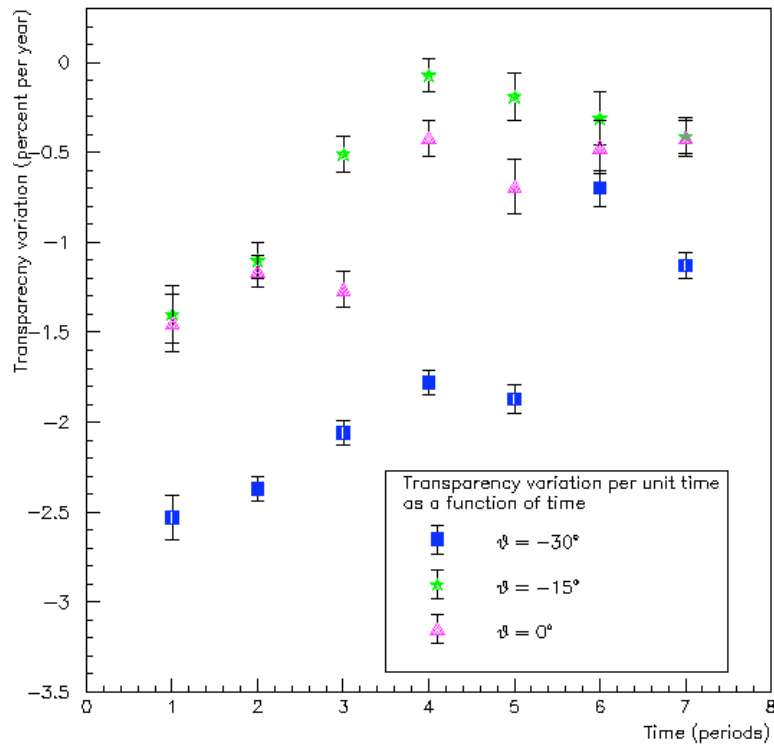


Figure 8.7 - Fouling speed evolution: transparency variation as a function of time for the equatorial part of the optical modules. The whole data sample, collected over about 18 months, has been sub-divided in seven ~80 days equal periods.

- **Biofouling measurements in NESTOR site**

Surfaces exposed to the marine environment typically develop a layer of attached organisms, a condition that is generally referred to as biofouling. Biofouling is any association of marine organisms that emerge on artificial or natural hard substrate. The term fouling is related to the words dirt, filth and damage as the presence of fouling organisms can utilize the structure on which they have settled or in which they bore.

Fouling causes several environmental and socioeconomic problems, like exotic species (CIESM, 2002 & ICES, 2003); hull fouling enhances fuel consumption (Adkins et al., 1996), reduction in the heat transfer efficiency (Bell, 1978) or blocking of pipes (Geesey, 1994). Bio-corrosion, causing a significant reduction of equipment lifetime, is also a result of fouling (Little & Lavoie, 1979), as it creates an oxygen concentration gradient across the surface of the material (Walker and Keevil, 1994). Furthermore, recent concerns about fouling problems of oceanographic instruments have pointed out the need to understand biofouling in order to figure out antifouling mechanisms for protecting those instruments and for securing the accuracy of data. In 1994 Stahle showed that a transmissometer immersed in water depths less than 100 meters gives unusable data (60% light transmission) after one month. Biofilms in general induce

scattering and absorption of optical signals, comprising the integrity of data (Kerr et al., 1998, Mars et al., 1999).

In order to secure correct data transmission from oceanographic instruments and to protect them from biofouling, it is important to understand the nature of biofouling, particularly biofouling and sedimentation.

For the evaluation of biofouling potential at the NESTOR site an experimental device is under construction (figures 8.8 and 8.9). To understand the biofouling process in such an extreme environment, parameters as substrate type, orientation, depth, setting period and duration will be taken into account (Table 8.1).

Table 8.1: Parameters that will be tested

Parameters	
Substrate types	Aluminium, titan, glass, limestone and shale
Depths	500m, 1000m, 2000m, and 4000m
Orientation	Horizontal up and vertical
Setting period	“Summer” (May) and “winter” (October)
Duration	6 months in all depths and also 12 and 18 months in 4000m

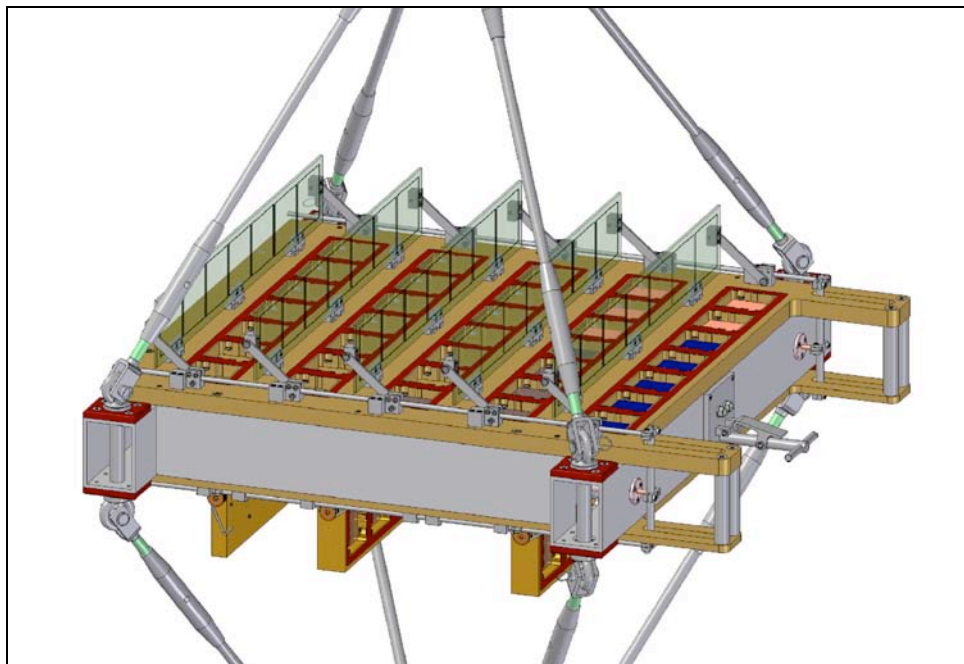
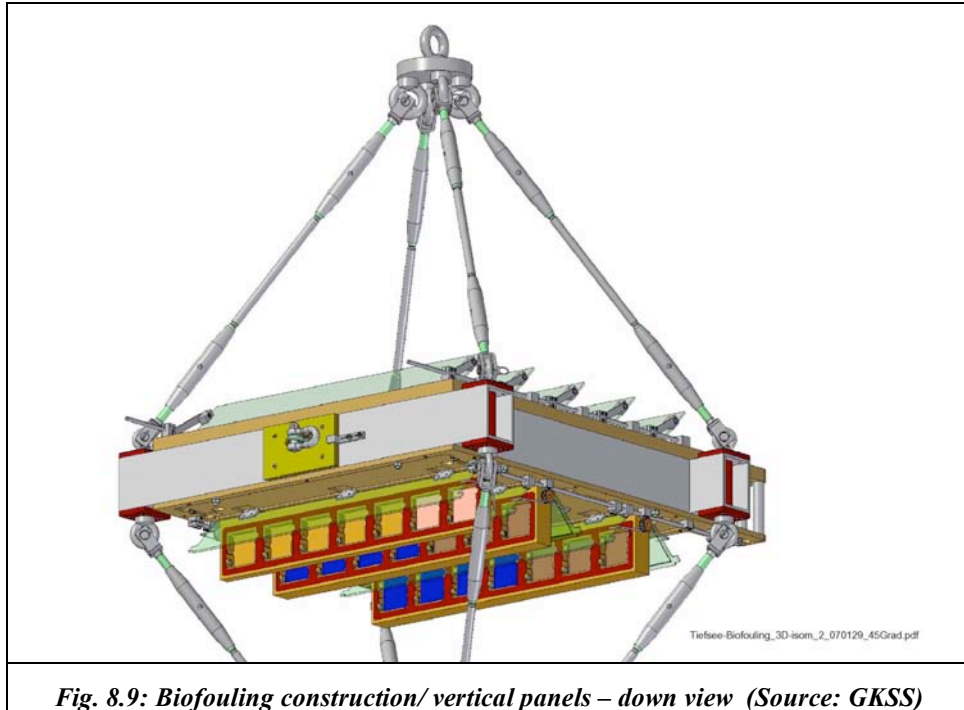


Fig. 8.8 - Biofouling construction/horizontal panels – up view (Source: GKSS)



At the HCMR BN1 site a mooring line with one biofouling platform in each depth (Table 8.1) will be deployed in May 07. An overview of deployment and retrieve is given in Table 8.2.

Table 8.2: Overview of Biofouling Experiment

	May 07	October 07	May 08	October 08
500m				
	Deploy	Retrieve		
		Deploy	Retrieve	
1000m				
	Deploy	Retrieve		
		Deploy	Retrieve	
2000m				
	Deploy	Retrieve		
		Deploy	Retrieve	
4000m				
	Deploy	Retrieve		
		Deploy	Retrieve	
	Deploy		Retrieve	
	Deploy			Retrieve

Analyzing the biofilm

For analyzing the biofilm formation and the percentage abundance of bacteria epifluorescence microscopy will be used and SEM for the analyses of the biofilm structure. The cells will first be stained with DAPI' (4', 2-diamidino-2-phenylindole dihydrochloride, $10 \mu\text{g ml}^{-1}$) for 7 min and then dip-rinsed in distilled water to wash off the excess stain (technique from Kerr et al., 1998 modified by Head et al., 2004).

Biofilm structure: At each season (summer and winter) and for each substratum in each orientation, three panels are taken for biofilm structure analysis. Biofilm is sampled on each panel by five random replicates. The counted micro-organisms will be identified as bacteria, protozoa, and fungi etc.

Biofilm structure: Multivariate analyses will be done on untransformed Bray–Curtis dissimilarities among panels. The biofilm structure will be represented on each panel by averaging the data from the five SEM replicates. To test the null hypothesis that there is no significant difference in material, orientation, depth or season statistical analyses will be done using One-Way-ANOVA (ANOSIM, Clarke, 1993) for each hypothesis.

Similarity percentage (SIMPER, Clarke, 1993) will be used to identify, for each substratum the percentage contribution of each taxon to the biofilm structure.

- **Corrosion and pressure action of the deep-sea on the NESTOR floor-detector**

Deep sea water muon and neutrino detectors, like ANTARES, NEMO or NESTOR, use the Coherences light, produced by leptons (mainly muons) to detect the interaction of a neutrino. As a very complicated complex multipurpose arrays which are established deeply under water these detectors (deep under water neutrino telescopes) should be designed to provide continues operation within not less than 10 years for accumulation of necessary statistics of registered events. Presence of a high pressure and the aggressive seawater environment forces to approach with special carefulness to selecting the materials necessary for units and parts of deep-water neutrino telescopes.

The main "enemies" of the facilities working in deep sea water are corrosion and pressure. Process of corrosion is well studied and, basically, it is clear how to avoid significant corrosion of elements of deep-water neutrino telescopes. The major principle for prevention of electrochemical corrosion is manufacturing all metal details from the same kind of metal or even from different metals, but with almost equal electrochemical potentials. For the deep-water devices, spending long time under water, Ti- alloys are the best materials. However in case of such complex systems as neutrino telescopes it is very difficult to make everything from titanium, especially the smallest details, because of its high price or the absence of prefabricated parts of the needed size. It is necessary to combine. First of all it concerns anchors and buoyancy, the elements distanced from the basic systems. Besides there always is a probability that at assembly of system among fixing elements there can occur a bolt or a nut made or others small things of inappropriate metal. Moreover, the proper combination could minimize material costs and simplify the technology for neutrino telescope production. Therefore any result of the analysis of processes of corrosion of devices, long time worked at the big depth in sea water, is very important and useful and experience should be generalized.

We started collecting data about influence of pressure and corrosion from first tests of elements of deep-water neutrino telescope NESTOR. In the given paper the results of the analysis of conditions of elements from the NESTOR test-detector which was exposed long time at the depth of 4000 m in the Mediterranean Sea are presented. This experience should be taken into account upon creation deep under water neutrino telescope.

Components in deep-sea

First long-term tests were started when in 2000. A 30 km-long deep sea cable with 18 mono mode optical fibers is laid from the shore to the deep-sea site (Fig.8.10). One copper conductor can deliver up D.C. power. The scientific payloads are attached at the end of cable. The sea end of cable is hoistable in order to change the deepwater equipment. The cable landing is terminated in the Terminal cable station in the village of Methoni (11 km from Pylos).

In January 2002 the end of the cable was brought to the surface by recovery rope and connected to the telescope bottom unit or “pyramid” constructed from corrosion resistant aluminum alloy (A14V2) tubes. This pyramid structure (Fig 4.7). is used for a attachment of environmental sensors and seawater electrode. The pyramid also houses the mass anchor and cylindrical junction box (JB) made from Ti-alloy. The mechanical part of the electro-optical cable is attached via a bend restrictor and a hang-off-terminator to the pyramid. The e/o cable is connected via GISMA hybrid connector to the JB. The off shore seawater electrode is also connected to the JB to provide the power. Many of these components are first-of-kind items and have had to be developed and tested for operation at a depth of 5000 m. The deployed package at the NESTOR site consisted of temperature sensors, pressure sensor, a compass, a light attenuation meter, a water current meter and an ocean-bottom seismometer (OBS). Useful data were transmitted to the shore from the pyramid and long-term variations in environmental parameters were obtained.

In March of 2003 the pyramid was brought back to the surface. The floor of the NESTOR test-detector (Fig 8.11), made out with Ti, was connected and deployed. The

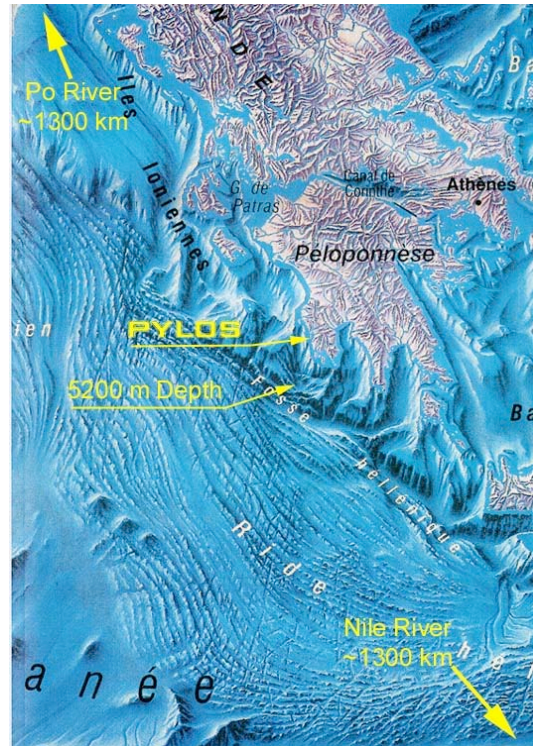


Fig.8.10. The NESTOR site.

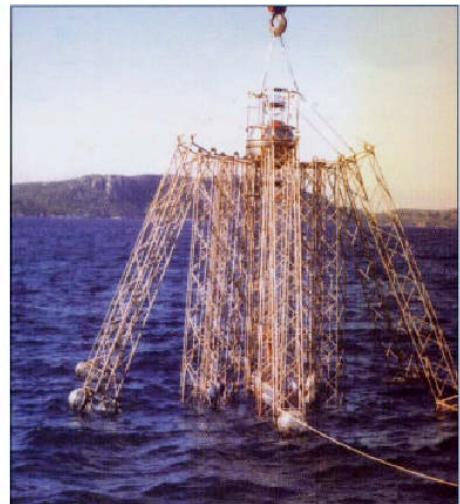


Fig.8.11. The NESTOR Ti-floor

present detector floor structure measures only 12 m in diameter but consists of the usual 6 arms and is equipped with 12 OMs. The detector floor was mounted some 150 m above the anchor. There are LED calibration pulse modules installed 20 m above and 20 m below the center of the floor plane.

The floor-detector has enough its own flotation and does not provided with additional buoy for underwater stability. The recovery buoy with its own mass anchor and release system was attached to the end of recovery rope and distanced from floor detector at about 5 km. The supporting frame of the buoy is made from mild steel structural shape. Two peaces of syntactic and 9 BENTHOS spheres are provide positive buoyancy of +215 kg which is enough to remove the end of the recovery rope on the sea surface. Buoy system is equipped with both auto light and auto radio beacons.

All deployment operations were made from a service vessel. All cable connections were made outside the water, on board of the vessel. This procedure does not require any robot or special submarine, it is cheap, quick and efficient

The purpose of this deployment was an engineering run with carrying out an overall system performance test under real conditions at full depth with the unavoidable ^{40}K decays and bioluminescence backgrounds, studying characteristics of the modules, testing the control and data acquisition system, the software, including its event reconstruction capability, and obtaining experience with the overall system operation.

Because of lack of coincidence between good weather and availability of a service vessel NESTOR test-detector stayed under water of 2.5 years. That provided very useful long-term examination for mechanical construction and all materials immersed at the big depth. Data about corrosion and pressure resistance are important for future large neutrino detecting array of KM3.

Pressure action

Housings for electronics and optical modules must resist against action of pressure which amount more than 400 atmospheres at 4000 m depth. All pressure housings were tested under 450 atm in the pressure tank before assembling of the NESTOR test-detector. However these tests cannot substitute long-term examinations *in situ*. First of all it concerns glass spheres that can loose strength in water because of leaching.

Practically all housing removed from 4000m depth do not have visible damages due to pressure action. Only one glass sphere lost visible chip about 5 cm in diameter and 1 mm at the maximum thickness from outward surface. There are no visible deformations of the titanium and bronze GISMA connectors. In the case of inappropriate construction the deformation under pressure could be so considerable that it did impossible to open connectors. In our case all connectors are opened easily. There is no water flowing through packing rings or from the side of cable penetration.

This result looks like trivial, but it is very important result, because before that nobody had experience of so long maintenance glass spheres at the depth of 4000 m.

Corrosion of the metal parts.

Corrosion is an electrochemical process in which a metal reacts with its environment to form an oxide or other compound. The cell which causes this corrosion process has three essential constituents: an anode, a cathode and an electrolyte (electrically

conducting solution). The anode is the site at which the metal is corroded; the electrolyte is the corrosive medium; and the cathode (part of the same metal surface, or of another metal surface in contact with it) forms the other electrode in the cell and is not consumed in the corrosion process. At the anode the corroding metal passes into the electrolyte as positively charged ions, releasing electrons which participate in the cathode reaction. Hence the corrosion current between anode and the cathode consists of electrons flowing within the metal and ions flowing within the electrolyte. The surface of one component may become the anode, and the surface of another component in contact with it, the cathode. Usually, corrosion cells will be much smaller and more numerous, occurring at different points on the surface of the same component. Anodes and cathodes may arise from differences in the constituent phases of the metal itself, from variations in surface deposits or coatings on the metal, or from variations in the electrolyte. The rate of corrosion is influenced considerably by the electrical conductivity of the electrolyte. Pure water has poor electrical conductivity and the corrosion rate will be much lower than, say, an acid or alkali solution of high conductivity. The ability of metals to resist corrosion is to some extent dependent upon their position in the electrochemical series (Table 8.3, [30],[31]). Table 8.3 provides easy way to choose appropriate combinations of different metals for the underwater equipment production. The farther two metals are separated from one another in the electrochemical series, the more powerful is the electric current produced by their contact in the presence of an electrolyte. Also the more rapidly the metal towards the bottom of the table is attacked and the more will the metal towards the top of the table be protected. It must be remembered, however, that the order in the above series may vary under special corrosive conditions, and the galvanic series in service media, e.g. sea water, are often more useful from the corrosion aspect.

The size of the cathode relative to the anode is important, e.g. small copper rivet (cathode) in a large steel plate (anode), is quickly polarised and corrosion on the plate is small. On the other hand, a large cathode coupled to a small anode has the opposite effect, with rapid attack of the anode. Electrochemical corrosion can be stimulated by not only differences in the metal surface, but also by variations in the electrolyte, [32], [33]. The presence of dissolve oxygen in the sea water accelerates the cathodic reaction; and consequently the corrosion rate increases in proportion to the amount of oxygen available for diffusion to the cathode. Cavities in metal surfaces and metal surfaces partially covered by another material are prone to this type of

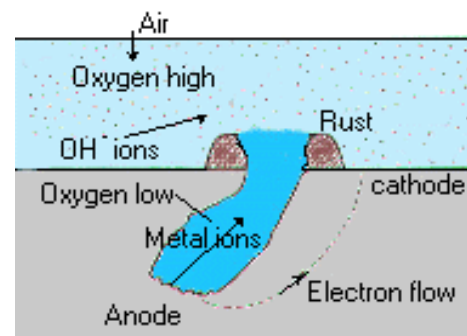


Fig.8.12 - Pitting corrosion

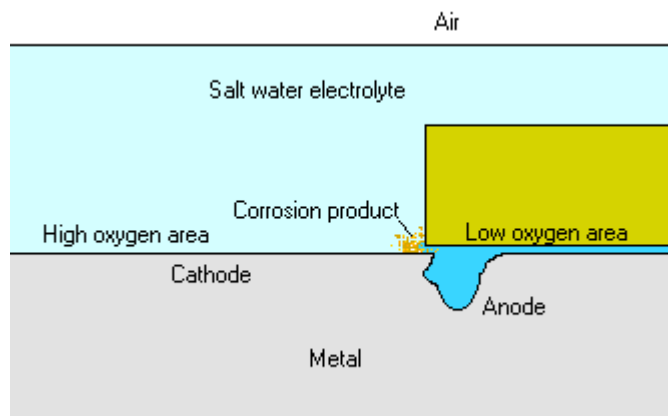


Fig.8.13 - Crevice corrosion

attack. The diffusion of oxygen into cavities or crevices is impeded and results in these areas becoming anodic to the surrounding metal which oxygen can easily reach (oxidation-concentration cell). The metal ions formed in the cavity migrate outwards and react with the hydroxide ions flowing in the opposite direction to form a corrosion product (rust) at the mouth of the cavity or crevice. This position of the corrosion product accentuates the corrosion by making the diffusion of oxygen to the anode more difficult, and if the cathode area is large severe pitting (Fig.8.12) may occur [34], [35].

Normally corrosion resistant materials which rely on thin oxide films for protection, such as stainless steel, can suffer from this type of corrosion attack [36]. These materials rely on oxygen being present, so that they can maintain their oxide films (passive state). When oxygen is excluded and the oxide films break down, the whole surface becomes active and corrodes readily (Fig.8.13).

The effects of corrosion can be accelerated or induced when operating in conjunction with stress and various wear mechanisms. Usually the mechanisms work by not allowing the corroded metal to become passive by continually removing protective films and setting up active/passive corrosion cells where the mechanism is not uniform applied [29]. The corrosion products formed may provide abrasive debris to make matters worse.

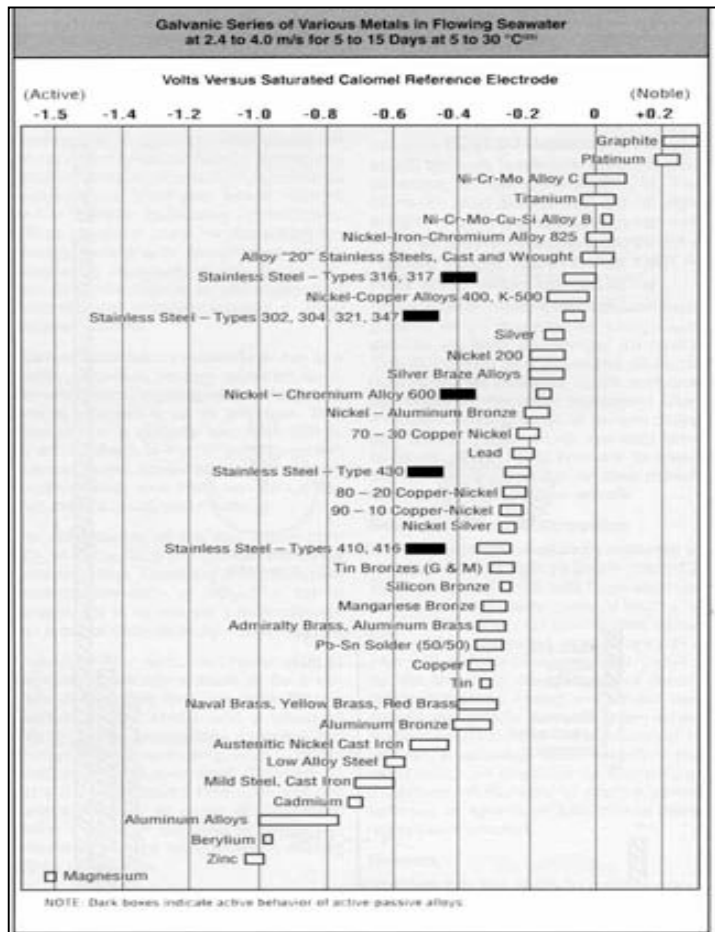


Table 8.3 – Galvanic series of various materials.

The best material for the mechanical construction of neutrino telescopes is titanium alloys. Titanium resists

corrosion by seawater at temperatures as high as 260⁰ C. Titanium tubing which has been exposed to seawater for many years at depths of over a mile shows no measurable corrosion. It has provided over twenty five years of trouble-free seawater service for the chemical, oil refining and desalination industries. Pitting and crevice corrosion are totally absent. The presence of sulphides in seawater does not affect the resistance of titanium to corrosion. Exposure of titanium to marine atmospheres or splash or tidal zones does not cause corrosion. However if Ti is chosen the use of Al details should be excluded completely. The combination Ti + Al is worst for the sea use (see Table 8.3). The main part of the test-detector, a Star, was made from Ti-alloy OT-4 (Russian Standard). This part of detector was NOT susceptible to corrosion. Only parts consisted of

some details made from aluminum and mild-corrosion process: the anchor unit, the recovery buoy and LED units

We were surprised a little when found so slight corrosion on the parts which were taken out from the depth. Even made from mild steel the buoy's frame was slightly covered by spots of pitting corrosion. Of cause it was protected with Zn-anodes and painted by special protective vanish. In any case the frame has returned from the depth in a very good condition and will be used again (see Fig.8.14). It should be mentioned also that after a long time of installation on the sear floor in 4000 m of water, there has been no visible indication of corrosion on the aluminum pyramid. Even five fingers on the hand are too many for calculation of the details with evident corrosion. One can see at the Fig.8.15 a typical crevice corrosion between the stainless steel washer and "hard hat" of the BENTHOS

and stainless steel could provide a



Fig.8.14- The buoy's frame from NESTOR test-detector is ready for new deployment

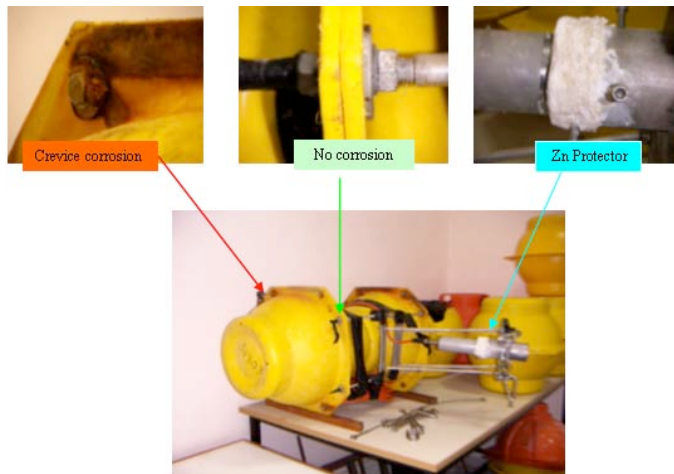


Fig.8.15 - Manifestations of corrosion on the LED unit

One more corrosion attack took place on the stainless steel straps girdled BENTHOS spheres. Bolts on the buckles were completely destroyed by crevice corrosion (Fig.8.17). The weakening of the straps is not dangerous for BENTHOS spheres. However a settling of the

sphere. We have to state, the corrosion was slow enough and has destroyed not more than a half of the thickness of washers. It's easy to see more of the same in Fig.8.16: neither bolts or nuts nor even the grovers were attacked. Only stainless steel washers had traces of crevice corrosion, but not all of them. Perhaps some washers and bolts (nuts and spring rings) were made of different kinds of stainless steel. The solution is simple, use plastic washers.

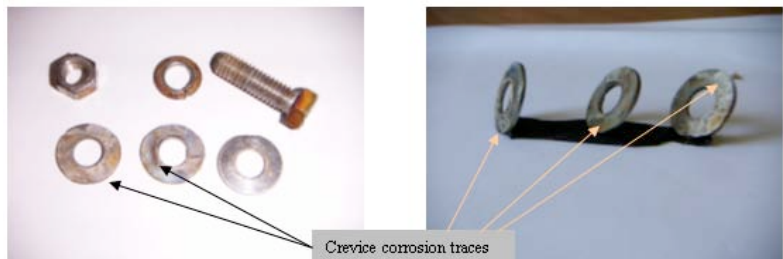


Fig.8.16 - The bolts and washers of fig.6. Traces of the crevice corrosion on the stainless steel washers only. Bolts and nuts have no signs of corrosion

rust on the BENTHOS's surface at the side of photo cathode can spoil sensitivity of the OM.

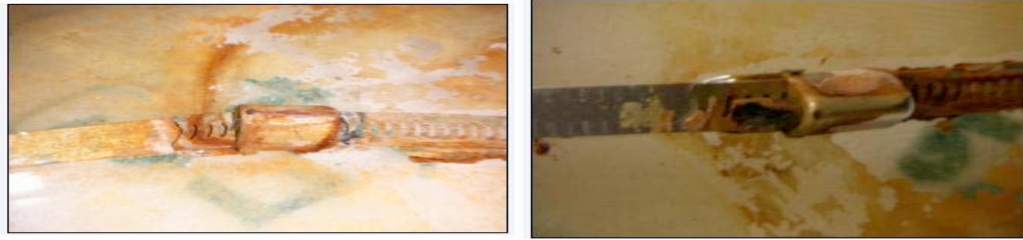


Fig.8.17 Result of corrosion attack to the buckle on stainless steel straps girdled around BENTHOS sphere.

Glass spheres corrosion.

Corrosion of glass in sea water is a process of decomposition due to leaching (solving process) and diffusion of alkali ions, across a hydrated porous silica network. Factors effecting this decomposition are, [37]:

- the composition of the glass itself;
- the composition and pH of the attacking solution;
- the temperature of the attacking solution;
- time.

The composition of the glass will determine its stability. Glass is composed of a network former – silica, and alkaline modifier such as sodium or potassium oxide, and calcium oxide, the positively charged ions of which will stabilize the negative ions of the alkali. In our case borosilicate glass (Pyrex) with low rate of radioactivity is used for the BENTHOS.

The pH of the attacking solution is important. For instance glass retrieved from an acid environment often had an iridescent layer of leached silica. If later that glass is immersed into fresh or sea water the alkali which diffuses out is neutralized by the acid and few hydroxyl ions are available to react with the silica. This reaction leaves a thick layer; the alkali leaks out and the silica remains as a hydrated network, in short, water is holding the glass together.

The composition of the attacking solution, in our case of marine environment, is rarely stable and can alternately increase or limit amount of leaching taking place. Being extremely saline, sea water contains many chlorides as well as oxygen and hydrogen sulphide generated through the activity of marine organisms and rotting vegetation. In such environment the reaction of exchanging alkali (mainly sodium) by hydroxyl (OH) ions proceeds at a constant rate throughout the glass [38]. A partially devitrified glass surface may change the appearance of the BENTHOS sphere. Particularly striking effects of iridescent colour may result from the interference of light by the thin film or flakes which compose the surface of the sphere.

If many times glass sphere was immersed under water over time many of these iridescent layers may build up into an 'Onion Skin' laminar formation and eventually exfoliate or fall off the glass [9]. The similar event arises when glass sphere is getting old besides of the use under water. Even under variable humidity many of iridescent layers may build up too and sphere loses a mechanical strength. Therefore, the leaching process may lead to a changing of the optical and mechanical properties of the BENTHOS sphere.

Taking into account the manifestations of leaching described above, we carefully inspected BENTHOS spheres recovered from the 4000 m depth after 2.5 years from deployment. Neither iridescent layers nor 'Onion Skin' were found. The absence of any visual spots of mat, micro scratches or rainbow colours on the outer or inner surfaces of the BENTHOS spheres allowed us to state that leaching during 2.5 years is negligible. The view of the outer surface of the used BENTHOS compared with one never used under seawater is shown on the Fig.8.18. One can see the practically identical structure of outer surfaces of both spheres.

Summary about corrosion.

All observations concerning corrosion we summarised in the Table 8.4 One can easily see there are only a small number of corroded elements of the detector's construction.

Table 8.4 - Signatures of the corrosion			
Part of the detector	Material	Type of corrosion	Comments
Recovery buoy's bearing construction	Mild steel	Pitting corrosion	Frame was painted by special enamel and protected by Zn
Floor detector	Titanium alloy	No corrosion	Ti-alloy OT 4 (Russian)
LED encapsulations	Stainless steel	No corrosion	Protected by Zn
Bottom pyramid	Aluminium alloy	No corrosion	Al-alloy A14V2 (German) Protected by Zn
Junction box	Titanium alloy	No corrosion	Ti-alloy OT 4 (Russian)
Bolts	Stainless steel	No corrosion	Not all washers were corroded
Nuts	Stainless steel	No corrosion	
Brads	Stainless steel	No corrosion	
Washers	Stainless steel	Crevice corrosion	
Spring rings	Stainless steel	No corrosion	
Hardhats	Plastic	No corrosion	
Sheath of cables	Plastic	No corrosion	
GISMA connectors	Ti-alloy	No corrosion	
GISMA connectors	Sea bronze	minor Pitting corrosion (on the flange)	Bronze connectors were used at the OMs
Glass BENTHOS spheres	Borosilicate glass	No corrosion (leaching)	
Straps for BENTHOS	Stainless steel	Crevice corrosion	Maximum attack is on buckle bolts

At first, of course, it is due to right choice of material. However the question still arises: why if the corrosion appears, its rate is so slow? Indeed, buoy's frame has a slight pitting corrosion and washers lost only a half of their thickness due to crevice corrosion during 2.5 years under water. We suppose perhaps it results from low quantity of

oxygen dissolved in deep sea water. It should be mentioned here also, there is low rate of sedimentation and overgrowing by marine organisms at the NESTOR site. We did not find visible signature of vital function of micro marine organisms on the surface of any part of the detector. One can argue that detector was washed during recovery procedure. This could be true however in Baikal project for instance, there are a lot of sediments fixed on the surface of neutrino detector with slime and it never was washed completely at the time of recovery.

The fact of low rate of sedimentation and overgrowing is very important for the future full neutrino telescope not only because they could brake sensitivity of optical modules, but could provoke corrosion and leaching also.

Low sedimentation rate, absence overgrowing, slow rate of corrosion all together with the excellent optical and hydrological characteristics of water render NESTOR site as most suitable for neutrino telescope accommodation

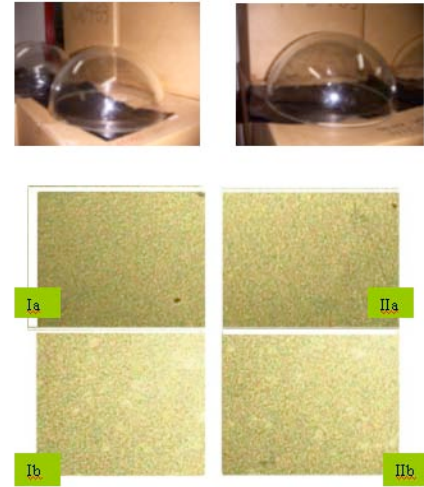


Fig.8.18 Condition of the BENTHOS exposed under water during 2.5 years (I) compare to one which never was under water (II)

Ia, IIa: outer surface's structure close to pole of the sphere

Ib, IIb: outer surface's structure at the back side of the sphere

Microscope magnification: 200

10. References

-
- 1 C.D. Mobley, *Light and Water*, Academic Press, San Diego (1994).
 - 2 S.Q. Duntley, *J. Opt. Soc. Am.*, 53 (1963) 214.
 - 3 L. Pappalardo et al., *Nuc. Phys. B (Proc. Suppl.)* 87 (2000) 525.
 - 4 J.A. Aguilar et al., *Astropart. Phys.* 23 (2005) 131.
 - 5 A. Capone et al., *Measurements of light transmission in deep sea with the AC9 trasmissometer*, *NIM A* 487 (2002) 423.
 - 6 G. Riccobene, A. Capone, *The NEMO Collaboration. Deep seawater inherent optical properties in the Southern Ionian Sea. Astroparticle Physics*, vol. 27 (2007) 1-9. Also published as astro-ph/0603701.
 - 7 C. Smith and K. Baker, *App. Opt.* 20 (1981) 1965.
 - 8 S. Khanaef et al.: “*Proceedings of the Second NESTOR International Workshop*”, L.K.Resvanis (Ed.), 1992, p. 273-270, www.nestor.org.gr
 - 9 E. Anassontzis et al.: “*Proceedings of the Second NESTOR International Workshop*”, L.K. Resvanis (Ed.), 1992, p. 270-284, www.nestor.org.gr
 - 10 E.G. Anassontzis et al, "Light transmissivity in the NESTOR site", *Nuclear Instruments and Methods A* 349 (1994) 242-246
 - 11 P. Amram et al., *Astrop. Physics* 13 (2000) 127.
 - 12 J.A. Aguilar et al., *Asptrop. Phys.* 26 (2006) 314.
 - 13 <http://www.ifremer.fr/sismer/catal/campagne/campagne.html?crno=5450020>
 - 14 L. Ursella, *Current-meter measurements at KM3 and KM4 in the period July 98 December 99*, Internal note (2002).
 - 15 T.A. Demidova and I.A. Repin, *Investigation of near bottom currents in inhouse pit in the vicinity of Nestor Area*, in “*Proceedings of the Second NESTOR International Workshop*”, 1992, p. 284-320, www.nestor.org.gr.
 - 16 G. Aggouras et al., *Laertis, a multidisciplinary station*, *Nuclear Instruments and Methods in Physics Research A* 567 (2006) 468–473
 - 17 P. Amram et al., *Astropart. Phys.* 19 (2003) 253.
 - 18 S. Heussner, C. Ratti and J. Carbonne, *The PPS3 time-series sediment trap and the trap sample processing techniques used during the ECOMARGE experiment*, *Cont. Shelf Res.*, 10 (1990) 943.
 - 19 J.I. Hedges and J.H. Stern, *Carbon and nitrogen determination of carbonate-containing solids*. *Limnol. Oceanogr.*, 29 (1984) 657.
 - 20 D.J. DeMastre, *The supply and accumulation of silica in the marine environment*, *Geochimica et Cosmochimica Acta* Vol.45, (1981) 1715.
 - 21 R.A. Mortlock and P.N. Froelich, *A simple method for the rapid determination of biogenic opal in pelagic marine sediments*, *Deep-Sea Research*, Vol. 36 n° 9 (1989) 1415.
 - 22 A. Boldrin et al., *Particulate matter in the southern Adriatic and Ionian Sea: characterisation and downward fluxes*, *J. Mar. Syst.* 33-34 (2002) 389.
 - 23 M.M. Turchetto et al., *Nutrients, phytoplankton and primary production processes in oligotrophic areas (southern Adriatic and northern Ionian seas)*, *Proc. XIII Congress Associazione Italiana di Oceanologia a Limnologia- AIOL*, Portonovo, Italy, 13, 2 (2000) 269-278.

-
- 24 S. Rabitti et al., Particulate Matter and Phytoplankton in the Ionian Sea, *Oceanol. Acta*, 17, 3 (1994) 297.
 - 25 A.F. Michaels and M.W. Silver, Primary production, sinking fluxes and the microbial food web, *Deep-Sea Res.*, 35 (1988) 473.
 - 26 Malanotte-Rizzoli et.al. ‘A synthesis of the Ionian Sea hydrography, circulation and water mass pathways during POEM-Phase I. *Progress in Oceanography*, 39: 153-204, 1997
 - 27 Warren, B.A., Deep circulation of the world ocean, in ‘Evolution of Physical Oceanography’, edited by B.A. Warren and C. Wunsch, MIT Press, Cambridge, Mass., 1981; Smith, P., 1975, A streamtube model for bottom boundary currents in the ocean, *Deep-Sea Research*, Vol 22, 1975
 - 28 Pollak, ‘The sources of the deep water of the eastern Mediterranean Sea’, 1951, *Journal of Marine Research* (128-151)
 - 29 Theocharis et al., 1999, Climatic changes in the Aegean Sea influence the thermohaline circulation of the Eastern Mediterranean (1986-1997). *Geophysical Research Letters* 26 (11), 1617-1620; Kontoyiannis et al., 2005, The hydrology and biochemistry of the Cretan Straits (Antikithira and Kassos Straits) revisited in the period June 1997 – May 1998. *Journal of Marine Systems* 53 (2005) 37-57
 - 30 V.V.Novysh. Brief hand book for underwater pressure housings design. Troitck, 1997, 40 p. (In Russian)
 - 31 Titanium in sear water. www.azom.com/details.asp?ArticleID=1336.
 - 32 CODEWELD® Titanium Tubing www.stainless-steel-world.net/titanium/seawate.
 - 32 Corrosion. Hand bock. www.metaltrade.ru/abc/k/korroziya.htm.(In Russian).
 - 33 E.Savinkina. Corrosion of the metals. 83.222.31.122/articles/116/1011691/1011691a1.htm (In Russian).
 - 34 H. Rachev, S. Stephanov. Hand book of corrosion. M., Mir, 1982, 523 p. (In Russian).
 - 35 A.I. Alcibeeva, S.Z.Levin. Inhibitors of corrosion. (Hand book) M., Chemistry, 1968, 264 . (In Russian).
 - 36 I.L.Rosenfeld. Corrosion and protection of metals. M., Mmetallurgy, 1969, 448 p. (In Russian). Corrosion. referat.niv.ru/referat/026/02600073.htm.
 - 37 I.A.Kumalagaev. Technology of glued multiple glass panes. http://okna.com.ua/art_.php?id=623 Windows, Doors and stained-glass windows Magazine, № 2, 2004, glass, (In Russian).
 - 38 Jane Pannel. Conservation of glass in Bodrum Museum of Underwater Archaeology. www.diveturkey.com/inaturkey/lab/pannell.htm Optical glass catalog 2005 ru. glassbank.ifmo.ru/eng/ (in Russian).